國立台灣大學電機工程學研究所博士論文

指導教授　李百祺教授

超音波定量血流量測

Ultrasonic Quantitative Blood Flow Estimation

研究生　葉秩光
中華民國九十三年一月

Table of Contents

中文摘要

本論文主要研究醫用超音波影像技術於人體血流量測之應用，同時配合超音波對比劑的輔助使用以探討新的定量血流量測技術。主要可分為兩大主題：超音波都卜勒角度量測以及超音波對比劑於血流量測之定量分析。

傳統超音波都卜勒技術只能量測沿著聲波前進方向的速度分量，為了修正以求得真正的血流速度及流量，就必須計算出聲波前進方向與血管之間的夾角(都卜勒角度)。利用超音波都卜勒頻譜頻寬效應於都卜勒角度量測已經廣泛被應用。我們提出以較短的資料長度配合自動回歸頻譜模型，得到都卜勒頻譜，然後計算出都卜勒角度。結果顯示，自動回歸方法利用較少的資料長度，所以比較不受到時間、空間速度梯度的影響，同時計算時間大幅降低，故可以實現於即時二維影像系統上。

利用以時間強度曲線為基礎的超音波對比劑技術已經應用於血流量測。本研究之第二部份，則希望能夠藉由量測所得到的混合腔輸入、輸出時間強度曲線配合去迴旋積分方式得到混合腔脈波響應，進而定量計算血流相關參數。首先，血流混合腔室模型被驗證是否為線性非時變系統，實驗結果顯示線性非時變系統的假設仍然是一個問題。雖然不能用去迴旋積分方式做絕對定量血流分析，但相對血流量的估計仍是可行。另外，對比劑應用於定量微灌流量測容易受到遮蔽效應的影響，為了解決遮蔽效應的影響，我們提出利用超音波對比劑輸入及輸出時間強度關係，提出新的定量血流量測方法，稱為輸入輸出時間強度曲線法。結果顯示輸入輸出時間強度曲線法不但能減少遮蔽效應的影響，而且可以用於相對血流量的量測。

此外，為了改善超音波對比劑血流量測系統解析度以觀察到低流速的微循環血流，我們亦提出一個高頻超音波對比劑破裂/充回影像系統。利用此系統所得到的時間強度曲線配合新的估算技術可以得到血流相關參數與實際血流速度關係。實驗結果顯示，實際血流與利用新的估算技術所估計血流之間存在一個相當高的相關性。此系統未來

應用包括高解析度小動物微血流如腫瘤血管增生的血流量估計及體表面血流量測。

關鍵字：超音波影像、血流量測、超音波對比劑、都卜勒角度、自動回歸方法、時間強度曲線、對比劑破裂/充回影像。

Abstract

The primary goal of this dissertation is to apply ultrasound imaging techniques to blood flow estimation. Ultrasound contrast agents are also used to explore new quantitative blood flow estimation techniques. The main topics of the dissertation include ultrasound Doppler angle estimation and quantitative blood flow estimation using ultrasound contrast agents.

Doppler principles have been widely used to estimate the blood flow velocity. However, such techniques can only detect the velocity component in the direction of wave propagation. In order to determine the true flow velocity, the angle between the wave propagation and the flow (i.e., the Doppler angle) must be known. We propose using an autoregressive (AR) model to obtain the Doppler spectrum using only a small number of flow samples and then to calculate Doppler angle. Since accurate estimates can be obtained using a limited number of flow samples, the Doppler angle estimated by the AR method is less affected by blood flow velocity gradients. Also, since only a small number of samples are used, the data acquisition time is significantly reduced and real-time two-dimensional Doppler angle estimation becomes feasible.

On the other hand, ultrasound contrast agents have been used to assist the assessment of blood flow parameters based on time-intensity measurements. By measuring the time intensities at both the input and the output of a blood mixing chamber, blood flow information can be obtained if proper deconvolution techniques are applied. In this study, the linear time-invariant (LTI) system assumption of the blood mixing mechanism is tested first. Results indicate that the LTI assumption does not hold but quantitative relative flow estimation is still feasible. Previous results have shown that the contrast-specific technique is not reliable in perfusion estimation due to the shadowing effect. To overcome this problem, a contrast-specific technique using both the input and the output time–intensity relationships is proposed and is referred to as the input–output time–intensity curve (IOTIC) method. It is concluded that the IOTIC technique eliminates the shadowing effect, making quantitative estimation of perfusion feasible.

To improve the spatial resolution and observe the low velocity microcirculation of the contrast-specific blood flow estimation technique, we also develop a high frequency microbubble destruction/contrast replenishment imaging system. Using a new estimation technique, flow constants proportional to the absolute flow rate are estimated from wash-in time-intensity curves. The results indicate a high correlation between the actual flow velocity and the estimated flow rate constant. Potential applications of this system include high-resolution angiogenesis perfusion assessment in small animal tumors and superficial vasculature estimation in clinical studies.

Key Words: ultrasound imaging, blood flow estimation, ultrasound contrast agents, Doppler angle, autoregression method, time-intensity curve, microbubble destruction/contrast replenishment imaging.

List of Symbols

A	received echo magnitude immediately after bubble destruction
$a_i^{'}s$	parameters of AR model
AUC	Area Under Curve
B	steady state value of the received echoes
bw	Doppler bandwidth
c	speed of sound
E	elevational beam width
$e(n)$	white, stochastic signal
F	transducer focal length
f_d	Doppler shift frequency
f_p	Doppler spectrum maximum intensity frequency
f_{reson}	bubble resonant frequency
$g(t)$	gamma function
$h(t)$	transfer function
$h_r(\vec{r},t)$	receive acoustic impulse responses
$h_t(\vec{r},t)$	transmit acoustic impulse responses
$I(t)$	time-intensity curve
$I_o(t)$	output function
$I_I(t)$	input function
κ	scaling factor
l	sample volume length
MTT	Mean Transit Time
N	number of flow samples
n	flow profile constant
$n(t)$	perfusion model
PRI	Pulse Repetition Interval
$P_e(t)$	Gaussian pulse
PE	prediction error
P_g	internal bubble gas pressure

P_l	ambient pressure with liquid
Q	flow rate
R	bubble radius
r	vessel radius
R_0	bubble initial radius
$\dot{R}$	velocity of bubble wall motion
$\ddot{R}$	bubble boundary acceleration
r_i	distance relative to the vessel cente
$T_{80\%}$	time to achieve 80% replenishment
$IT_{80\%}$	time to achieve 80% replenishment to corresponding ITIC
t_0	delay time
V	volume of mixing chamber
v	flow velocity
$V_{\max}$	maximum flow velocity
W	transducer aperture size
w	transducer beam width
$y(n)$	AR model
β	rate constant
λ	wavelength
θ	Doppler angle
ρ_l	liquid density
μ	liquid viscosity
σ	surface tension
ξ	acoustic response constant
θ_c	Doppler critical angle
τ	transit time constant
ψ	ratio of the estimated volume to the theoretical volume

List of Figures

List of Tables

1. Chapter 1 Introduction

In this chapter, the background and motivation for this research are developed and the dissertation scope is presented.

In the first section (1.1), a general overview of ultrasonic blood flow estimation is briefly introduced. Afterwards, several ultrasonic blood flow estimation techniques are reviewed in section (1.2). Three typical techniques including Doppler phase shift estimator, time shift estimator and two-dimensional velocity estimators are described and compared, respectively.

In section (1.3), ultrasonic microbubbles based contrast agents are introduced. Basics and current applications of ultrasound contrast agents are also presented.

Section (1.4) describes issues in quantitative volume flow estimation in medical imaging. In the final section (1.5), the scope for this dissertation is presented. The motivation for this research is emphasized, and the dissertation organization is outlined.

1.1 Ultrasonic Blood Flow Estimation

Medical imaging methods have been successfully developed to assess blood flow information in large vessels in the body. Figure 1.1 shows the major arteries and veins in the human body. These techniques include magnetic resonance (MR) angiography, contrast x-ray computed tomography (CT), and Doppler ultrasound. In this research, we focus on blood flow estimation using ultrasonic techniques.

Doppler ultrasound is a non-invasive technique for velocity measurements of blood flow. Johann Christian Doppler (1803-0853) was the first to describe the frequency shift effect that occurs when sound or light is emitted from a moving source and the Doppler effect now bears his name. To measure blood velocity using Doppler effect, ultrasound is transmitted into a vessel and the echo reflecting from the blood is detected. Generally, medical ultrasound operating in the 2-12 MHz range is one of the most widely used modalities for soft tissue imaging and large vessel blood flow assessment (Jensen 1996). Table 1.1 summarizes the diameters and velocities of vessels at different levels of the circulatory system.

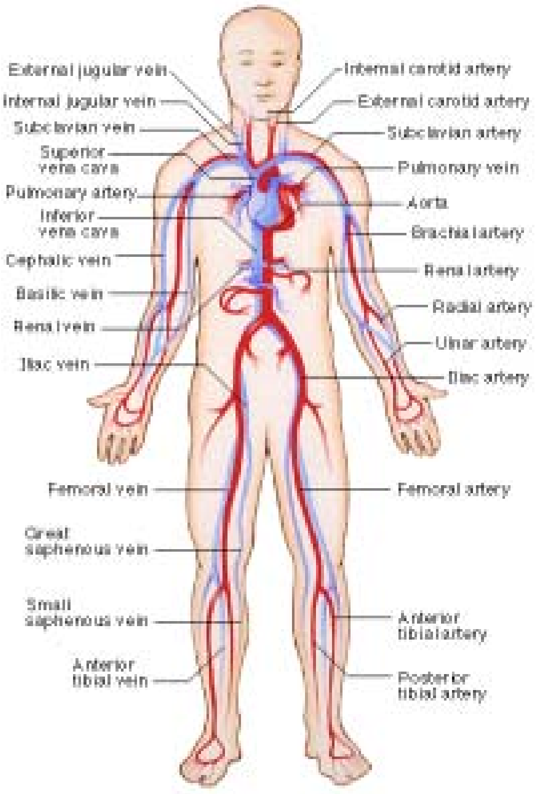

Figure 1.1 Major arteries and veins in the human body.

(From American Medical Association, *http://www.ama-assn.org/ama/pub/category/7152.html*)

Table 1.1 The diameters and velocities of vessels at different levels of circulatory system.

Vessel	Diameter (mm)	Mean Velocity (mm/s)
Ascending Aorta	10 - 24	100 - 400
Carotid Artery	2 - 8	100 - 200
Femoral Artery	2 - 8	100 - 150
Arterioles	0.01 - 0.1	2 - 10s
Venules	0.01 - 0.2	2 - 10
Capillaries	0.004 - 0.008	0.2 - 1.5

(From Zweifach and Lipowsky, *Handbook of Physiology*, 1985)

1.2 Doppler Effect

The Doppler effect resulting from ultrasound's interaction with moving red blood cells has been extensively used to determine the blood flow velocity. The previous developments of ultrasonic blood velocity estimation have been used to quantify mean blood velocity, blood velocity profile, and volume blood flow for clinical cardiology (Jensen 1996). Ultrasonic Doppler flow imaging has thus been routinely used and become a powerful tool in clinical applications.

1.2.1 Basic Principles of Doppler Effect

Doppler principles are schematically shown in figure 1.2. When both the source and the receiver are stationary, the frequency experienced by the receiver (f_s) is simply as c/λ, where c is the speed of sound and λ is the acoustic wavelength. If both the source and the receiver are moving and suppose the velocity of source is v_s and the receiver is moving toward the source at a velocity of v_r, the Doppler shift frequency (f_d) is

$$f_d = f_s (v_r + v_s)/(c - v_s) \tag{1.1}$$

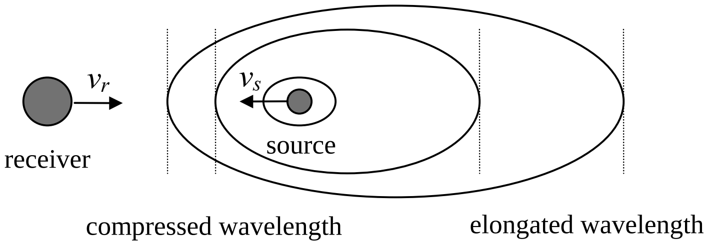

Figure 1.2 Diagram of Doppler effect.

Assuming the source velocity is much smaller the sound velocity (i.e., $v_r, v_s << c$), the equation (1.1) can be simplified as

$$f_d \approx f_s (v_r + v_s)/c \tag{1.2}$$

This assumption is true for diagnostic ultrasound since the velocity of typical physiological flows in the body are at most at the order of a few meters per second (please refer to table 1.1), whereas sound velocity in blood is around 1500 meters per second. Since motion of the source relative to the receiver causes a change in the observed sound frequency, blood flow velocity can be measured by detecting the Doppler frequency shift of echoes backscattered from moving blood. The primary scattering site in blood that produces echoes is the red blood cell. The scattering cross section of the red blood cell is about 1000 times larger than that of the platelet. Leukocytes are not present in sufficient numbers to influence the total backscattered signal.

Considering the real ultrasound system as shown in figure 1.3, the basic ultrasound Doppler equation (1.2) can then be written as

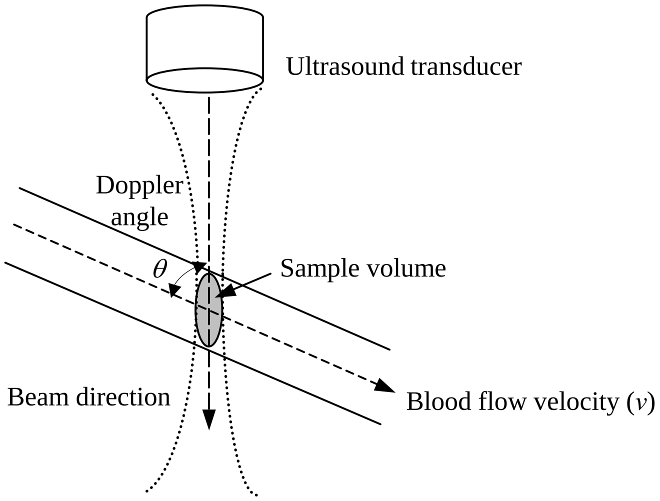

Figure 1.3 Doppler effect in ultrasound system.

$$f_d = \left(\frac{2vf_s}{c} \right) \cos\theta \tag{1.3}$$

where v is the blood flow velocity, f_s is the center frequency of transducer and θ is the Doppler angle between the flow and the ultrasound beam. Note that the frequency shift is doubled due to round trip propagation and only flows parallel to the ultrasound beam can be detected. For example: if the transmit frequency is about 2 to 4 MHz, the Doppler shift frequency of moving blood is in the audible range, e.g., < 20 kHz, and thus it can be heard through a pair of stereo loudspeakers.

1.2.2 Color and Spectral Doppler

Frequency shifts due to Doppler effect are typically estimated by short-time Fourier transform or efficient autocorrelation techniques. The former is usually called

Spectral Doppler, in which only flows along a single ultrasound line (continuous wave, CW) or flows within a particular sample volume (pulsed wave, PW) are estimated. The latter only estimates simple flow parameters, such as mean velocity, flow energy and velocity variance, and is capable of displaying two-dimensional flow information in real-time. Since flow parameters (velocity, variance and energy) are mapped to different colors, this is also known as the Color Doppler mode. Ultrasound Doppler color flow imaging provides the spatial information of velocity and direction of flow in real time. Currently, it is used primarily in a qualitative fashion to aid diagnosis of cardiac and peripheral vascular abnormalities (Jensen 1996).

1.3 Ultrasound Velocity Estimation Techniques

In this section, three ultrasonic blood flow measurements are introduced and compared, respectively. First, Doppler phase shift estimator is based on the Doppler frequency shift. The second one is time shift estimator that measures the time shift between two transmission pulses using the crosscorrelation technique. Finally, the two-dimensional estimator based on the speckle tracking technique is described for estimation of the lateral component of real blood velocity.

1.3.1 Doppler Phase Shift Estimator

The method for estimating blood velocity is to detect a Doppler phase shift in an ensemble of received echoes from a vessel (as shown in figure 1.3). The lateral axis represents the pulse transmission sequences (referred as the slow time index). The vertical range is the depth direction (referred as the fast time index). The time interval between two transmission pulses is referred as the pulse repetition interval (PRI). The Doppler frequency shift of the received echo backscattered from moving blood is detected by sensing the difference in phase between the echo and a reference signal (Baker 1970). In order to achieve a reasonable spatial resolution, pulsed Doppler (PW Doppler) was developed for ultrasound application in which a set of pulses are transmitted and received, and the ensemble phase difference is estimated. In other words, pulsed Doppler ultrasound is a technique for measuring the velocity of blood in a small sample volume.

One drawback of a PW Doppler system is that the maximum detectable Doppler frequency shift (which is directly related to the maximum detectable velocity) is limited by PRI (Azimi and Kak 1985). Therefore, the maximum velocity ($v_{\max}$) of the flow projected along the direction of the ultrasonic beam without aliasing is

$$v_{\max} \leq \frac{\lambda}{4 \cdot PRI} \tag{1.4}$$

On the other hand, the smallest velocity that can be estimated by PW Doppler is determined by the imaging system performance when detecting the phase in the presence of noise. The parameters of the imaging system such as the total observation time and the center frequency can be adjusted for estimation of low velocity blood flow. Generally, long observation times and higher frequencies can be employed to detect low velocities. Due to the low computational cost, Doppler phase shift estimator based on PW Doppler mode is commonly used in clinical ultrasound scanners.

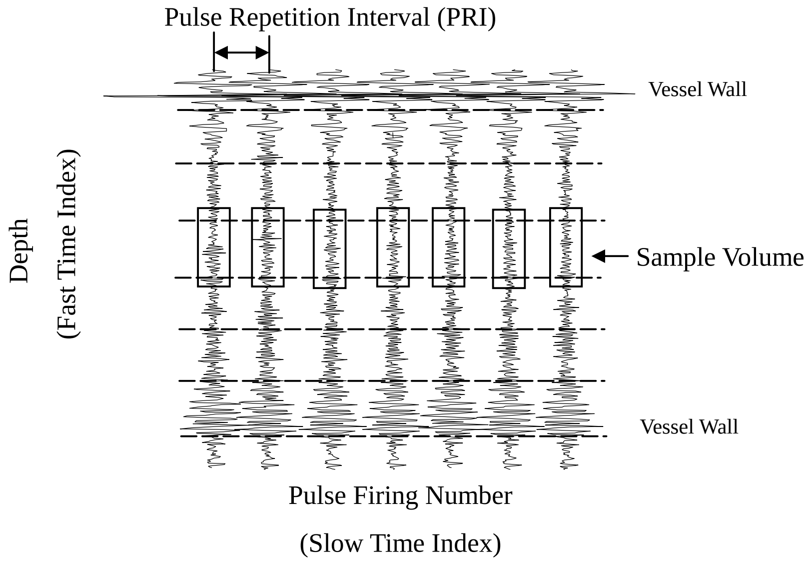

Figure 1.4 Typical pulsed Doppler signals.

The implementation of a Doppler phase shift estimator typically requires a transmission pulse length of 4-12 cycles in order to maintain a sufficiently narrow bandwidth (Li et al 2000). In fact, Doppler velocity estimation can be considered a narrowband technique. The continuous wave (CW) insonation performs the extreme narrowband and with a highest velocity resolution. Along the axial direction, high spatial resolution blood velocity estimation requires a short pulse length. Therefore, wideband velocity estimation can be alternatively achieved by implementing a time shift estimator.

1.3.2 Time Shift Estimator

The time shift estimator is most easily understood in the time domain. The crosscorrelation of a set of received echoes moving axially relative to the transducer is maximized at the correct axial velocity. This estimation strategy uses both the change in the position of the scatterers and the change in frequency of the received echo. The primary advantage of this estimator is that the transmission pulse can be as wideband as the transducer. Aliasing is generally considered not to occur using wideband estimation. Nevertheless, the computational cost associated with a correlation-based estimator is significantly larger than the computational cost of a Doppler phase shift estimator.

1.3.3 Two-Dimensional Velocity Estimators

One limitation of both Doppler phase shift and time-shift estimators is the inability to detect lateral blood flow. Both estimators are designed to estimate the axial component of the real blood velocity and therefore information of velocity in vessels that have a lateral component will be missing. An unbiased estimate can be corrected if the beam-vessel angle (Doppler angle) can be measured using traditional B-mode ultrasound imaging. Unfortunately, for small blood vessels or for complicated vessel geometry, the Doppler angle is difficult to define and measure. In order to obtain the lateral component of the blood flow velocity, a number of approaches have been proposed (Bohs et al 1995, 1998; Hein 1997; Jensen 2001; Anderson 1998).

Speckle tracking techniques have been developed that are capable of estimating lateral velocities. The two-dimensional velocity vector can be found by tracking the speckle pattern from consecutive B-mode images (Bohs et al 1995, 1998). However, the computational cost is high, the estimate is based on the essential B-mode image resolution.

Another approach is to use a three-transducer set-up to measure the three-dimensional flow vector (Hein 1997). Since the transverse movement of the blood scatterers results in a modulation of the received signal, a modified autocorrelation approach that automatically compensates for the axial velocity when determining the transverse velocity was also proposed (Jensen 2001). A similar approach has been suggested by Anderson based on spatial quadrature (Anderson 1998). The lateral velocity of a particle is estimated using a similar autocorrelation approach as was developed by Kasai et al (1985), though in order to correctly estimate the lateral velocity, the axial velocity must be estimated first so that there is compensation for the axial motion. The main drawback of these two-dimensional velocity estimators is not easy to implement on the real-time system due to the complicated algorithm (Chomas 2001).

1.4 Basics of Ultrasound Contrast Agents

In addition to conventional Doppler techniques, new techniques for ultrasonic blood flow measurements have also been developed. The use of ultrasound contrast agents is a good example (Frinking et al 2000; Goldberg 2000).

Typically, the scattered signal from blood is approximately 30-40 dB lower than that from normal tissue, and hence the signal from blood alone is difficult to detect (Shung et al., 1976). Nearly 35 year ago, Gramaik and Shah (1968) discovered that the injection of microbubbles could produce the increase in ultrasound backscatter. They injected a dye into the heart through a small bore needle to create bubbles which were detectable on a M-mode echocardiogram.

The use of these microbubble contrast agents has been shown to have significant clinical importance. Many contrast agents are either air-filled or contain gases that dissolve poorly in the blood with a mean diameter on the order of 1 to 10 μm such that they can reach the left ventricle of the heart and avoid rapid disappearance. The high echogenicity feature of microbubbles is useful in increasing the backscattered signal intensity (~15-20 dB) from blood. Increasing the echogenicity of blood allows clinicians to better measure blood perfusion in tissue and flow velocity in blood vessels, especially in recognizing malignant tumors or in monitoring treatment.

1.4.1 Commercial Contrast Agents

The primary requirements for ultrasound contrast agents are that it should be easily administered into the vascular system, be stable during diagnostic examination, have no toxicity and affect acoustic properties of tissues that determine the ultrasound imaging process. Table 1.2 shows the ideal conditions of ultrasound contrast agents. Ultrasound contrast agents might exist and act in the vascular system and they are ultimately metabolized or by their selective uptake in tissue after vascular circulation.

Table 1.2 Ideal conditions of ultrasound contrast agents.

An ideal ultrasound contrast agent
Non-toxic
Intravenously injectable, by bolus and infusion
Stable during cardiac and pulmonary passage
Remains within the blood pool or has a well-specified tissue distribution
Duration of effect comparable to that of the imaging examination

(From Becher and Burns, *Handbook of Contrast Echocardiography*, 2000)

The evolution of ultrasound contrast agents is shown in table 1.3. There are five types of contrast agents: free gas bubbles, encapsulated gas bubbles, colloidal suspensions, emulsions and aqueous solutions. The shell of contrast agent is designed to reduce diffusion into the blood and the thickness can vary from 10 to 200 nm. Attempts to maximize the persistence of the bubbles have employed high density gases with low diffusion and saturation contrast. A number of commercially produced agents are undergoing experimental and clinical investigations. Several typical contrast agents are introduced in the following paragraphs.

The first contrast agent approved for cardiac indications in the United States was Albunex^R (Molecular Biosystems, San Diego, CA). Albunex^R is biodegradable and prepared by a controlled 20 KHz sonication of 5% human serum albumin. This yields a high concentration of rather stable and very echogenic air-filled albumin microspheres. The mean microsphere diameter is 3.8 mm and 95% of these albumin-encapsulated bubbles are less than 10mm in diameter. Other microbubble stabilization methods are currently being investigated.

Table 1.3 The evolution of ultrasound contrast agents.

Generation	Formulation	Characteristics
0	Free gas bubbles	Could not traverse cardiopulmonary beds
1	Encapsulated air bubbles	Successful trans-pulmonary passage
2	Encapsulated low solubility gas bubbles	Improved stability
3	“Particular” (e.g. polymer shell) gas bubble	Controlled acoustic properties

(From Becher and Burns, *Handbook of Contrast Echocardiography*, 2000)

Levovist^{R} (SHU 508, Schering AG, Berlin, Germany) is biodegradable and made up of many crystalline galactose particles, plus a low concentration of a palmitic acid which coats the resulting air bubbles. The diameter of 99% of the bubbles is in the range 1-8 μm, which an average of 2.7 μm. Concentrations between 200 and 400mg particles per ml have been obtained. Definity^{R} (Bristol-Myers Squibb Medical Imaging, Inc.) consists of octafluoropropane-filled liposome microspheres. Mean diameter ranges from 1.1 μm to 3.3 μm. The diameter of 98% of the bubbles is less than 10 μm. Table 1.4 shows typical commercial contrast agents.

1.4.2 Mathematical Model of a Gas in a Liquid Medium

Fundamental bubble behavior can be viewed as analogous to the damped oscillations of a spring with its natural frequency. The equivalent mass is that of the liquid surrounding the bubble, with the compression-expansion of the bubble gas resembles the spring’s elastic energy process. Most theoretical models of bubble behavior are admittedly simplified. The best known mathematical description of the response of a single gaseous bubble is the Rayleigh-Plasset equation:

$$P\ddot{R} + \frac{3}{2}\dot{R}^2 = \frac{1}{\rho_l}\left[p_g - p_l - \frac{2\sigma}{R} - \frac{4\mu}{R}\dot{R}\right] \qquad (1.5)$$

R = bubble radius

$\dot{R}$ = velocity of bubble wall motion

$\ddot{R}$ = bubble boundary acceleration

P_l = ambient pressure with liquid

P_g = internal bubble gas pressure

ρ_l = liquid density

μ = liquid viscosity

σ = surface tension

There are many formations of the resonant frequency f_{reson} including Houghton's mathematical solution (Goldberg 1997). For adiabatic air bubble in water (ρ_l = 1 g/m^3 at P_l ~ 1dyne/cm^2) and, R_0 (in µm) denotes the bubble initial radius, f_{reson} (in Hz) is:

$$f_{reson} = \frac{329}{R_0} \tag{1.6}$$

For a microbubble of R_0 = 2 µm, f_{reson} ~ 1.645 MHz.

Manufacturer	Name	Gas	Shell	Status
Acusphere	AI-700	Decafluorobutane	Polymer	Pre-clinical
Alliance/Schering	Imavist	Perfluorohexne	Surfactant	Approved
Bracco	Sonovue	Sulfurhex/Fluoride	Phospholipid	Available EU
Bracco	BR14	Perfluorocarbon	Phospholipid	Clinical
Byk-Gulden	BY963	Air	Lipid	Research Only
Dupont-	Definity	Octafluoropropane	Liposome	Available USA/Canada
IMARx	Aersomes	Perfluoropropane	Lipid bilayer	Clinical
Mallinckrodt	Albunex	Air	Albumin	Available
Mallinckrodt	Optison	Octafluoropropane	Albumin	Available
Nycomed	Sonazoid	Perfluorocarbon	Lipid	Late Clinical
Point Biomedical	BiSphere	Air	Polymer bilayer	Late Clinical
Porter	PESDA	Perfluorocarbon	Albumin	Research
Quadrant	Quantison	Air	Albumin	Clinical/hold
Schering	Echovist	Air	No	Available
Schering	Levovist	Air	Fatty acid	Available
Schering	Sonavist	Air	Polymer	Clinical
Sonus	Echogen	Deodecafluoropentane	Surfactant	Withdrawn 2000

Table 1.4 Commercial contrast agent lists (from IEEE short course, Hawaii, 2003)

1.4.3 Applications of Contrast Agents

Ultrasound contrast agents have also been shown to be useful as a diagnostic tool in radiology. Microbubbles have been shown to enhance the detection of blood flow in cardiac, abdominal, peripheral and vascular structures (Forsberg et al., 1995). Evaluation of microvascular blood flow such as kidney, pancreas, liver and especially after transplants is another important application of contrast agent. Contrast-specific imaging techniques have also been proposed and they can be categorized into three groups.

The first group is based on the enhanced echo signal at the fundamental frequency. Ultrasound contrast agents improve blood flow detection and offer possibilities to visualize perfusion conditions (Navin and Reinhard 1993).

1.4.3.1 Nonlinear Response of Contrast Agents

The second group is based on the nonlinear response due to oscillation of the contrast agent. In section (1.4.2), we know the most unique characteristic of ultrasound contrast agents is their nonlinear oscillation, which has been the subject of many experimental and theoretical investigations (Shi and Forsberg 2000). Harmonic imaging techniques take advantage of the non-linear oscillations exhibited by microbubbles when they are sufficiently driven by an acoustic pulse. Nonlinear oscillations provide the opportunity to distinguish tissue and microbubble echoes based on their center frequency or response to the phase of the transmitted pulse. Imaging modes, including phase-inversion (Simpson et al 1999), sub-harmonic and ultra-harmonic modes (Lotsberg et al 1996; Shi et al 1999), exploit these nonlinear properties (as figure 1.5).

Previous research in sub-harmonic imaging shows that a pressure threshold exists for generating the sub-harmonic response. However, the pressure threshold is experimentally and theoretically observed to be low (Lotsberg et al 1996; Shi and Forsberg 2000). An optimal sub-harmonic response has been predicted when insonifying a microbubble with approximately twice its resonant frequency (Lauterborn 1976).

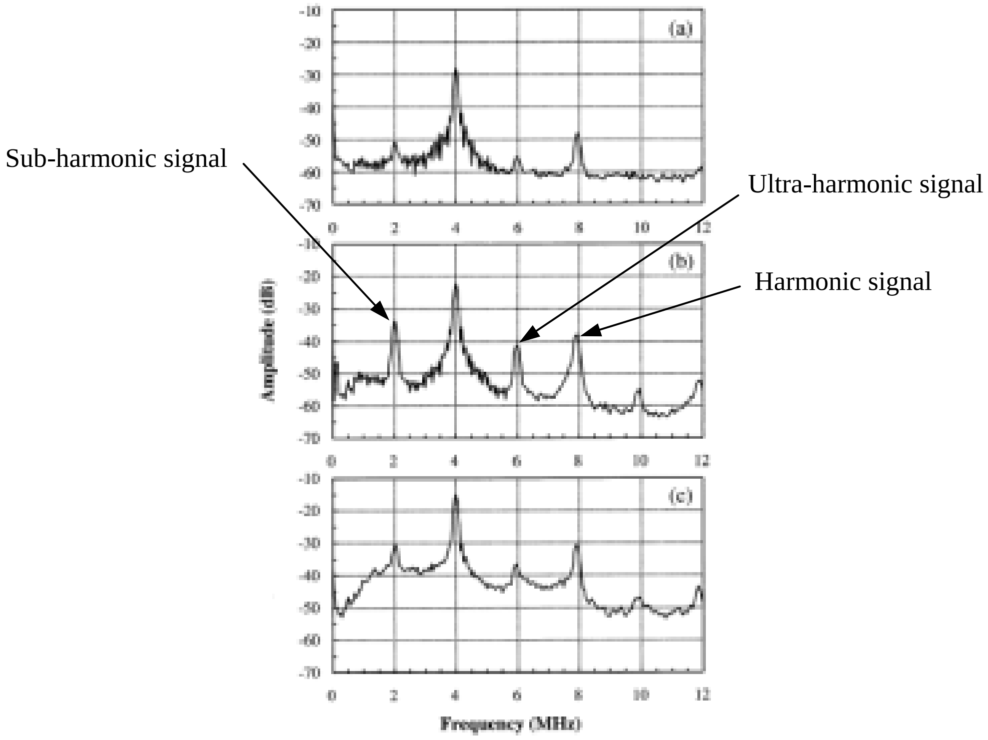

Figure 1.5 Non-linear response of ultrasound contrast agents.

(Spectra of the scattered signals from Optison^{R} microbubbles insonified at (a) 0.8 MPa; (b) 1.6 MPa; and (c) 2.4MPa. Acoustic pulses with a center frequency of 4.0MHz and a length of 32 cycles were transmitted at a PRF of 10Hz.) (From Shi and Forsberg, *Ultrasound Med. Biol.*, 2000)

Pulse inversion imaging overcomes the conflict between the requirements of contrast and resolution in harmonic imaging and provides great sensitivity. In pulse inversion imaging, two pulses are sent in succession into the tissue. The second pulse is a mirror imaging of the first (as figure 1.6). The second pulse undergoes an 180^{o} phase change. The scanner detects the echo from these two successive pulses and forms their sum. For ordinary tissue, which behaves in a linear manner, the sum of two inverted pulses is simply zero. For an echo with nonlinear components from bubbles, on the other hand, the echoes produced from these two pulses will not simple mirror images of each other, because of the asymmetric behavior of the bubble radius with time. The result is that the sum of these two echoes is not zero. Thus, a signal is detected from a bubble but not from tissue.

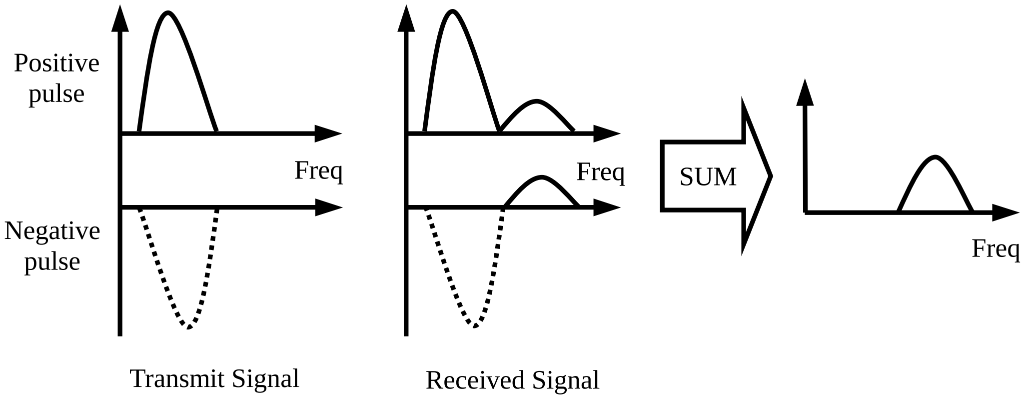

Figure 1.6 Principle of pulse inversion technique.

1.4.3.2 Contrast-Specific Techniques

The third group of contrast-specific techniques is based on dilution and destruction of microbubbles in the blood pool (Claassen et al 2001; Chen et al 1998; Hindle and Perkins 1994; Schwarz et al 1993, 1996; Ugolini et al. 2000; Wilkening et al 1999, 2000; Wilson et al 1993). One unique characteristic of ultrasound contrast agents is that they can be fragmented after proper acoustic excitation (Chomas et al 2000, 2001).

The signal enhancement effect of the contrast agent can be used to monitor concentration of the agent and to make quantitative indicator-dilution style measurements. After a dose of indicators is injected into blood, concentration of the agent is monitored as a function of time. Several recent studies have focused on *in vivo* and *in vitro* flow measurements based on the indicator-dilution theory. The indicator-dilution theory provides a mathematical model for estimating hemodynamic parameters using changes in the backscattered intensity as a function of time (i.e., the wash-out time-intensity curve, TIC) as shown in figure 1.7. It has been shown that relative change in the wash-out rate of the time-intensity curve is linearly proportional to the volume flow rate. Thus, the possibility for quantitative perfusion analysis using the time-intensity curve has been demonstrated.

Several contrast-based techniques that measure the TICs within the perfused area have been proposed. Ugolini et al. (2000) performed absolute and relative flow quantification using harmonic-power Doppler imaging, and they found a good correlation between the absolute flow and several flow parameters derived from the

TIC. However, the power Doppler mode is unreliable due to potential motion artifacts – the flow velocities may be too slow to be distinguished from tissue motion. Simpson et al. (2001) proposed a Doppler filter technique using radio frequency data to eliminate the motion artifacts.

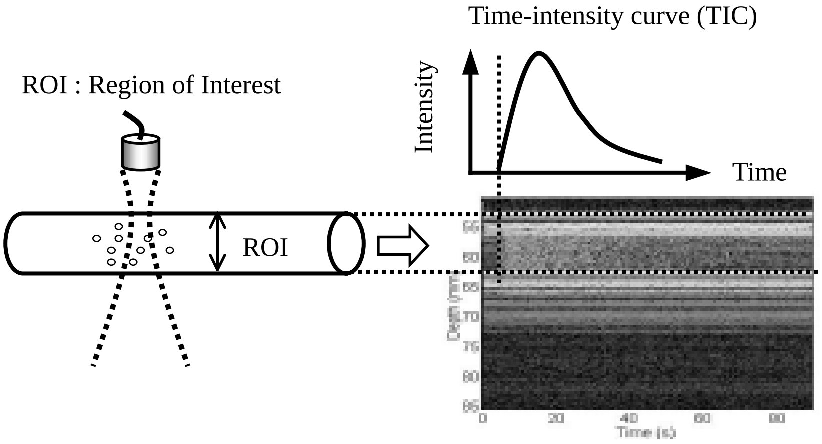

Figure 1.7 Diagram of time-intensity curve (TIC).

(From Li et al, *Ultrasound Med. Biol.,* 2002)

Wilkening et al. (1999) compared three contrast-based imaging modes (i.e., contrast harmonic imaging, contrast burst imaging, and time variance imaging) to detect the brain perfusion through the transtemporal bone window using Levovist®. These three modes were designed to detect nonlinearities and microbubble destruction. However, the high attenuation of the transtemporal bone window makes visualization of brain perfusion unreliable even at high acoustic powers.

1.5 Issues in Volume Flow Estimation

Blood volume flow rate is an important issue in medical diagnosis. The blood volume flow rate (Q) equals blood flow with velocity (v) pasting a blood vessel cross sectional area (*Area*). It can be written as

$$Q = v \times Area. \tag{1.7}$$

In ultrasound imaging system, the size of blood vessel cross section area can be obtained by B-mode scanning. If blood flow velocity is given, blood flow rate can be calculated based on equation (1.7).

1.5.1 Doppler Angle Estimation

Conventionally, the Doppler effect is used to acquire blood flow information. In this case, blood velocity is measured by detecting the frequency change of echoes backscattered from the moving blood. Despite of its wide clinical acceptance, the utility of Doppler based methods in quantitative volume flow estimation has been limited (Burns and Jaffe 1985). One of the limitations is the difficulty to obtain the beam-to-flow angle (Li et al. 2000, 2001). The Doppler based techniques can only detect the velocity component in the direction of wave propagation since projection of the velocity vector onto the transverse direction does not produce any Doppler shift, and thus the Doppler angle between the wave propagation and the flow must be known to determine the true flow velocity (as figure 1.8). Another limitation is variations of the area of a vessel over a heart cycle and flow turbulence also make quantitative flow measurements practically difficult.

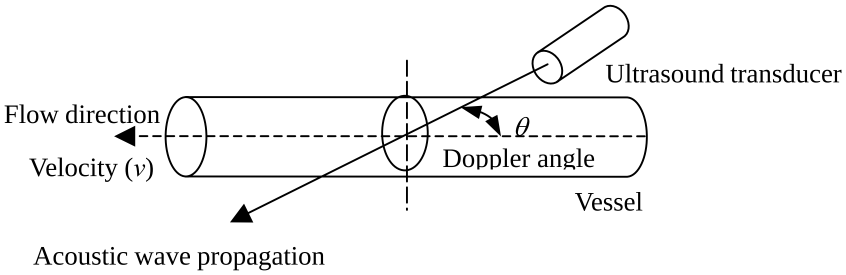

Figure 1.8 Doppler angle between wave propagation and flow direction.

1.5.2 Contrast-Specific Techniques

In addition to conventional Doppler techniques, the use of ultrasound contrast agents for blood flow measurements have also been developed. Several recent studies have focused on *in vivo* and *in vitro* flow measurements based on the indicator-dilution theory.

However, the time-intensity based methods are not as effective when the injection site is far away from the measurement site. The situation can be viewed as the case where there are more than one mixing chamber between the injection site and the measurement site. Thus, when a prolonged injection is introduced, the output time-intensity curve reflects not only the dilution process in the mixing chamber, the input must also be taken into account.

Several contrast-based techniques that measure the TICs within the perfused area have also been proposed. Since the TIC measured within the perfused area is affected by the shadowing effect, it is not a reliable method for deriving flow parameters. The shadowing effect occurs when a contrast agent passes through a perfused region and depends on the concentration of the contrast agent. In clinical conditions, it may also occur in a heart chamber or a blood vessel (Goldberg 1997). It has been shown that the shadowing effect may limit penetration of the ultrasound beam and affect visualization of myocardial layers in contrast echocardiography (Bos et al. 1996; Kaul et al. 1992).

In order to overcome the shadowing effect on perfusion estimation, a new technique in this dissertation is proposed based on both the inflow and the outflow TICs. The new technique monitors the signal enhancement at both the input and the output of a perfused region so that the shadowing effect is less significant on the inflow and the outflow TICs.

1.5.3 Major Vessels vs. Microcirculation Blood Flow Estimation

Quantitative flow measurement is a primary goal of flow imaging. It is also important in areas such as tumor diagnosis and monitoring of transplant rejection. The volume flow rate in tumors is significantly lower than in normal tissue due to the highly tortuous vessel structure and increased flow resistance in tumors (Jain 1988). Microvascular changes also occur in many disease states including cancer and diabetes. New therapies have been developed to increase or decrease angiogenesis, and imaging techniques to evaluate their performance are currently under evaluation. Therapies designed to modulate blood flow within existing vasculature have also been developed for glaucoma and a wide range of other diseases. In these new therapies, the target may either be newly formed capillaries and very small arterioles/venules whose development is immediately affected by growth factors, or more mature arteries that can dilate or constrict in response to a drug.

In order to observe microcirculation velocity within the capillaries, high-frequency ultrasound systems (>20 MHz) were recently developed to increase the spatial resolution (~50-150 μm). In addition, in order to improve sensitivity of the flow mapping system and provide opportunities to simultaneously estimate arterioles, venules and capillaries, ultrasound contrast agents are injected.

1.6 Scope and Organization of the Dissertation

The primary goal of this work is to estimate relevant parameters of blood flow and microcirculation perfusion using ultrasound. Three major topics are discussed in this dissertation.

In chapter 2, we explore the potential of Doppler angle estimation using the AR spectrum model. The proposed approach estimates the Doppler spectrum using a short data set, and the results are compared to those from the FFT-based method. Since only a small number of samples are acquired, the data acquisition time is significantly reduced and real-time two-dimensional Doppler angle estimation is possible. In addition, the flow pulsation and turbulence has been discussed. In this case, the flow velocity is time-varying and the Doppler bandwidth is affected by the temporal velocity change within the data acquisition window. Section (2.1) reviews the relationship between the Doppler bandwidth and the Doppler angle. Principles of the proposed approach are described in section (2.2). The performance of the angle estimator with simulated data is presented in section (2.3), and the experimental results are shown in section (2.4). The brief concludes in section (2.5).

Ultrasound contrast agents have been used to enhance the acoustic backscattered intensity of blood and to assist the assessment of blood flow parameters. One example is the time-intensity method based on the indicator-dilution theory. Section (3.1) reviews the contrast-specific techniques. Principles of indicator-dilution theory and relevant flow parameters are introduced in section (3.2). The self-made and commercial contrast agents adapted in this study are presented in section (3.3). The hypothesis that a blood mixing chamber is an LTI system is tested in section (3.4). Several aspects are studied. The concept of an effective mixing volume is also introduced and evaluated. To overcome the shadowing effect, a contrast-specific technique using both the input and output time–intensity relationships is proposed in section (3.5). This contrasts with conventional techniques that utilize only the relationship directly from the perfused area. The shadowing effect is also studied experimentally.

In order to improve the resolution of contrast-assisted imaging systems, we have developed high frequency destruction/contrast replenishment imaging system with a spatial resolution of 160 by 160 μm in chapter 4. The background of microbubbles destruction/reperfusion techniques is introduced in section (4.1). The methodology is presented in section (4.2) and the measurements of threshold pressure for microbubble destruction are provided in section (4.3). Section (4.4) shows the high-frequency destruction/reperfusion system. Results of *in vitro* and *in vivo* experiments are summarized in section (4.5) and (4.6), respectively. This study is concluded in section (4.7).

Chapter 5 includes the coverall discussion and conclusions regarding the three major topics. Chapter 6 provides future works.

2. Chapter 2 Doppler Angle Estimation[1]

2.1 Introduction

In this chapter, the estimation method of the beam-to-flow angle (i.e., Doppler angle) as figure 1.8 is described. An autoregressive (AR) spectral analysis technique in combination with the Doppler spectrum broadening effect is proposed to estimate the Doppler angle. Since only a limited number of flow samples are used, real-time two-dimensional Doppler angle estimation is possible. The method is validated not only for laminar flows with constant velocities but for flow pulsation and turbulence in clinical applications.

The Doppler effect resulting from ultrasound's interaction with moving red blood cells has been extensively used to determine the blood flow velocity. However, such techniques can only detect the velocity component in the direction of wave propagation since projection of the velocity vector onto the transverse direction does not produce any Doppler shift, and thus the angle between the wave propagation and the flow must be known to determine the true flow velocity.

The Doppler spectrum broadening effect was also used to find the Doppler angle. Newhouse et al. (1980, and 1987) established the transverse Doppler theory describing the relationship between the Doppler angle and the bandwidth of the Doppler spectrum. The received bandwidth of the Doppler spectrum broadens as the scatterers travel through the focused ultrasound beam within a certain period of time. Tortoli et al. (1992, and 1995) demonstrated that the maximum frequency of the measured Doppler spectrum equals the Doppler shift frequency plus one half of the spectrum bandwidth even in the presence of velocity gradient. The Doppler spectrum maximum frequency can be related to the maximum velocity in the range cell which depends on the beam-to-flow angle. Based on the classic and transverse Doppler effects, Lee et al. (1999) proposed a Doppler angle and flow velocity estimation method for both constant and pulsatile flow measurements.

---

[1] The Chapter is based on the work presented at *IEEE UFFC*, 2002 and *Ultrasonic Imaging*, 2002.

2.1.1 Doppler Spectrum Estimation

It has been shown that the Doppler bandwidth is inversely proportional to the transit time of a scatterer crossing the ultrasound beam (Jones and Giddens 1990; Li et al 2000; Newhouse et al 1980, 1987; Tortoli et al 1994). This has been described as the transit time spectrum broadening effect, and several methods have been proposed for determining the Doppler angle from the resulting Doppler bandwidth (Newhouse et al 1980, 1987). The Doppler bandwidth has also been derived theoretically for a flow moving transversely to the beam axis of a transducer.

2.1.1.1 Fast Fourier Transformation (FFT)

The fast Fourier transform (FFT) is the most commonly used signal processing technique for Doppler spectrum estimation. One problem with this approach is that a long data acquisition time is required to achieve adequate spectral resolution and reduce the bias and variance of the estimates (David et al 1991; Jensen 1996). Furthermore, if the data acquisition time (i.e. the observation time) is smaller than the transit time, the dependence of the Doppler bandwidth on the Doppler angle no longer exists. Thus, the requirement of a long data acquisition time renders the FFT-based method unsuitable for real-time two-dimensional Doppler imaging.

2.1.1.2 Correlation-Based Method

To overcome the problem based on FFT method, a correlation-based method has been proposed for Doppler angle estimation (Kasai et al 1985; Li et al 2000). Specifically, the variance of the Doppler spectrum is used to approximate the square of the Doppler bandwidth. In a color Doppler imaging system, the variance of the Doppler signal is routinely calculated using only a small number (e.g. 4–12) of flow samples. Compared to the FFT-based method, this represents a significant reduction in the data acquisition and makes real-time two-dimensional Doppler angle estimation possible.

Although it has been shown that the correlation-based method can be used for accurate angle estimation using only four flow samples, variance averaging must then be applied (Li et al 2000). The variance averaging can be performed either temporally or spatially. If temporal averaging is used, the correlation-based method is primarily restricted to constant velocity flows. For spatial averaging, on the other hand, the method is affected by the velocity gradient. Thus, clinical applications of the correlation-based method are not yet practical unless the effects of temporal and spatial variations of the flow can be taken into account.

2.1.1.3 Parametric Spectral Estimation Method

Parametric spectral estimation methods have previously been suggested for Doppler spectrum estimation (Kaluzynski 1987, 1989; Keeton et al 1997; Schlindwein and Evans 1990; Vaitkus et al 1988). One advantage of these methods is that high spectral resolution can be achieved using a short data set for nonstationary flows. In other words, new samples can be predicted based on previous samples if the signal model can be accurately estimated.

David et al. compared the conventional FFT-based method with three parametric spectral estimation techniques under a variety of signal-to-noise ratio and signal bandwidth conditions (David et al 1991). If the model order was chosen appropriately, the parametric spectral analysis techniques were shown to be superior to the Fourier techniques in most circumstances. The criteria for selecting an optimal model order and its corresponding clinical significance have been studied extensively (Kaluzynski 1987, 1989; Schlindwein and Evans 1990). It has also been suggested that it is feasible to implement real-time AR spectral analysis in diagnostic ultrasound (Schlindwein and Evans 1989). Note that the AR spectral analysis approaches found in the literature are somewhat restrictive, in that they are generally used to extract certain features of the blood flow signal under specific conditions only.

2.1.2 Motivation and Goal

The primary purpose of the study was to explore an AR method for real-time Doppler angle estimation which dispenses with the need for temporal averaging. Specifically, the autoregressive (AR) spectral analysis technique was used to estimate the Doppler spectrum from a small number of flow samples. Nonetheless, since the general features of the Doppler spectrum (e.g. center frequency and bandwidth) are still of primary interest, the AR coefficients are used here only for data extrapolation: the Doppler spectrum is still calculated using the FFT.

In clinical applications, flow pulsation and turbulence need to be considered. In this case, the flow velocity is time-varying and the Doppler bandwidth is affected by the temporal velocity change within the data acquisition window. The AR method proposed by Yeh and Li (2002) is expected to outperform the conventional FFT method since the shorter data acquisition time required by the AR method is less affected by the temporal velocity change.

Another issue for Doppler bandwidth estimation is the interference caused by multiple scatterers within the sample volume. Ideally, the transit time and corresponding Doppler bandwidth can be accurately estimated if there is only a single scatterer crossing the acoustic beam. In practice multiple scatterers are present, and the interference among them may affect Doppler bandwidth estimation. This phenomenon is illustrated in figure 2.1.

The top panel of figure 2.1(a) shows the grayscale M-mode image of the envelope of a radio-frequency (RF) signal from a single scatterer crossing the sample volume with a dynamic range of 40 dB. Each vertical line in this panel corresponds to the envelope of the received signal along the axial direction. Such signals are repetitively obtained at a rate defined by the pulse repetition frequency, and are plotted along the horizontal axis. For a particular depth or within a certain range gate, the signal along the horizontal direction is also known as the Doppler signal. The signal can be either in the RF range or in baseband. Note that if a range gate is used, axial averaging of all the signals within the gate is performed. The Doppler signal corresponding to the range gate 68–70 mm from the signal shown in the top panel of figure 2.1(a) is shown in the middle panel. The bottom panel shows the corresponding Doppler spectrum. Note that the Doppler signal is a discrete signal with the sampling rate defined by the pulse repetition frequency. For a single scatterer, the transit time is the length of the time interval along the horizontal direction during which a strong Doppler signal is observed. The transit time defined by the envelope of the Doppler signal shown in the middle panel is inversely proportional to the Doppler bandwidth shown in the bottom panel.

The three panels of figure 2.1(b) have the same format as figure 2.1(a) except that there are now two scatterers crossing the sample volume. The lower two panels demonstrate that both the envelope of the Doppler signal and the Doppler bandwidth are affected by the presence of more than one scatterer. The mean Doppler frequency, on the other hand, is relatively unchanged. Thus, a significantly different bandwidth is found although the true Doppler angle remains unchanged.

Figure 2.1(c) shows the results in a realistic case where multiple scatterers are present. Again, both the transit time and the Doppler bandwidth are affected due to the interference from multiple scatterers. Thus, the estimated Doppler angle will be incorrect. However, if the Doppler spectrum is obtained by extrapolating a small data set, such interference may be reduced without affecting the spectral resolution. The advantage of the AR method may be more pronounced for a smaller Doppler angle, since the transit time is longer in this case.

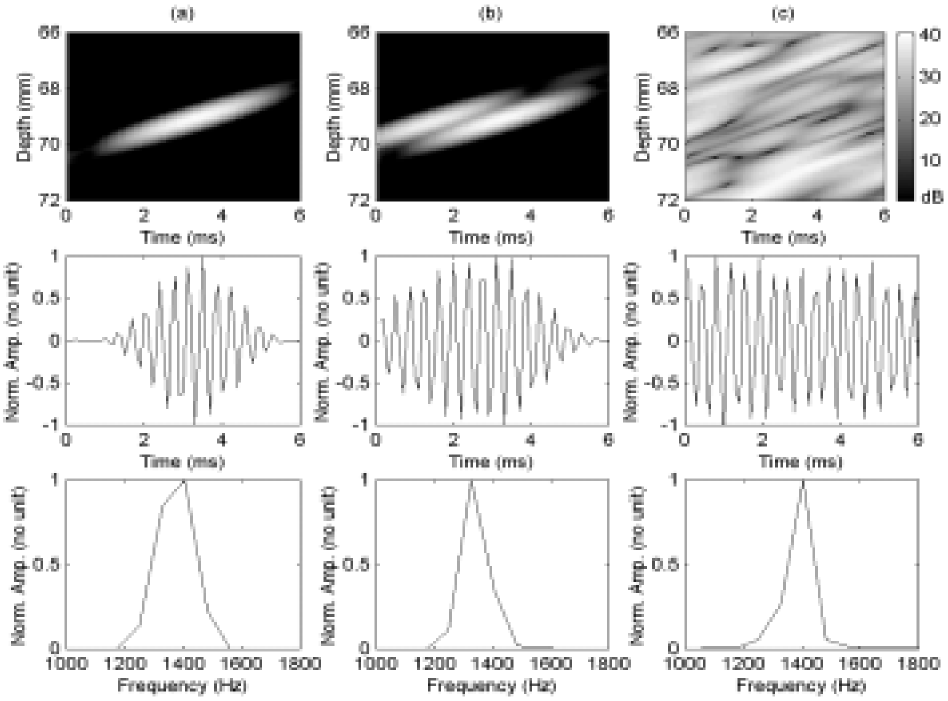

Figure 2.1 M-mode, Doppler signal, and Doppler spectrum (from top to bottom) for (a) one scatterer, (b) two scatterers, and (c) multiple scatterers. Normalized amplitudes (Norm. Amp.) are shown.

2.2 Theory

2.2.1 Basic Principles of Doppler Angle Estimation

The velocity of blood flow can be measured by detecting the Doppler frequency shift of echoes backscattered from blood. The Doppler frequency shift (f_d) is related to the flow velocity (please refer to equation (1.3)) by

$$f_d = \frac{2v}{\lambda}\cos\theta, \tag{2.1}$$

where v is the flow velocity, λ is the acoustic wavelength, and θ is the Doppler angle. The term $v \cdot cos\theta$ is the axial flow component of the velocity vector, which is what is computed by most blood velocity estimators.

It is known that the Doppler bandwidth (bw) is inversely proportional to the transit time of an acoustic scatterer crossing the sample volume (Newhouse et al 1980, 1987). The relation is given by

$$bw = \kappa\frac{v \cdot \sin\theta}{w}, \tag{2.2}$$

where κ is a scaling factor and w is the beam width. Given a particular Doppler spectrum and the acoustic beam geometry, the Doppler angle can be determined from (Li et al 2000; Newhouse et al 1980, 1987; Tortoli et al 1994)

$$\theta = \tan^{-1}\left(\frac{w \cdot bw}{\kappa \cdot v \cdot \cos\theta}\right). \tag{2.3}$$

Equation (2.3) indicates that the accuracy of Doppler angle estimation is determined by the accuracy of the spectrum estimation.

In equation (2.3) it is assumed that the observation time is longer than the transit time, and that the velocity is constant within the sample volume. In practice, however, the Doppler spectrum is broadened due to spatial velocity variations (i.e. velocity gradient) in the blood vessel. To overcome this problem, Tortoli et al. demonstrated that in the presence of a velocity gradient, the maximum Doppler frequency fmax is unchanged (Tortoli et al 1995). Thus, the maximum Doppler frequency can be used to derive the Doppler angle:

$$\theta = \tan^{-1}\left(\frac{f_{\max} - f_p}{f_p} \cdot \frac{2F}{W}\right), \tag{2.4}$$

where f_p is the frequency at which the Doppler spectrum has its maximum intensity, F is the transducer focal length, and W is the transducer width (Lee et al 1999).

2.2.2 Doppler Angle Estimation Using AR Model

As mentioned in section (2.1.2), this study used the traditional FFT-based method to estimate the Doppler spectrum, but here the AR method is used for data extrapolation. Based on the AR model, the value of a Doppler signal $y(n)$ can be described by a linear combination of previous values of the same Doppler signal and a white-noise input (Kay 1988). Note that the Doppler signal is discrete by definition. For a p-th order AR model, we have

$$y(n) = e(n) - a_1 y(n-1) - a_2 y(n-2) - \cdots - a_p y(n-p), \qquad (2.5)$$

where $e(n)$ is a white, stochastic signal driving the AR process, and the $a_i{}'s$ are the parameters. The variance of $e(n)$ and the $a_i{}'s$ can be estimated by solving the Yule–Walker equations. Future values of the Doppler signal can be extrapolated once these parameters are computed. In other words, given the Doppler signal for $y(n-1)$ to $y(n-p)$, the Doppler signal for $y(n)$ to $y(n+q)$ can be extrapolated if the $a_i{}'s$ are assumed to be estimated accurately. Three major issues need to be addressed when implementing the AR model.

2.2.2.1 AR Model Selection

The first is selection of the model order p; if it is too low, not all features of the signal can be described; whereas if the order is too high, false peaks and line splitting may be present (Kaluzynski 1989; Schlindwein and Evans 1990). The order selection criterion is discussed in section (2.3.1).

2.2.2.2 Aspect Ratio of Sample Volume

The second issue relates to the aspect ratio of the sample volume, which is defined as

$$aspect \quad ratio = \frac{l}{w}, \qquad (2.6)$$

where l is the sample volume length (i.e. length of the Doppler range gate). For a ratio of 1, the sample volume on the image plane becomes circular. Thus, the Doppler bandwidth is relatively constant since the transit time does not change as a function of the Doppler angle. For a large aspect ratio (e.g. 5), the relationship between the bandwidth and $\sin\theta$ is approximately linear at large Doppler angles (Li et al 2000).

2.2.2.3 Doppler Signal Extrapolation

The third issue is selection of the Doppler signal to be extrapolated. To ensure that the extrapolated signal can be used to obtain an accurate estimate of the Doppler bandwidth, the flow data must be selected carefully.

Assuming that a p-th order AR model is used, the p flow samples are used for Doppler angle estimation if the following two conditions are satisfied simultaneously: (1) one of the flow samples must correspond to a maximum in the axial direction so that good signal-to-noise ratio is guaranteed, and (2) the signal intensity of the flow samples increases and reaches a peak before it starts to decrease along the horizontal direction. The second criterion implies that the scatterers of interest cross the center of the beam during the observation time. The criteria are graphically demonstrated in figure 2.2.

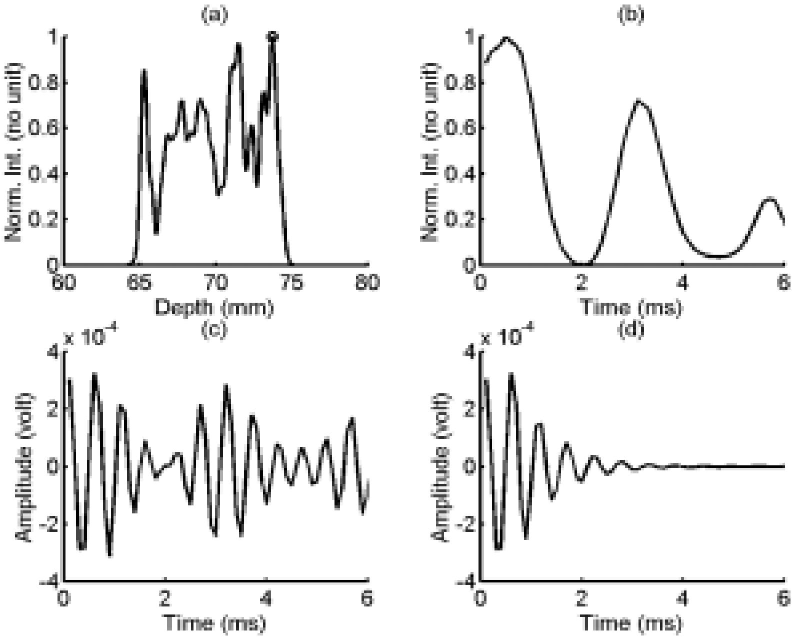

Figure 2.2 Selection of the Doppler signal. (a) Signal intensity (vertical direction). (b) Doppler signal intensity (horizontal direction). (c) Original Doppler signal. (d) Extrapolated Doppler signal. “Norm. Int.” represents the normalized intensity.

The circle in figure 2.2(a) corresponds to a maximum along the axial direction. Figure 2.2(b) shows the Doppler signal intensity at the depth defined in figure 2.2(a), where the intensity is defined as the square of the signal amplitude after baseband demodulation. The intensities in figure 2.2(a) and (b) are normalized such that the peak value is one. In this case, a peak is found in the first few samples and hence the flow samples can be used. Figure 2.2(c) corresponds to the original Doppler signal. The extrapolated Doppler signals using the first eight samples are shown in figure 2.2(d). It is expected that the data selection process can effectively select valid Doppler samples and reduce interference from multiple scatterers. This study uses –6 dB bandwidths of the Doppler spectra in equation (2.3).

2.3 Simulation Methods and Results

2.3.1 Simulation Model: Velocity with Spatial Changes

To test the proposed approach, simulated data were generated using the model developed by Kerr and Hunt (1992). The model takes into account both amplitude and temporal responses from a given transducer geometry. The acoustic response of each scatterer is calculated using the acoustic impulse response method. In other words, the transducer output $V(t)$ can be expressed as

$$V(t) = \xi \cdot P_e(t) * h_r(\vec{r}, t) * h_t(\vec{r}, t), \tag{2.7}$$

where ξ is a constant and $*$ denotes the convolution operator. The pulse-echo response $P_e(t)$ is assumed to be Gaussian, $h_r(\vec{r}, t)$ and $h_t(\vec{r}, t)$ are the receive and transmit acoustic impulse responses, respectively. The model assumes that point scatterers are randomly distributed in a two-dimensional grid.

In the simulations, the transducer was a linear array with a center frequency of 5 MHz and an aperture size of 19 mm. The sample volume was located at the focal point, which was 70 mm from the transducer (i.e., F number was 3.7). The corresponding pulse-echo –6 dB beam width at the focal point was approximately 1 mm. The sound velocity was 1540 m/s and the pulse repetition interval was 100 μs. For the AR method, eight original flow samples were extrapolated to 64 samples, which were then Fourier transformed to obtain the Doppler spectrum. The spectrum was also compared to the spectrum obtained by Fourier transforming 64 original flow samples. The dependence of the Doppler angle, the aspect ratio, and the flow velocity on Doppler bandwidth estimates was studied. Both constant flows and flows with spatially varying velocity were simulated.

The order of the AR model was selected such that the prediction error (*PE*) was minimized. The prediction error is given by

$$PE(p) = E\left\{ (y(n) - \hat{y}(n \mid p))^2 \right\}, \tag{2.8}$$

where $y(n)$ is the original data and $\hat{y}(n \mid p)$ is an extrapolated data set based on a p-th order AR model. The typical prediction error as a function of the model order is shown in figure 2.3. By definition, *PE*(1) was 100%. The *PE*(*p*) curve shows that the prediction error decreases as the model order increases. Figure 2.3 shows that the maximum value of the prediction error was approximately constant for orders of 8 and higher, so an eighth-order AR model was chosen for extrapolation of the data.

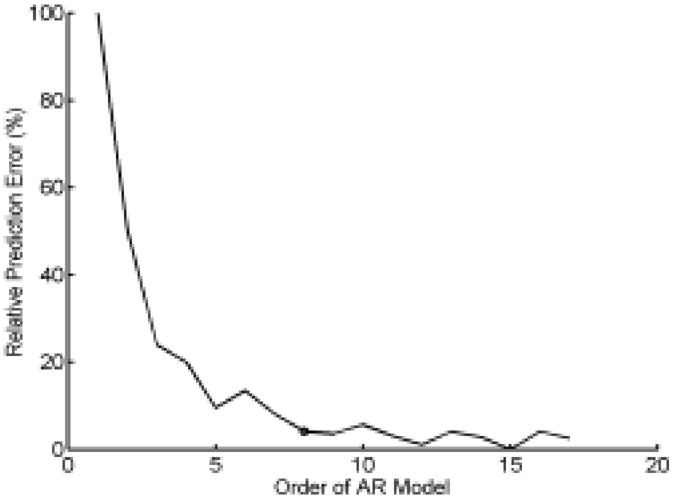

Figure 2.3 Relative prediction error as a function of AR model order.

Figure 2.4 shows the effects of the aspect ratio on the –6 dB Doppler bandwidth estimates using the AR method. The scatterers were assumed to be flowing at constant velocity, and three aspect ratios were investigated. The Doppler bandwidth estimates for an aspect ratio of 1 are shown as the dashed lines. Results for aspect ratios of 3 and 5 are shown as the solid lines with circles and dotted lines, respectively. Finally, the solid lines denote the theoretical values (i.e. an infinite aspect ratio). Figure 2.4(a)-(d) presents results obtained for velocities of 30, 40, 50, and 60 cm/s, respectively. For an aspect ratio of 5, the mean errors of the Doppler angle estimates (from 30° to 75°) with the four velocities were 2.71°, 1.65°, 1.64°, and 1.61°, respectively. Figure 2.4 shows that a good agreement between the AR method and the theoretical values predicted by equation (2.3) was found at large Doppler angles and high velocities for all values of the aspect ratio. However, at lower Doppler angles there was a significant deviation between the predicted and theoretical values for aspect ratios smaller than 5, suggesting that low values may be inadequate for Doppler angle estimation. This is due to the fact that with a small aspect ratio, the path length along the flow direction quickly deviates from the assumed value as the Doppler angle decreases from 90° (Li et al 2000).

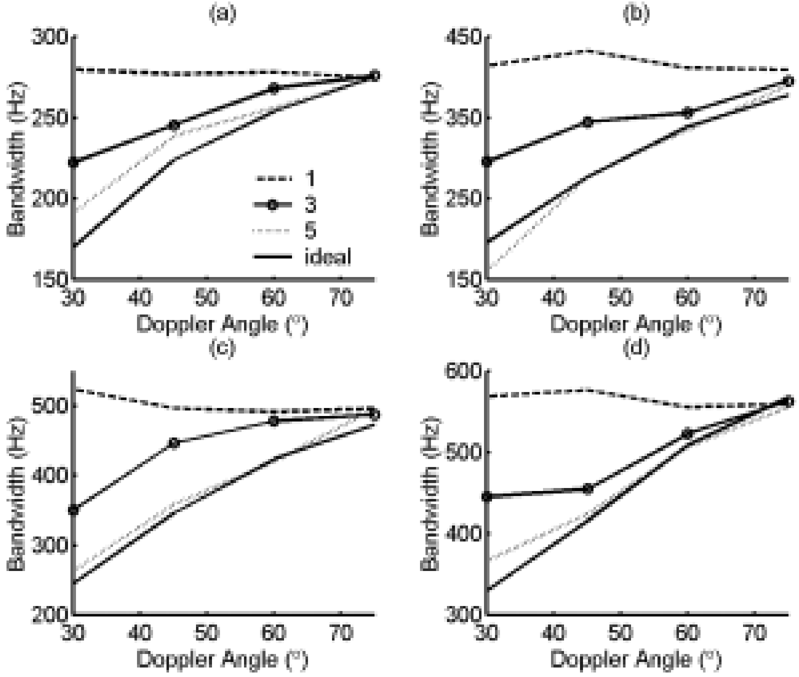

Figure 2.4 Effects of aspect ratio and flow velocity on Doppler bandwidth estimation: (a) 30 cm/sec, (b) 40 cm/sec, (c) 50 cm/sec, and (d) 60 cm/sec. The true Doppler bandwidth is plotted with the solid line, and the estimates for aspect ratios of 1, 3, and 5 are plotted with a dashed line, a solid line with circles, and a dotted line, respectively.

2.3.1.1 Flow with Constant Velocity

The results from the AR method were compared with those from the conventional FFT method. The estimates of the Doppler frequency shift and bandwidth for Doppler angles between 30^o and 75^o are shown in figure 2.5. The theoretical values, based on equations (2.1) and (2.2), are also shown in the figure. The flow velocity was 35 cm/s and the aspect ratio was 5. For each estimate, three sets of Doppler signals from three different locations within the sample volume were used based on the selection criteria described in section (2.2.2). The three estimates were then averaged. The results shown for the FFT method were also the average of the three estimates from the same locations. Figure 2.5 shows that the AR and FFT methods produce a reasonable agreement with the theoretical values of both the Doppler bandwidth and the Doppler frequency shift.

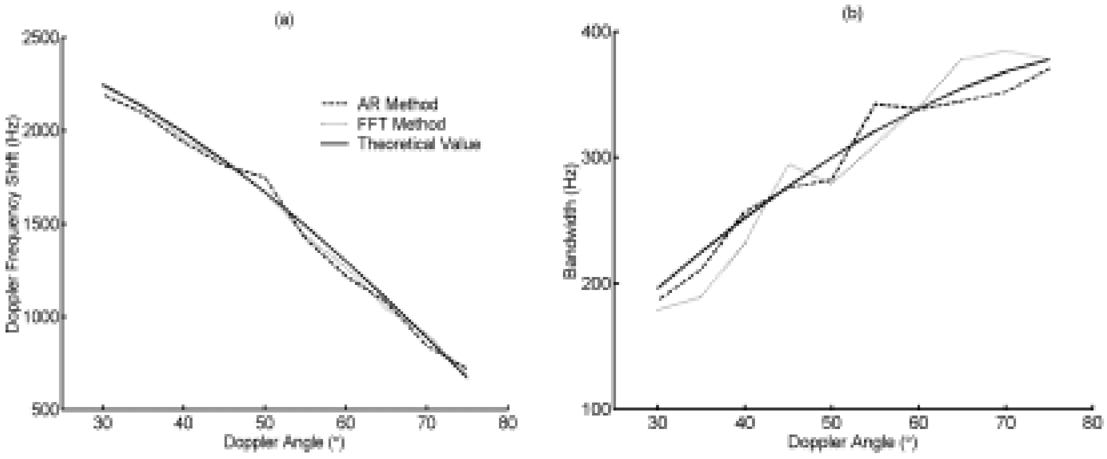

Figure 2.5 The AR method vs. the conventional FFT method, in terms of (a) Doppler frequency shift and (b) Doppler bandwidth. The solid lines show theoretical values, dashed lines are for the AR method, and dotted lines are for the FFT method.

The FFT method requires that the observation time is longer than the transit time. Therefore, the following condition must be satisfied,

$$v \cdot (N-1) \cdot PRI \geq \frac{w}{\sin\theta}, \tag{2.9}$$

where N is the number of flow samples and PRI is the pulse repetition interval. Equivalently, equation (2.9) can be written as

$$\theta \geq \sin^{-1}\left(\frac{w}{v(N-1)PRI}\right) \equiv \theta_c, \tag{2.10}$$

where θ_c is defined as the critical angle. The Doppler angle must be greater than θ_c so that equation (2.3) can be applied. For the AR method, only eight flow samples were used in this study, with the remaining flow values being obtained by extrapolation. Thus equation (2.10) is no longer applicable.

The effects of the critical angle on the results of the AR method, the FFT method, and the theoretical values are shown in figure 2.6. The Doppler angle varied from 20^o to 75^o. The flow velocity was constant at 40 cm/s, and the critical angle was 24^o according to equation (2.10).

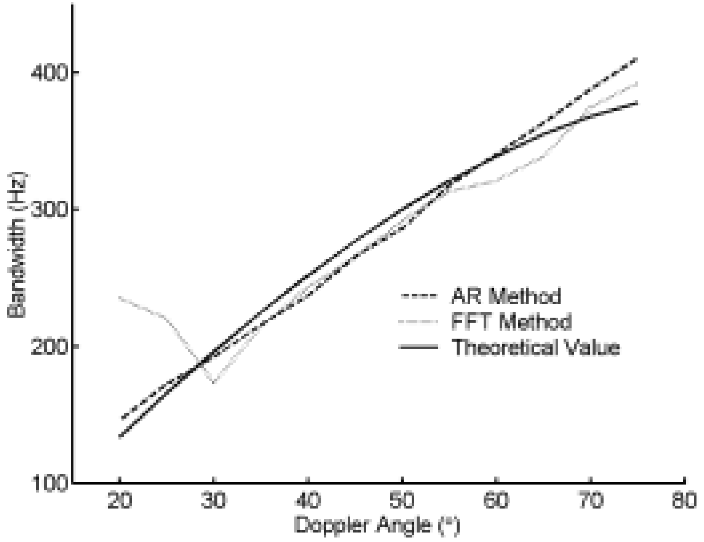

Figure 2.6 Bandwidths estimated with the AR model (dashed line) and the FFT method (dotted line) with constant flows. The solid line shows the theoretical values.

The figure shows that at small Doppler angles the FFT-based method was less accurate than the AR method. The variable κ was set to 1.05 so that the Doppler bandwidth estimates and the corresponding Doppler angles could be obtained. The AR method had an average estimation error of 1.91^o and a standard deviation of 1.24^o, whereas the FFT method had an average error of 3.96^o and a standard deviation of 5.15^o. Figure 2.6 also shows that although the observation time is smaller than the transit time, extrapolation of the AR method effectively results in accurate bandwidth estimates, provided that proper Doppler signals and a model with a high-enough order are used. Note that for high Doppler angles there was a tendency for the angle estimates from the AR method to deviate far from the theoretical values. This is due to the projected velocity component along the wave propagation direction (i.e., $v \cdot \cos\theta$) being smaller for larger Doppler angles. Thus the Doppler angle estimates are more affected since the angle is inversely proportional to the projected velocity based on equation (2.3).

2.3.1.2 Flow with Velocity Gradients

The simulations described in section (2.3.1.1) were based on constant flows. In practice, the velocity gradient should not be ignored, and so simulations of flows with spatially varying velocity were also performed. The velocity V_s in a vessel can be expressed by

$$V_s = V_{\max}\left[1-(\frac{r_i}{r})^n\right], \tag{2.11}$$

where n is a constant, r is the vessel radius, V_{max} is the maximum flow velocity, and r_i is radial distance relative to the vessel center. The constant n in the flow model was set to 2, and the maximum flow velocity V_{max} was 40 cm/s. The critical angle in this case was again 24$^{\text{o}}$.

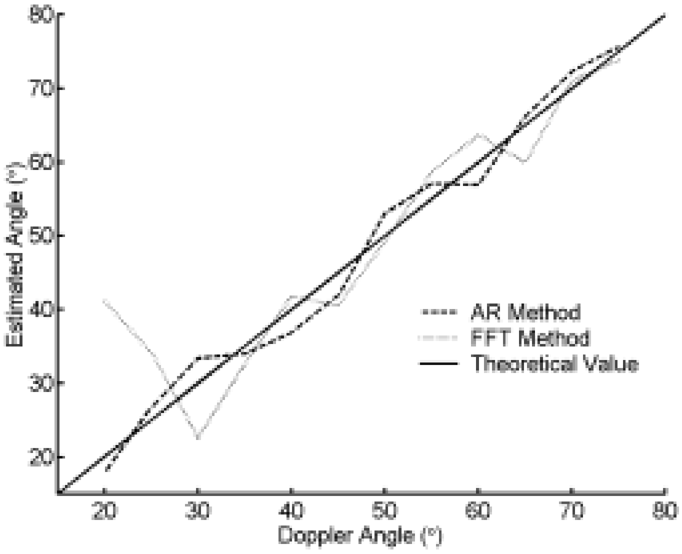

Figure 2.7 Doppler angles estimated with the AR model (dashed) and the FFT method (dotted line) for flows with spatially varying velocity. The solid line shows the theoretical values.

The Doppler angle was estimated using equation (2.4) to minimize the effects of the velocity gradient. The results for Doppler angles from 20^o to 75^o are shown in figure 2.7, which includes the theoretical values obtained from equation (2.3). The AR method had an average estimation error of 2.3^o and a standard deviation of 2.52^o, whereas the FFT method had an average error of 5.2^o and a standard deviation of 7.65^o. As for figure 2.6, the AR method outperformed the FFT method at smaller Doppler angles.

Both constant flows and flows with spatially varying velocity were studied: the estimation errors for flows with spatially varying velocity were generally larger than those for constant flows, indicating that the velocity gradient associated with a flow had a noticeable impact on the estimation results. The effects of the velocity gradient on the AR-based Doppler angle estimation method were further investigated using simulations.

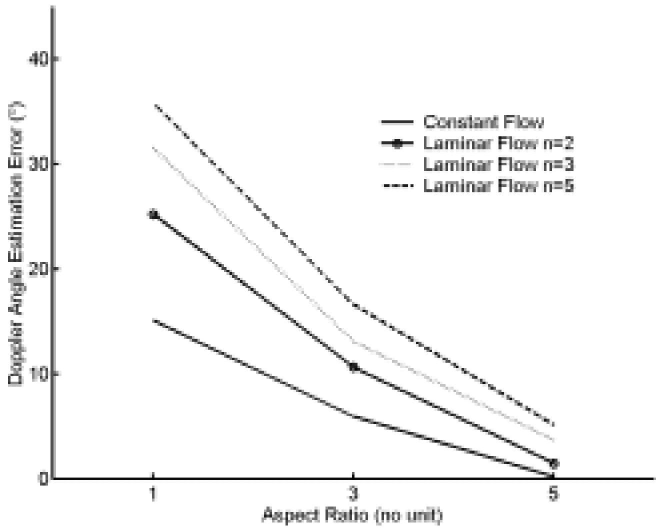

Figure 2.8 Effects of aspect ratio and velocity gradient on Doppler angle estimation using the AR method. The estimate error for constant flows is shown by the solid line, and the flows with spatially varying velocity for flow models with orders of 2, 3, and 5 are plotted with a solid line with circles, a dotted line, and a dashed line, respectively.

In these simulations, three flows with spatially varying velocities with orders (i.e. *n* as defined in equation (2.11)) of 2, 3, and 5 were employed. The maximum flow velocity was 40 cm/s, and the Doppler angle was 30^o. A constant flow with the same velocity was also included. The results are given in figure 2.8, which show that the estimation error increases with the order. The estimation error also decreases with the aspect ratio. This is consistent with the results shown in figure 2.4, despite a larger aspect ratio generally producing larger velocity gradients when the beam width is assumed to be fixed.

2.3.2 Simulation Model: Velocity with Temporal and Spatial Changes

Simulations of pulsatile flows were performed to test the proposed approach. The simulation model consisted of two parts. The first part included blood scattering and the acoustic point spread function. The response of each scatterer was calculated using an acoustic impulse response method as described in section (2.3.1) (Kerr and Hunt 1992). The second part was for the time-varying velocity profile of pulsatile flows (Evans 1982; Jensen 1996). The velocity at a particular point in the vessel changed with time due to flow acceleration and deceleration. In this section, the flow velocity profiles emulated flows in the carotid artery.

In the simulations, the transducer was a linear array with a center frequency of 3.5 MHz and a 19 mm aperture size. The sample volume was located at the focal point, which was 70 mm away from the transducer. The corresponding pulse-echo –6 dB beam width was about 1.4 mm at the focal point. The sound velocity was 1540 m/s and the PRI was 150 μs. The heart rate was 80 per minute (i.e., the duration of a heart cycle equaled 0.75 s). Figures 2.9(a)-(d) represent the temporal velocity distributions during a single cardiac cycle with the mean velocities at 3, 9, 15, and 21 cm/s, respectively. The Doppler angle in this case was 45^0. Note that inverted brightness is displayed in figures 2.9 (a)-(d) (i.e., the signal intensity increases as the display brightness decreases).

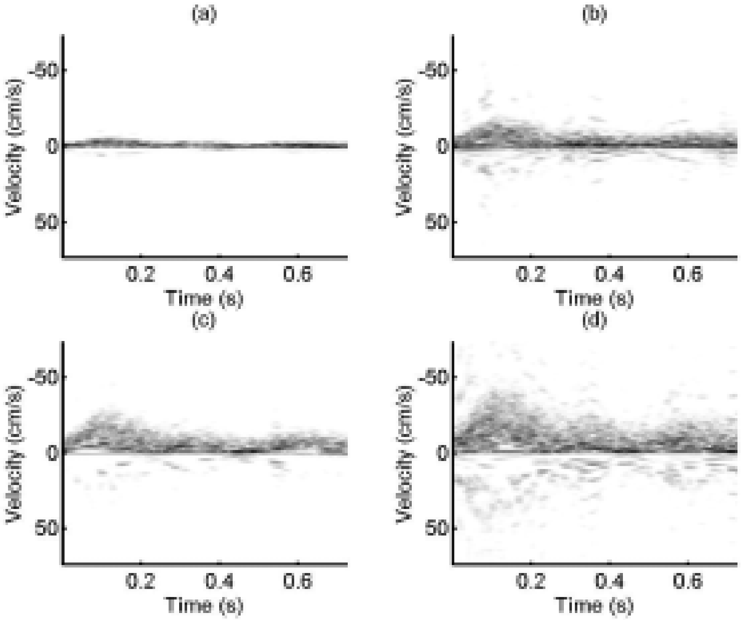

Figure 2.9 Velocity distribution with mean velocities at (a) 3 cm/s, (b) 9 cm/s, (c) 15 cm/s, and (d) 21 cm/s. The Doppler angle was 45^0. Note that inverted brightness is displayed (i.e., the signal intensity increases as the display brightness decreases).

2.3.2.1 Flow Pulsation

The results of Doppler angle estimation using the AR method and the FFT method are shown in figures 2.10 and 2.11, respectively. In each figure, panels (a)-(d) represent the results at mean velocities of 3, 9, 15, and 21 cm/s, respectively. Totally, fifteen Doppler angle estimates were obtained within the duration of a heart cycle. The actual Doppler angles (i.e., 45^o) are shown as the horizontal dashed lines. The asterisks represent the estimated Doppler angles. The AR method had an average estimation error of 2.61^o and a standard deviation of 3.19^o, whereas the FFT method had an average error of 5.41^o and a standard deviation of 6.16^o.

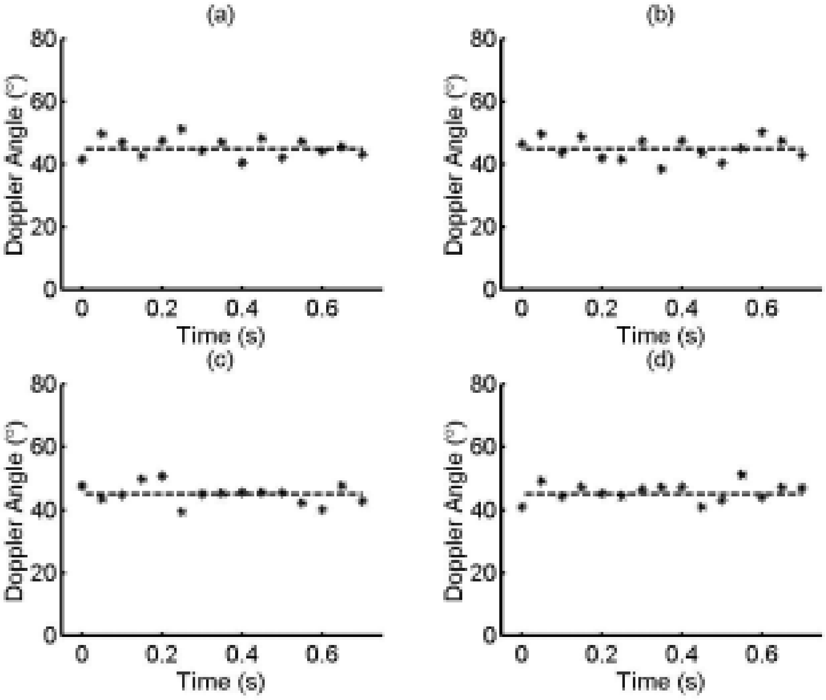

Figure 2.10 Simulation results of the estimated Doppler angles using the AR model with the mean velocities at (a) 3 cm/s, (b) 9 cm/s, (c) 15 cm/s, and (d) 21 cm/s. The Doppler angle was 45^0.

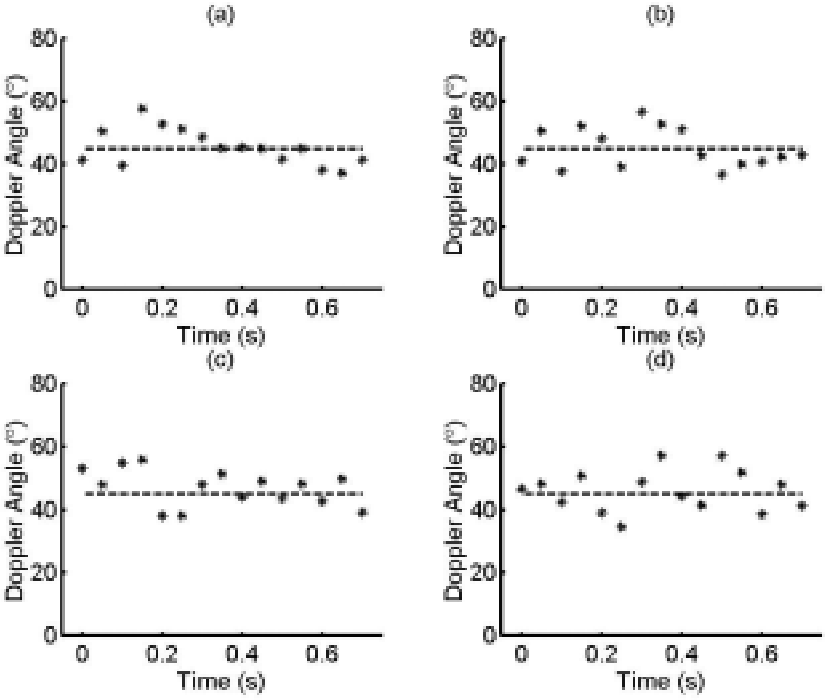

Figure 2.11 Simulation results of the estimated Doppler angles using the conventional FFT method with the mean velocities at (a) 3 cm/s, (b) 9 cm/s, (c) 15 cm/s, and (d) 21 cm/s. The Doppler angle was 45^0.

Different Doppler angles were also considered in this study. The Doppler angle varied from 30^o to 78^o. Other ultrasonic parameters were the same as those used in previous simulations. The means and the standard deviations of the estimation errors were summarized in table 2.1. Tables 2.1 (a) and (b) show the Doppler angle estimates using the AR method and the FFT method, respectively. The simulation data for the AR method had an average estimation error of 2.39^o and an average error of 6.07^o for the FFT method. The results indicate that the AR method provides more accurate Doppler angle estimates than the FFT method. This is because that the AR method only uses 8 Doppler signals, whereas the FFT method uses 64 Doppler signals. Hence, the AR method is less affected by the temporal velocity change.

Table 2.1 Summary of the errors of Doppler angle estimation using (a) the AR method and (b) the FFT method with simulation data. All results are mean ± one standard deviation.

(a)

Doppler angle	**Mean velocity (cm/s)**			
(^{o})	**3**	**9**	**15**	**21**
30	2.42 ± 2.78	1.87 ± 2.24	2.00 ± 2.87	2.50 ± 3.14
45	2.71 ± 3.17	3.03 ± 3.56	2.35 ± 3.19	2.35 ± 2.83
55	2.44 ± 3.20	3.09 ± 3.56	1.87 ± 2.51	2.01 ± 2.38
65	2.58 ± 3.16	2.69 ± 3.83	2.78 ± 3.39	2.17 ± 2.53
78	2.93 ± 3.82	1.66 ± 1.88	2.30 ± 3.18	2.10 ± 2.58

(b)

Doppler angle	**Mean velocity (cm/s)**			
(^{o})	**3**	**9**	**15**	**21**
30	7.45 ± 5.56	6.54 ± 5.24	5.96 ± 4.58	6.58 ± 5.19
45	5.48 ± 5.85	5.54 ± 6.32	5.16 ± 5.80	5.47 ± 6.66
55	5.75 ± 8.54	6.81 ± 7.53	7.31 ± 8.54	6.34 ± 5.45
65	5.81 ± 6.45	5.84 ± 6.56	5.57 ± 6.82	5.15 ± 4.87
78	7.23 ± 4.87	6.63 ± 7.98	6.04 ± 5.68	4.78 ± 5.91

2.3.2.2 Flow Turbulence

Turbulent flows may be present in clinical applications of Doppler angle estimation. In the cardiovascular system, for example, turbulence has been associated with poststenotic dilatation, aneurysms, atherogenesis and thrombosis (Bascom et al 1993; Cloutier et al 2001). With turbulent flows, significant velocity variations exist within the sample volume. In this case, the Doppler angle estimation using the AR method or the FFT method is similarly affected by the spatial flow velocity changes. The Doppler angle estimates in turbulent flows using the AR and the FFT methods were investigated using simulations.

Because the turbulence is an irregular eddying motion occurring about the mean velocities, random velocity components were used to generate the Doppler signal (Cloutier et al 2001). In the simulations, the Doppler signal in the presence of turbulence is simulated by having the scatterers within the sample volume move with a two-dimensional random displacement between two firings. A maximum flow velocity was set in advance. In other words, the velocities of the scatterers between two firings were random distributions within the maximum flow velocity and the moving directions of the scatterers between two firings were random distributions ranging from 0 to 2π.

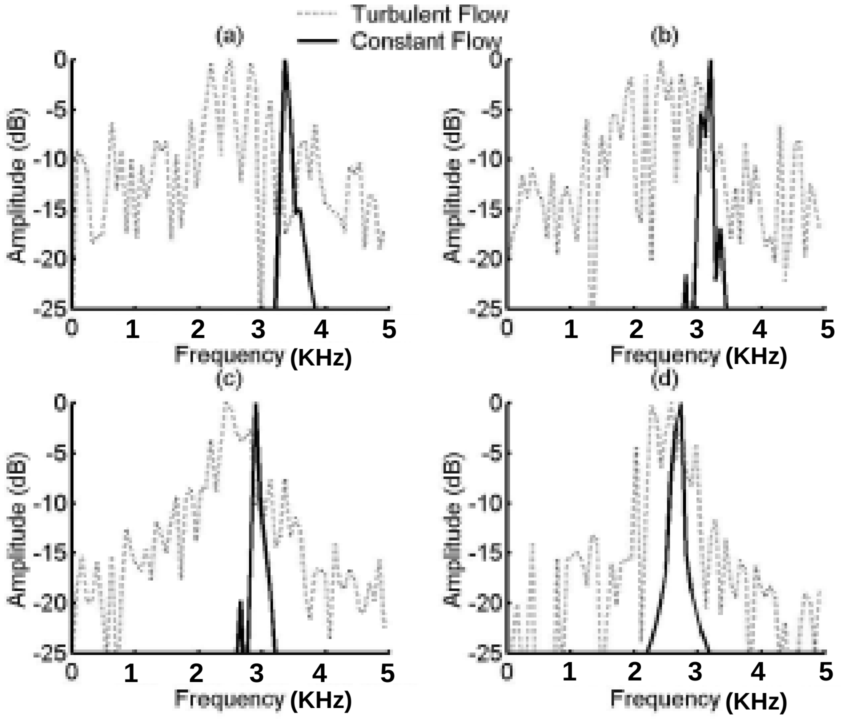

Figure 2.12 The Doppler spectra of laminar flow with constant velocity (solid) and flow with turbulence (dotted). The Doppler angles are (a) 30^0, (b) 45^0, (c) 60^0, and (d) 75^0.

The simulation model and relative parameters were the same as that described previously. 64 Doppler signals were simulated for each case. The laminar flows with constant velocities were introduced to compare with flows with turbulence. The maximum velocity was 30 cm/s. Figures 2.12(a)-(d) represent the distributions of Doppler spectrum using FFT with Doppler angles of 30^o, 45^o, 60^o, and 75^o, respectively. The solid and dotted lines represent the results of laminar flows with constant velocities and turbulent flows, respectively. The results show that the Doppler bandwidth of a turbulent flow is broader than that of a laminar flow with constant velocity.

The Doppler angle estimates in turbulent flows with five Doppler data sets at each angle are shown in figure 2.13. Figure 2.13(a) shows the estimated Doppler angles using the AR method, which had an average estimation error of 17.3^o. The FFT method using 64 flow samples had an average error of 15.7^o as shown in figure 2.13(b). The results show that both the AR and the FFT methods are not suitable to estimate Doppler angles when the Doppler spectrum is affected by turbulence.

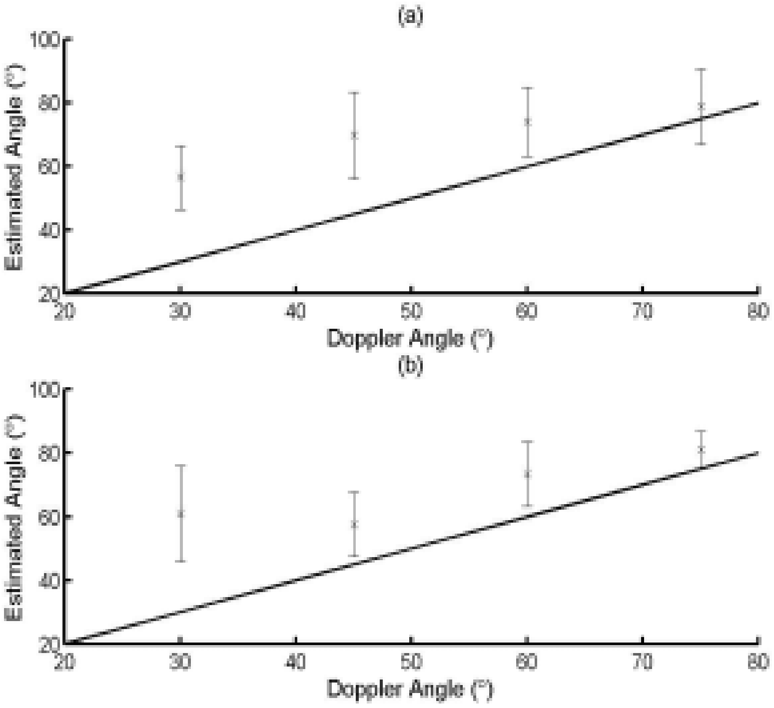

Figure 2.13 Doppler angles estimated for simulated data of turbulent flows using (a) the AR method and (b) the FFT method. The solid lines are the true angles. The error bars represent ± one standard deviation relative to the mean value (“×”).

2.4 *In Vitro* Experiments and Results

2.4.1 Velocity with Spatial Changes

Phantom experiments were performed using the experimental system shown in figure 2.14 to investigate the performance of the AR method. The data acquisition system consisted of a pulser/receiver (Panametrics 5072PR, Massachusetts, USA), and a VXI mainframe computer (Hewlett-Packard E1401B, California, USA) with a 12-bit, 40 Msamples/s arbitrary function generator and a 12-bit, 20 Msamples/s A/D converter. The equipment was controlled by a personal computer via VEE software (Hewlett-Packard, California, USA). The arbitrary function generator was used to externally trigger the pulser at a pulse repetition interval of 200 μs. The returning echoes were amplified, sampled by the A/D converter, and stored for off-line signal processing. Data analysis and graphic display were performed on a PC using MATLAB (MathWorks, Massachusetts, USA).

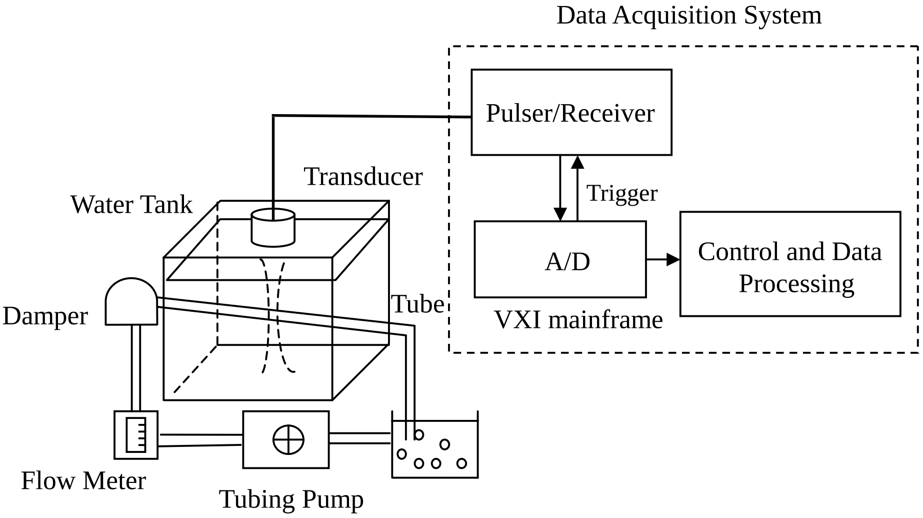

Figure 2.14 A block diagram of the experimental system setup.

The circular array transducer (Panametrics V308-SU, Massachusetts, USA) had a center frequency of 5 MHz and a fixed focus at 70 mm. The transducer diameter was 19 mm, which gave a two-way –6 dB beam width at the focal point of approximately 1 mm. Blood-mimicking fluid (Shelley Medical Image Technologies, Ontario, Canada) was used (Ramnarine et al, 1998). The flow system comprised a tubing pump (Cole-Parmer Model 77201-60, Illinois, USA), peroxide-cured silicone tubing (Cole-Parmer L/S-18, Illinois, USA), a shielded flow meter (Gilmont

Instruments GF-2560, Illinois, USA), and a pulse damper (Cole-Parmer LC-07596-20, Illinois, USA) that eliminated pulsation in the output flow.

The Doppler angles investigated in this study were 33°, 45°, 54°, 60°, and 72°, with five Doppler data sets being used at each angle. One valid Doppler signal that satisfied the criteria described in section (2.2.2) was used for each data set. The results are shown in figure 2.15. Figure 2.15(a) shows the estimated Doppler angles using the AR method, which had an average estimation error of 3.6° and a standard deviation ranging from 4.6° to 7.6°. The FFT method shown in figure 2.15(b) using 64 flow samples had an average error of 4.7° and a standard deviation ranging from 3.0° to 5.2°. The actual standard deviation and the mean values from the Doppler angle estimation are listed in table 2.2. The experimental results indicate that no significant differences in Doppler angle estimation were found between the AR and FFT methods for these Doppler angles. Table 2.2 shows that the standard deviations on the estimates from the AR method are always higher than those from the FFT method, with this difference reaching a factor of 2 for high angles. A possible reason for this is the extrapolation error inherent in the AR method.

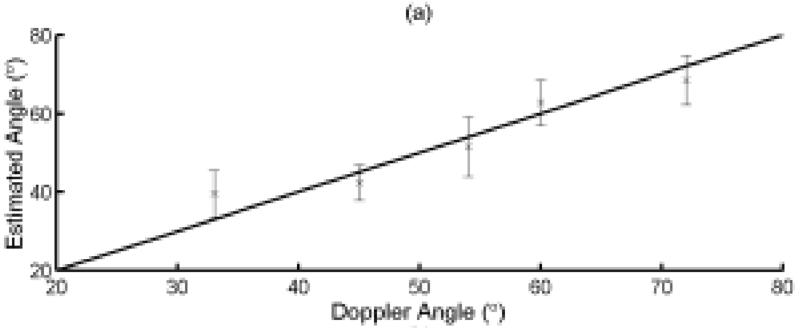

(b)

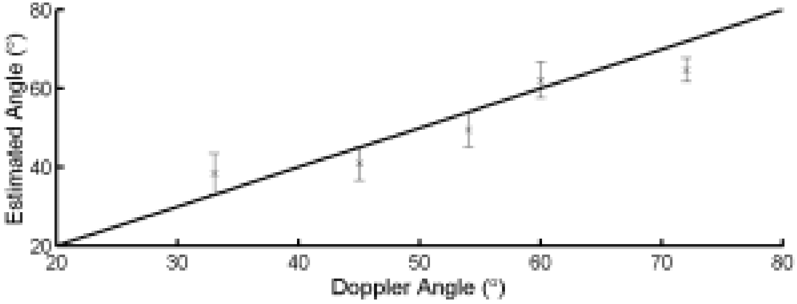

Figure 2.15 Doppler angles estimated for experimented data using (a) the AR method and (b) the FFT method. The solid lines are the correct angle estimates. The error bars represent ± one standard deviation relative to the mean value ("×").

Table 2.2 The Doppler angle estimates obtained using the AR method and the FFT method on experimental data (mean ± one standard deviation).

Doppler Angle (^{o})	AR Method (^{o})	FFT Method (^{o})
33	39.6 ± 6.0	38.4 ± 5.2
45	42.3 ± 4.6	41.0 ± 4.3
54	51.6 ± 7.6	49.6 ± 4.4
60	62.8 ± 5.7	62.2 ± 4.5
72	68.6 ± 6.4	64.7 ± 3.0

2.4.2 Velocity with Temporal and Spatial Changes

Experiments were also conducted to investigate performance of the AR method. A block diagram of the experimental system is shown in figure 2.16. The pulsatile flow was generated by the CompuFlow1000 flow system (Shelley Medical Imaging Technologies, Ontario, Canada). A blood mimicking fluid (Shelley Medical Imaging Technologies, Ontario, Canada) was used as the scattering source. The heart cycle was 0.752 s. A silicone tube with an 8 mm internal diameter was used as the vessel.

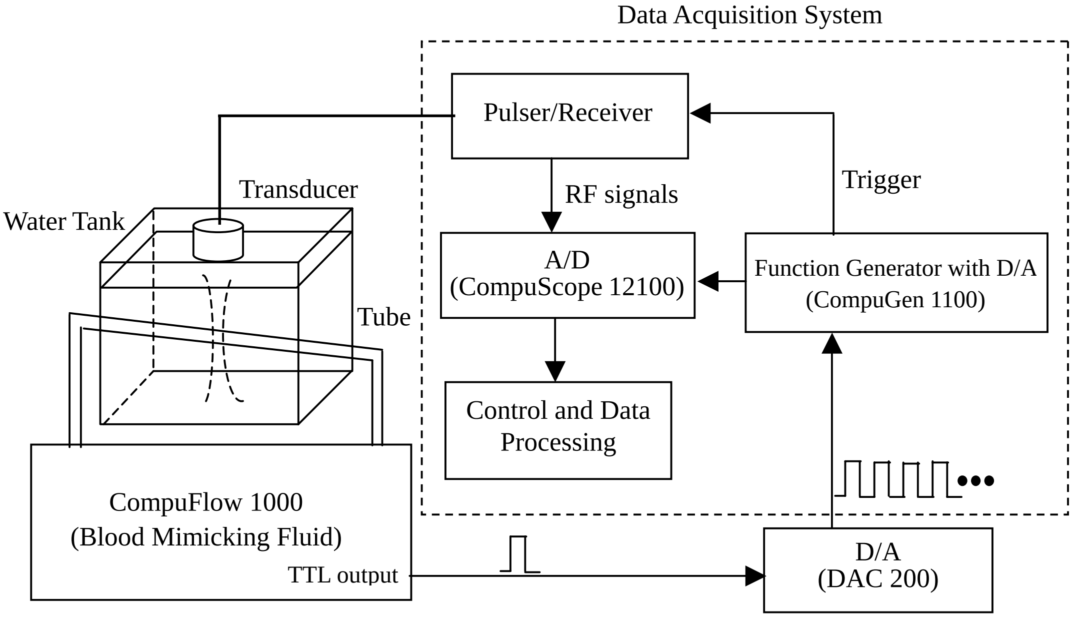

Figure 2.16 Pulsation flow experimental system set up.

The data acquisition system consisted of a pulser/receiver (Panametrics 5072, MA, USA) with a 12-bit, 80 Msamples/s arbitrary function generator (CompuGen

1100, Gage, Montreal, Canada) and a 12-bit, 100 Msamples/s A/D converter (CompuScope 12100, Montreal, Canada). The sampling frequency of the A/D converter was 20 Msamples/s. The arbitrary function generator was used to externally trigger the pulser with a PRI of 150 μs. The equipment was controlled by a personal computer under LabVIEW (National Instruments, TX, USA). After the returning echoes were amplified, the signals were then sampled by the A/D converter and stored for off-line signal processing. Data analysis and graphic display were done on a personal computer using MATLAB (MathWorks Inc., MA, USA). The transducer (Panametrics V381, MA, USA) had a center frequency of 3.5 MHz and a fixed focus at 70 mm. Diameter of the transducer was 19 mm making the two-way –6 dB beam width about 1.4 mm at the focal point. In this study, two D/A converters were used in order to ensure that the CompuFlow1000 flow system and the data acquisition system were synchronized.

In the experiments, four arterial flows with peak velocities at 10, 30, 50, and 70 cm/s were used. The four flows corresponded to mean velocities (i.e., temporal averages) at 3, 9, 15, and 21 cm/s, respectively. The velocity profile with the peak velocity at 10 cm/s (defined by the CompuFlow 1000 flow system) is shown in Figure 17(a). The Doppler angle was 45^0. Note that the Doppler signal from 0 to 0.285 s (denoted by the dashed line in figure 2.17(a)) in the arterial flow was collected. The portion of the Doppler signal also included the peak velocity, where the velocity variation was the greatest. Figure 2.17(b) shows the corresponding grayscale M-mode image of the Doppler signal collected by the experimental system with a dynamic range of 40 dB. The two horizontal dashed white lines represent the upper and the bottom vessel walls, respectively.

The Doppler angles used in the experiments were 30^o, 45^o, 55^o, 65^o, and 78^o. At each angle, five data sets were used. For each data set, Doppler angles were estimated every 0.05 s. In addition, the data selection criteria described in Section (2.2.2) were applied. In other words, one of the flow samples must contain the maximum in the axial direction and signal intensity of the Doppler signal increases and reaches a peak before it starts to decrease along the Doppler temporal direction.

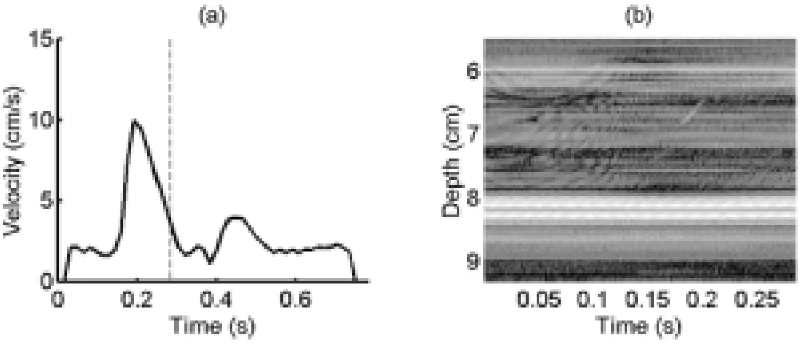

Figure 2.17 Experimental data for a pulsatile flow with the peak velocity at 10 cm/s. (a) Velocity profile of the arterial flow. (b) M-mode image.

Results of the Doppler angle at 45^0 using the AR method and the FFT method are shown in figures 2.19 and 2.20, respectively. Panels (a)-(d) represent the flows with peak velocities of 10, 30, 50, and 70 cm/s, respectively. The dashed lines in all panels are the true Doppler angle. In figure 2.18, the AR method had an average estimation error of 3.75^o (average estimate denoted by "x") and the standard deviation ranged from 3.71^o to 4.31^o (denoted by the error bar). The results from the FFT method using 64 original flow samples as shown in figure 2.19 had an average error of 6.87^o and the standard deviation ranged from 6.03^o to 8.00^o.

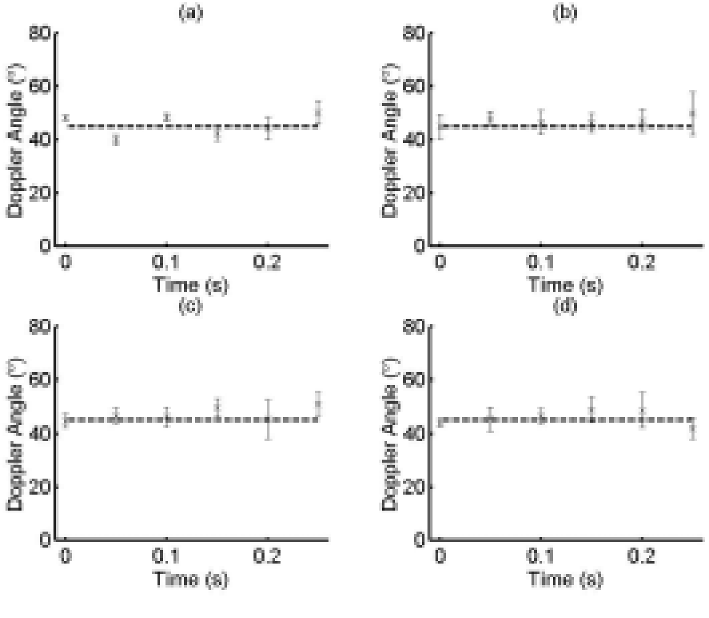

Figure 2.18 Estimated Doppler angles using the AR method. The real angle is 45^0. Peak velocities are (a) 10 cm/s, (b) 30 cm/s, (c) 50 cm/s, and (d) 70 cm/s.

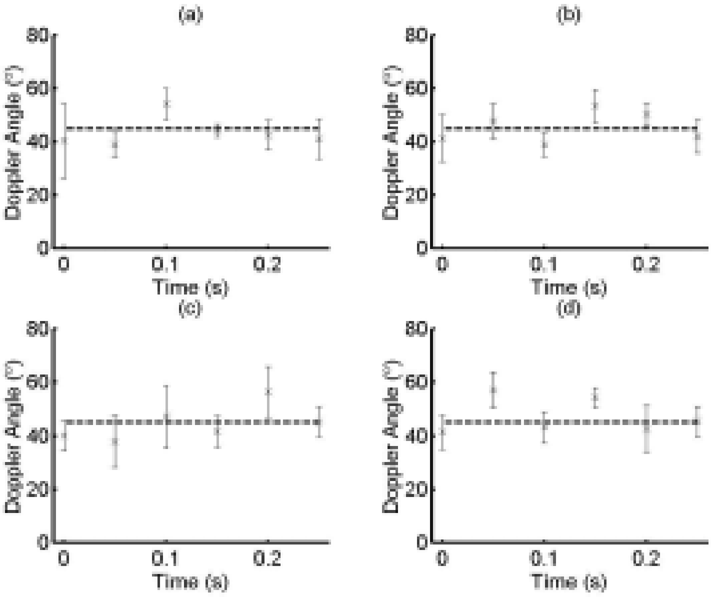

Figure 2.19 Estimated Doppler angles using the FFT method. The real angle is 45^0. Peak velocities are (a) 10 cm/s, (b) 30 cm/s, (c) 50 cm/s, and (d) 70 cm/s. Error bars represent ± 1 standard deviation relative to the mean value.

The mean values and standard deviations of Doppler angle estimation with different Doppler angles (from 30^o to 78^o) and flow rates were summarized in table 2.3. Other ultrasonic parameters were the same as those used in previous experiments. Tables 2.3 (a) and (b) show the Doppler angle estimates using the AR method and the FFT method, respectively. The experimental data for the AR method had an average estimation error of 3.50^o and an average error of 7.08^o for the FFT method. The experimental results also indicate that AR method outperformed the FFT method.

The relative performance of the AR and FFT method depends on the signal-to-noise ratio (SNR). The SNR is defined as the ratio of the average signal power to the average noise power. Marasek and Nowicki (1994) compared the performance of various spectral estimation techniques for maximum frequency estimation of the Doppler spectra. It was concluded that the performance of the spectral estimation techniques depended on SNRs and accurate estimation results can be obtained only for signals with SNR > 3dB. In our study, the SNRs were equal to 20 dB and 10.5 dB (> 3dB) for the simulations and the experiments, respectively. Thus, the AR and the FFT method are both suitable to estimate the Doppler spectra.

Table 2.3 Summary of the errors of Doppler angle estimation using (a) the AR method and (b) the FFT method with experimental data. All results are mean ± one standard deviation.

(a)

Doppler angle (^{o})	**Peak velocity (cm/s)** 10	30	50	70
30	2.93 ± 3.33	3.05 ± 3.06	3.30 ± 2.74	3.77 ± 3.19
45	3.46 ± 3.71	3.95 ± 4.31	4.05 ± 4.04	3.53 ± 3.99
55	3.77 ± 3.54	3.43 ± 3.62	3.42 ± 3.69	3.99 ± 3.14
65	2.75 ± 3.45	3.51 ± 3.32	3.96 ± 3.38	4.65 ± 4.01
78	3.40 ± 3.38	2.54 ± 2.88	3.06 ± 3.13	4.13 ± 3.02

(b)

Doppler angle (^{o})	**Peak velocity (cm/s)** 10	30	50	70
30	8.87 ± 7.51	7.24 ± 5.96	8.62 ±5.02	6.46 ±7.19
45	6.45 ± 6.70	6.50 ± 6.03	7.33 ±8.00	7.20 ±6.19
55	6.98 ± 6.26	5.41 ± 6.57	6.58 ±7.02	8.34 ±7.41
65	5.51 ± 7.24	6.38 ± 5.56	8.02 ±6.25	7.95 ±6.87
78	6.94 ± 5.67	5.54 ± 6.52	7.54 ±5.18	7.81 ±6.13

2.5 Conclusions

This chapter proposes a new approach for Doppler angle estimation that requires a small number of flow samples. An eighth-order AR model was used to extrapolate the original eight flow samples to 64 flow samples for spectrum estimation. The selection criteria for both the Doppler signal and the model order had a significant effect on the results obtained. The results obtained using simulated and experimental data show that the AR method not only accurately estimated the Doppler bandwidth, it also outperformed the conventional FFT method at small Doppler angles. This study shows that real-time two-dimensional Doppler angle estimation is possible using only a small number of flow samples.

3. Chapter 3 Contrast-Specific Flow Estimation[2]

3.1 Introduction

Ultrasound contrast agents are used to enhance the acoustic backscattered intensity of blood. They improve blood flow detection and offer possibilities to visualize perfusion conditions. Several recent studies have focused on *in vivo* and *in vitro* flow measurements based on the indicator-dilution theory (Chen et al 1998; Claassen et al 2001; Goldberg 1997; Heidenreich et al 1993; Li et al 2001; Schwarz et al 1993). In this chapter, the relevant topics of contrast-specific flow estimation based on the indicator-dilution theory are discussed.

The indicator-dilution theory provides a mathematical model for estimating hemodynamic parameters using changes in the backscattered intensity as a function of time (i.e., the time-intensity curve, TIC) (Ostrander et al 1990; Schwarz et al 1993; Ugolini et al 2000; Wilkening et al 1999, 2000). It has been shown that relative change in the wash-out rate of the time-intensity curve is linearly proportional to the volume flow rate (Schwarz et al 1993). It has also been shown that the peak intensity of the time-intensity curve is approximately linearly proportional to the volume concentration of the injection contrast agent (Wilson et al 1993). Thus, the possibility for quantitative perfusion analysis using the time-intensity curve has been demonstrated.

3.1.1 Wash-Out Time-Intensity Curve

The concentration of the contrast agent as a function of time can be mathematically derived by modeling the flow system as a series of blood mixing chambers. Each mixing chamber is described by a transfer function relating the indicator concentration entering (i.e., input) and leaving (i.e., output) the chamber as a function of time. With a bolus injection, a good correlation between time constants derived from the time-intensity curve and the volume flow rate can generally be found, if the acoustic intensity is linearly proportional to the concentration (Li et al 2001).

---

[2] This Chapter is based on the work presented at *Ultrasonic Imaging*, 2002 and *Ultrasound in Medicine and Biology*, 2003.

However, the time-intensity based methods are not as effective when the injection site is far away from the measurement site (Wilson et al 1993). The situation can be viewed as the case where there are more than one mixing chamber between the injection site and the measurement site. Thus, the input function of the last mixing chamber has a prolonged duration. When a prolonged injection is introduced, the output time-intensity curve reflects not only the dilution process in the mixing chamber, the input must also be taken into account.

3.1.2 Linear Time-Invariant System

To take into account the input function, the output time-intensity curve of the mixing chamber can be represented as the convolution of the input function and the transfer function of the mixing chamber (Axel 1980; Bates 1991; Gobbel and Fike 1994; Mor-Avi et al 1993). Assuming a linear and time-invariant (LTI) system, the transfer function of the mixing chamber can be obtained by deconvolution techniques if both the input and the output time-intensity curves are available. However, most deconvolution algorithms proposed to date were applied to analyze simulation data. Efficacy of the deconvolution algorithms on *in vitro* and *in vivo* data is not yet evaluated.

A fundamental hypothesis that needs to be tested before investigating the deconvolution techniques is the assumption that the blood mixing chamber is LTI (Eigler et al 1989). In other words, it is necessary to verify if the acoustic backscattered intensity is linearly proportional to the concentration such that the measured time-intensity curve reasonably represents the temporal change of the concentration of the contrast agent. Influence of the concentration on flow estimation has been preciously discussed (Claassen et al 2001; Heidenreich et al 1993; Schwarz et al 1993; Wilson et al 1993). The linear relationship between the concentration and parameters such as the area under the time-intensity curve and the peak intensity was found if the concentration was within a certain range. One primary purpose of this section is to investigate not only the relationship between the acoustic intensity and the concentration, but also effects of the concentration on flow estimation results. In addition, both a compartment flow model and a perfusion flow model will be used.

Another factor affecting the LTI assumption is the effect of the chamber size on blood mixing. In other words, the effective volume may be different from the physical volume of the mixing chamber (Fred 1962). If the contrast agent does not mix completely with liquid within the mixing chamber, the effective dilution volume is smaller than the physical volume of the mixing chamber. Because the wash-out rate of the contrast agent depends on both the volume flow rate and the volume of the mixing chamber, quantitative flow estimation is not possible without the knowledge of the effective mixing volume. In other words, the indicator-dilution theory can only be used to estimate the effective volume, instead of the physical volume. Influence of the effective volume on the time-intensity based flow estimation is also studied in this paper.

Another purpose in section (3.4) is to investigate the validity of the LTI assumption by comparing the input time constant to the output time constant. The relationship between the input time constant and the output time constant are mathematically derived and compared to the measurement results. The experiments in this chapter were performed with both a compartment model and a perfusion model (Hindle and Perkins 1994). Each model had two configurations for bolus injections and prolonged injections, respectively.

3.1.3 Input-Output Time-Intensity Curve

If the blood mixing chamber can be treated as a linear time-invariant system, it may be possible to apply deconvolution techniques for flow estimation if the time–intensity relationships are measured at both the input and the output of the blood mixing chamber (Yeh et al 2001).

In section (3.5), an *in vitro* perfusion model is set up to measure three TICs – inflow, outflow, and the perfused area – simultaneously using grayscale imaging. One purpose of this section is to evaluate the effect of shadowing on TIC-based perfusion assessment. In the perfused area, shadowing is evaluated at different regions of interest (ROIs) during different flow rates. The correlation between flow parameters and the various TICs is also discussed. Moreover, a new technique is proposed in this study for perfusion estimation based on both the inflow and the outflow TICs, and is referred to as the input–output TIC (IOTIC) method. The TIC based on the IOTIC method is compared with the TIC measured within the perfused area. The relationships between flow parameters and parameters of the IOTICs are also discussed. Note that the injection site can be far away from where the inflow TIC is measured, because both input and output time intensities are taken into account.

One potential clinical application of the IOTIC technique is to assess brain perfusion by measuring the time–intensity relationship in the extracranial flow. Specifically, the time–intensity curves are measured both in a carotid artery and a jugular vein. Therefore, the shadowing effect and the poor acoustic window can be avoided since the TIC from the brain tissue is no longer needed.

3.2 Basic Principles of Indicator-Dilution Theory

3.2.1 Time-Intensity Curve (TIC)

When a certain amount of indicator solution is input into the flow system, the concentration at the system output can be described based on the indicator-dilution theory. However, concentration of the ultrasound contrast agent is not directly measured in practice. Instead, the backscattered acoustic intensity is used to represent the concentration of contrast agent. The following discussion on the mixing chamber model assumes that the backscattered intensity is a linear function of the concentration of the contrast agent. Validity of this assumption will be studied in the next section.

3.2.1.1 Mixing Chamber Model

A diagram of the mixing chamber is depicted in figure 3.1. The echo intensity measured at the output of a mixing chamber, denoted by $I_o(t)$, depends on the input function $I_I(t)$ and the transfer function $h(t)$. If the system is LTI, the output function can be expressed as the convolution of the input function and the transfer function of the mixing chamber (Chen et al 1998). In other words,

$$I_O(t) = I_I(t) \otimes h(t), \tag{3.1}$$

where $\otimes$ stands for convolution and $h(t)$ is the transfer function of the mixing chamber.

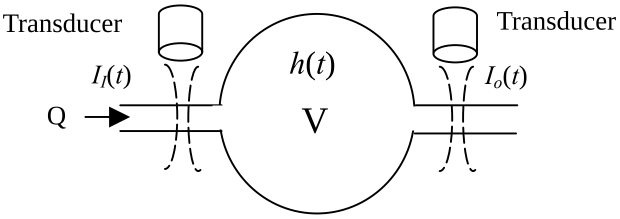

Figure 3.1 Illustration of the input and the output of a mixing chamber.

3.2.1.2 Transfer Function

The transfer function $h(t)$ contains characteristics of the mixing chamber and is given by

$$h(t) = \begin{cases} 0 & t < 0 \\ \frac{1}{\tau} e^{-t/\tau} & t > 0 \end{cases}, \tag{3.2}$$

where τ is considered as the system's transit time (i.e., inverse of the wash-out rate) and it is proportional to the mixing chamber volume and inversely proportional to the volume flow rate (Chen et al 1998). Equation (3.1) indicates that deconvolution techniques can be applied to estimate the transfer function of a mixing chamber if both the input and the output time-intensity curves are available. After the transfer function is determined, blood flow parameters, such as the wash-out rate, can then be obtained.

3.2.2 Relevant Flow Parameters Estimates

The time-intensity curve is used to derive two parameters. One is the mean transit time (MTT) and the other is the area under curve (AUC).

3.2.2.1 Mean Transit Time (MTT)

The MTT is defined as

$$MTT = \frac{\int_0^\infty tx(t)\,dt}{\int_0^\infty x(t)\,dt}, \tag{3.3}$$

where $x(t)$ is either the measured time-intensity curve or the derived transfer function of the mixing chamber. The MTT represents the time for the entire fluid volume to pass though the mixing chamber. According to the indicator-dilution theory, there is an inverse relation between the flow rate and the MTT. If the transfer function is defined in equation (3.2), it can be shown that

$$MTT = \tau = \frac{V}{Q}, \tag{3.4}$$

where V is the volume of mixing chamber and Q is the volume flow rate.

Base on equations (3.1) and (3.2), it can also be shown that the MTT of the output function (MTT_{out}) equals the sum of the MTT of the input function (MTT_{in}) and the MTT of the transfer function of mixing chamber (MTT_{mix}) (Bates 1991). In other words,

$$MTT_{out} = MTT_{in} + MTT_{mix}. \tag{3.5}$$

To verify the LTI assumption, the MTT derived from equation (3.5) will be compared with the value derived from equation (3.4).

3.2.2.2 Area Under Curve (AUC)

Finally, the AUC defined as the following equation is used to test the linear relationship between the concentration and the backscattered intensity (Claassen et al 2001).

$$AUC = \int_0^\infty I_o(t)dt \tag{3.6}$$

3.3 Self-Made and Commercial Contrast Agents

Here, we introduced three different kinds of contrast agent to do the experiments. A commercial contrast agent (Levovist®, Schering, Berlin, Germany) referred to section (1.3.2) and two self-made contrast agents were used.

The first one of self-made agent was made from human albumin using the agitation technique (Li et al 2001; Navin and Reinhard 1993). The size of the self-made microbubbles was estimated using a light microscope (EMZ-TR, MEIJI Tech. Co., Tokyo, Japan). The diameter of the self-made agent was about 20 to 50 μm (Li et al 2001). The concentration of the albumin-based contrast agent is primarily determined by the amount of air used when making the agent. In this chapter, the contrast agent is referred to Self-Made Agent-A.

The second contrast agent used in this chapter was sonicated albumin. The procedure used to produce the agent was similar to that described by Bos et al. (1996). To heat the solution, 8 ml of 25% human albumin (Octapharma, Vienna, Austria) was sonicated by a sonicator at a low-amplitude setting of 40% (model 450, Branson Ultrasonics Corporation, Danbury, CT). After 60 s, the acoustic amplitude was increased to 60% to sonicate the albumin for another 60 s. Stable microbubbles were formed by surface agitation. The sonicator was switched off and another 8 ml of albumin was administered at room temperature. The solution was stirred carefully and 3 ml of contrast agent was withdrawn from beneath the foamy surface. The diameter of the microbubbles was measured under a light microscope (model EMZ-TR, Meiji, Tokyo, Japan), and ranged from 5 to 20 μm. This contrast agent is referred to Self-Made Agent-B. Figure 3.2 shows an image of the albumin-based contrast agent (Self-Made Agent-B). Note that the bubbles may appear artificially large in the image because they were flattened when taking the picture.

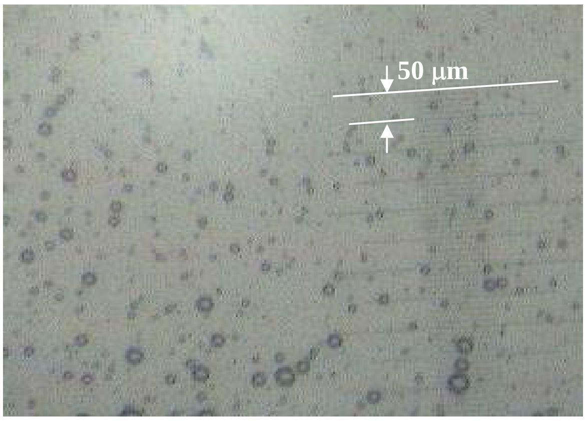

Figure 3.2 Photograph of the sonicated albumin-based contrast agent.

3.4 Linear Time-Invariant Verification of Mixing Chamber Model

3.4.1 Concentration vs. Mean Transit Time

3.4.1.1 Experimental Setup

Two *in vitro* flow models were constructed. One was made of a spherical compartment phantom and the other was made of a perfusion phantom (Hindle and Perkins 1994). Furthermore, each flow model had two different configurations. One was for bolus injection and the other was for prolonged injections. Figure 3.3 shows a single compartment phantom and figure 3.4 shows two compartment phantoms in cascade. If the input has a short duration compared to the MTT of the mixing chamber, the output intensity curve measured from the phantom shown in figure 3.3 approximates the transfer function of the mixing chamber (i.e., the input is approximated as an impulse). For the flow model shown in figure 3.4, on the other hand, the input of chamber A is also the output of chamber B. Thus, the time-intensity curve measured at the output of chamber A can be used to evaluate the time-intensity based method when the input has a prolonged duration.

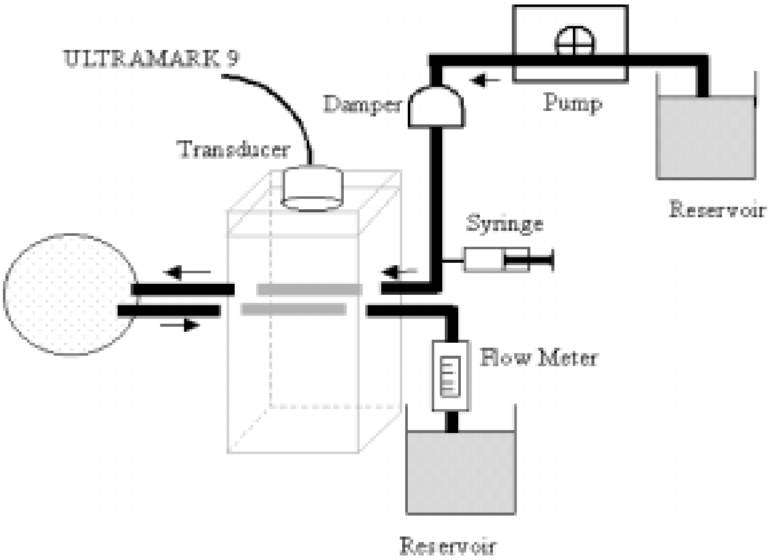

Figure 3.3 Experimental setup for the compartment phantom.

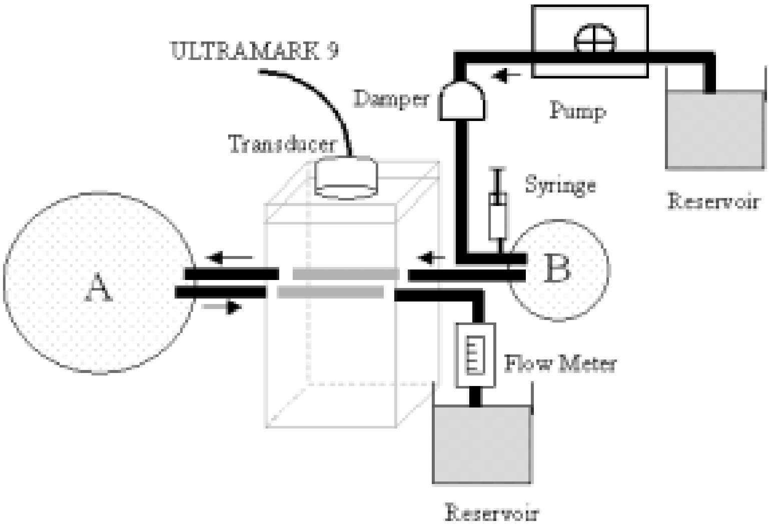

Figure 3.4 Experimental setup for two compartment phantoms in cascade.

The compartment phantom was made of an acrylic hollow sphere. Two silicon tubes connecting to the sphere were fixed in parallel with opposite flow directions and immersed in a water tank. The diameter of the tubes was 8 mm. A 7-MHz linear array transducer (L7-4, Advanced Technology Laboratories, Bothell, WA, U.S.A.) was placed 2 cm above the tubes. The damper was used to stabilize the flow. To prevent re-circulation of the contrast agent back in the phantom, the water in this system only passed through the model once. In figure 3.3, the contrast agent was injected to the tube at the front side of the sphere by a syringe. In figure 3.4, the injection position was at the input side of chamber B. The input time-intensity curve of chamber A was the transfer function of chamber B if duration of the input injection was sufficiently short.

The other flow model was based on a perfusion phantom made of a dialysis cartridge. Again, an additional sphere was inserted between the injection site and the perfusion phantom as the configuration for prolonged injections. Schematic diagrams of the two configurations are shown in figures 3.5 and 3.6, respectively. The dialysis tube (C-12, TERUMO Co., Tokyo, Japan) consisted of 8600 capillaries with a diameter of 200 μm and a length of 235 mm for each capillary, making a total volume of 79 ml.

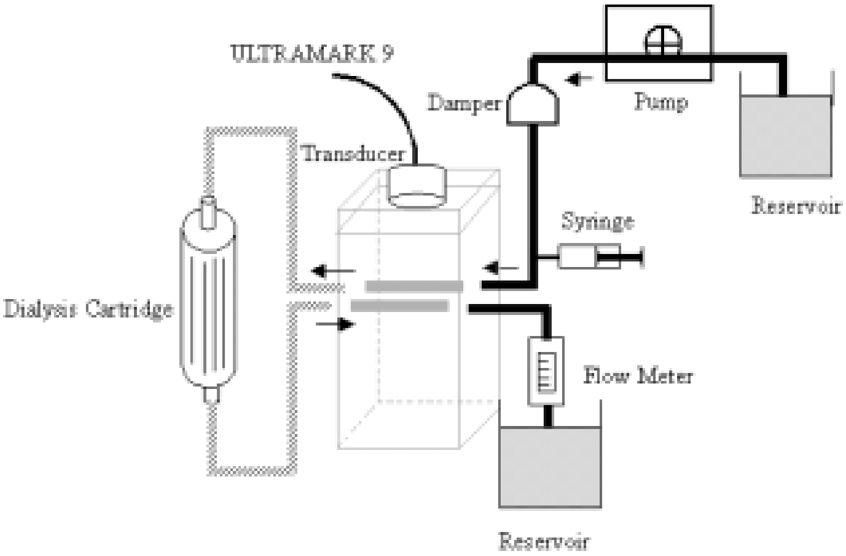

Figure 3.5 Experimental setup for the perfusion phantom.

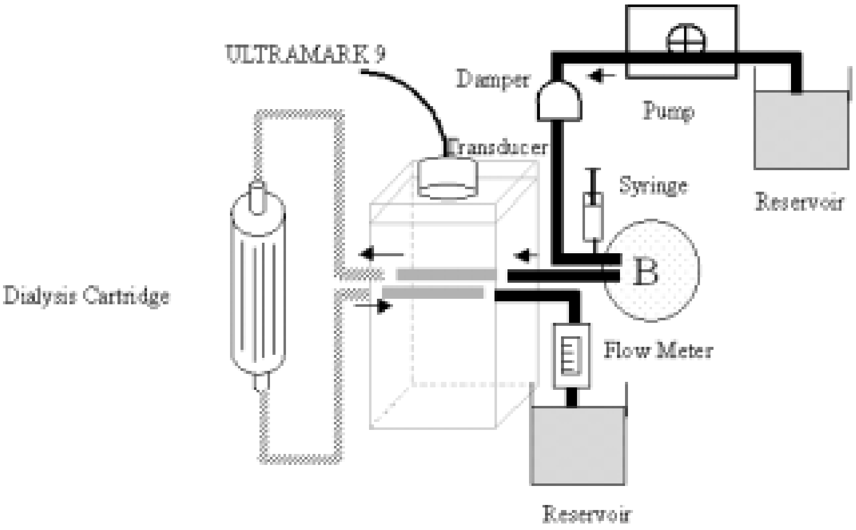

Figure 3.6 Experimental setup for the perfusion phantom in cascade with a compartment phantom.

3.4.1.2 Imaging Processing

The input and the output time-intensity curves were simultaneously measured using a commercial ultrasound machine (Ultramark 9, Advanced Technology Laboratories Inc., Bothell, WA, U.S.A.). The mechanical index (MI) was 0.7 with the imaging frame rate ranging from 20 to 30 Hz. The destruction of microbubbles due to the acoustic power level was negligible based on the fact that the ratio of the input AUC to the output AUC was close to unity in all cases. Effects of post-processing on the time intensities were also ignored because the images were acquired prior to the post-processing functions were applied. In addition, the shadowing and other unwanted effects potentially resulted from the uneven microbubble distribution were not observed in the gray-scale images. Gray-scale images of the transverse view of the input and the output tubes were acquired one frame per second. A total of 300 image frames (i.e., 5 minutes) were acquired and digitized by a frame grabber (UPG401B, UPMOST Corp., Taipei, R.O.C.) and stored for off-line analysis. The image size was 153 by 232 pixels covering a 36 mm by 55 mm area. A typical image is shown in figure 3.7. The two regions of interest denoted by the two circles correspond to the input and the output tubes. The image data were converted from the logarithmic scale to the linear scale before the mean backscattered intensities inside the ROI were calculated.

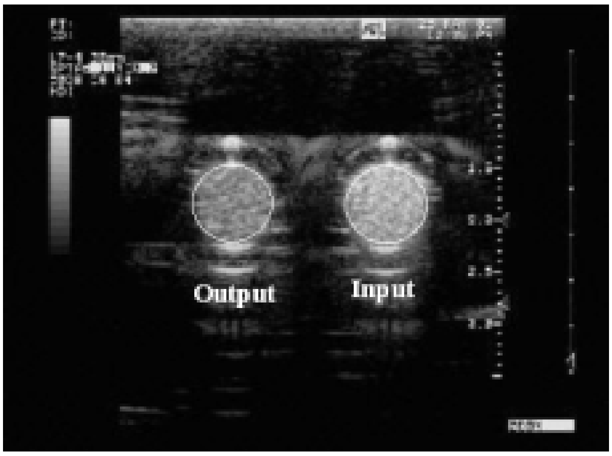

Figure 3.7 A typical gray-scale image showing intensities from both the input and the output tubes.

To obtain a time-intensity curve, a circle was used to cover the inner portion of the tube. Intensities of the pixels inside the ROI were summed and the result was used as the intensity at that particular time. The procedures continued until all the 300 digitized gray-scale images were processed.

To reduce noise in the time-intensity measurements, the time-intensity curve is fitted to a gamma function $g(t)$ defined as the following

$$g(t) = \alpha (t - t_o)^{\gamma} e^{-\beta (t - t_o)}, \tag{3.7}$$

where t_0 indicates a delay time, α and β are scaling factors and γ represents the skewness. All flow related parameters were calculated after gamma function fitting. A typical input and a typical output time-intensity curves are shown in figure 3.8. Note that the dotted lines correspond to the original measurements and the solid lines are with curve fitting.

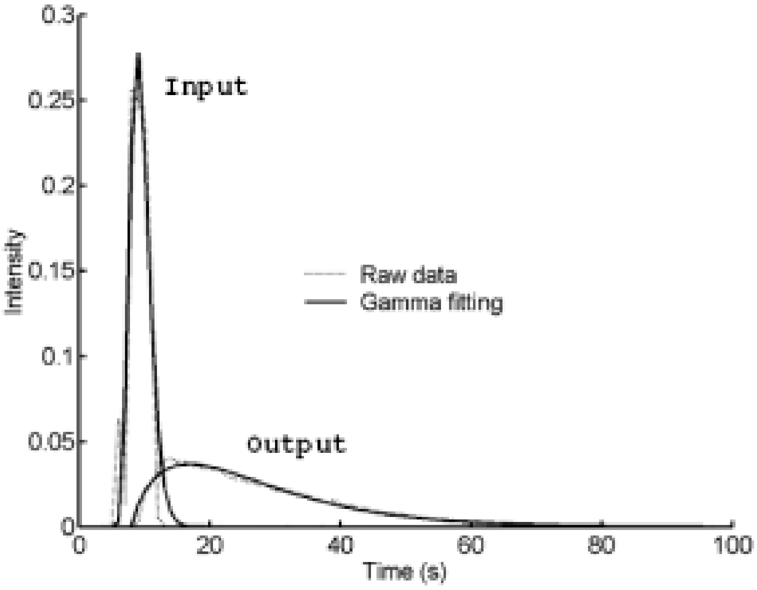

Figure 3.8 Typical input and output time-intensity curves with (solid) and without (dotted) gamma fitting.

3.4.1.3 Results: Compartment Phantom

Experiments were conducted to evaluate influence of the concentration of the contrast agent on the MTT estimates. A flow rate of 900 ml/min was used. For each case, the average and the standard deviation were taken from three independent measurements. The experimental setup is shown in figure 3.3 with the volume of the compartment at 200 ml.

Figure 3.9(a) demonstrates the relationship between the AUC and the concentration of Levovist®. The average values are shown with the error bars representing +/- one standard deviation. Levovist® with four different doses (0.5 g, 1.0 g, 1.5 g and 2.0 g) were mixed with 4 ml water. It is shown that the AUC increased with the Levovist® dose. Figure 3.9(b) shows the MTT estimated at four concentration levels (i.e., four different doses). Theoretical values derived from equation (3.4) were shown as the dashed line. Results indicate that although the AUC increased with the Levovist® concentration, the MTT estimates still varied with the concentration.

The same experiments were also performed with the perfusion phantom shown in figure 3.5 under the same experimental conditions. Results are shown in figure 3.10. Again, the AUC increased with the Levovist® concentration, but the MTT estimates were all smaller than the theoretical value (dashed line). Note that the theoretical value was calculated based on the sum of the volume of the cartridge (79 ml) and the volume of the connecting tubes (160 ml). If only the volume of the cartridge was considered, the dashed line becomes much closer to the measurement results.

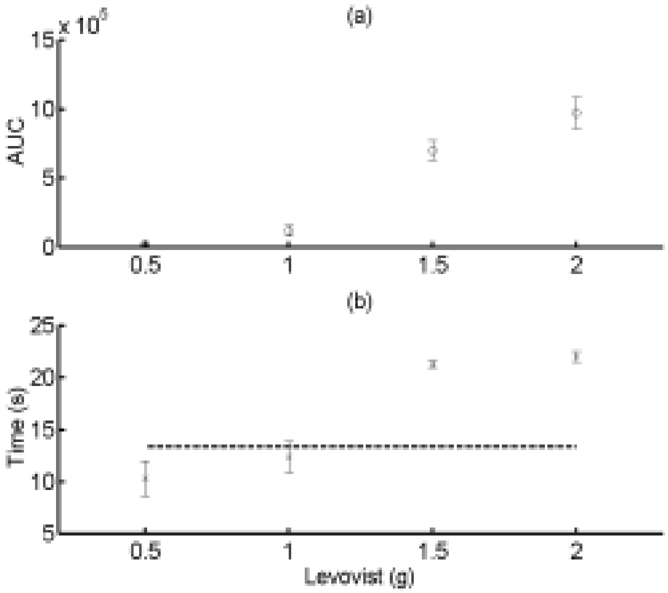

Figure 3.9 (a) AUC of the input time-intensity curve and (b) MTT of the output time-intensity curve vs. Levovist® concentration for the compartment phantom.

Note that the MTT's for the perfusion phantom (figure 3.10(b)) appear to be much flatter than those for the compartment phantom (figure 3.9(b)). One possible reason is the difference in the mixing camber volume. In the perfusion phantom, the real dilution volume equaled the volume of the cartridge. The dilution volume of the compartment phantom, on the other hand, was larger than that of the perfusion phantom. In other words, the physical volume may be larger than the effective volume.

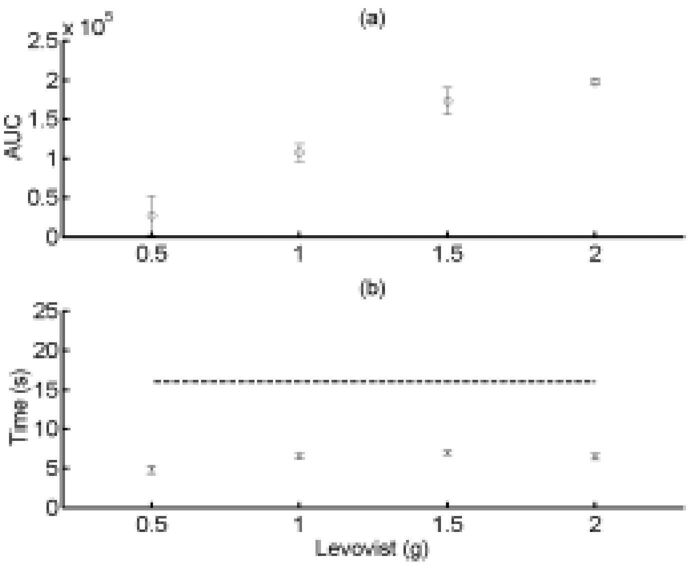

Figure 3.10 (a) AUC of the input time-intensity curve and (b) MTT of the output time-intensity curve vs. Levovist® concentration for the perfusion phantom.

3.4.1.4 Results: Perfusion Phantom

The experiments were also repeated using the albumin-based Self-Made Agent-A. Four ml of water and 0.2 ml of 20% human albumin were used in all cases. The different concentration levels corresponded to 0.2, 0.4, 0.6 and 0.8 ml of air, respectively. Figures 3.11 and 12 show the results from the compartment phantom and the perfusion phantom, respectively. In figures 3.11(a) and 3.12(a), the AUC increases with the amount of air. The amount of air primarily determines the concentration of the contrast agent. Figures 3.11(b) and 3.12(b) illustrate the MTT's estimated at different concentrations levels. Again, the MTT increased with the concentration for the compartment phantom and stayed relatively constant for the perfusion phantom.

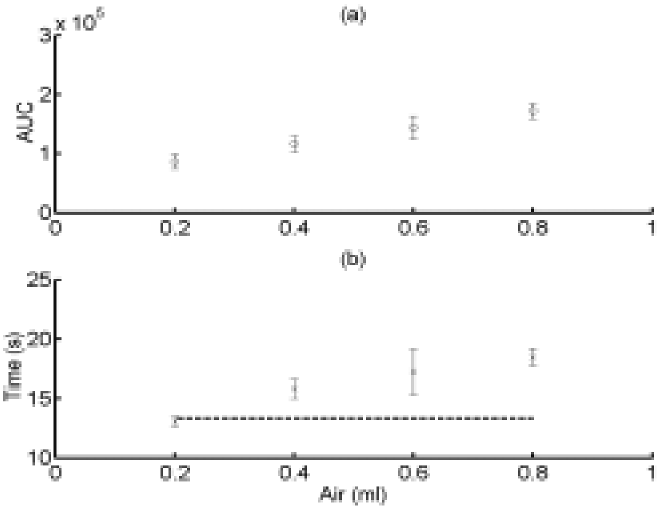

Figure 3.11 (a) AUC of the input time-intensity curve and (b) MTT of the output time-intensity curve vs. concentration of the albumin-based contrast agent for the compartment phantom.

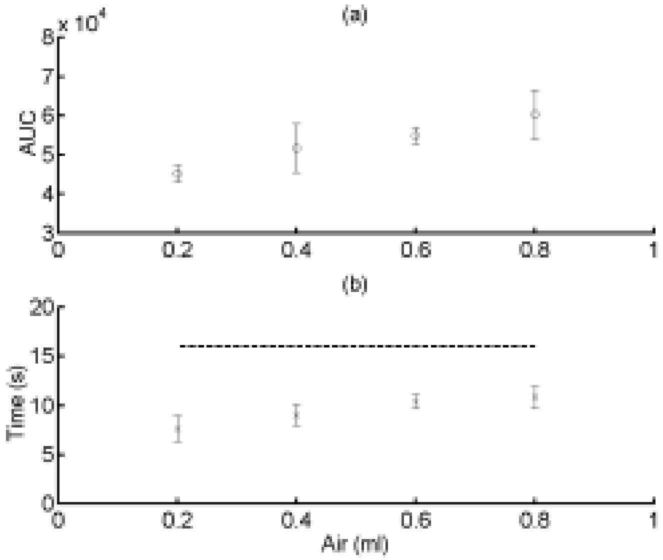

Figure 3.12 (a) AUC of the input time-intensity curve and (b) MTT of the output time-intensity curve vs. concentration of the albumin-based contrast agent for the perfusion phantom.

Results shown in figures 3.9-3.12 indicate that the MTT generally depends on the concentration, although the measurements agree well with the theory in certain situations. In addition, the MTT estimates from the self-made agent have larger standard deviations than those from the commercial agent Levovist®. One possible reason is the size uniformity of microbubbles. For Levovist®, 99% of the microbubbles are smaller 4 μm whereas size of the self-made agent ranged from 20 to 50 μm. The size uniformity may potentially affect the backscattered signal intensities.

3.4.2 Effective Mixing Volume

The MTT's were estimated from the output time-intensity curves using the compartment phantoms with different sizes and flow rates. The experimental setup is shown in figure 3.3 and the albumin-based Self-Made Agent-A was used. Results are shown in figure 3.13. In figure 3.13(a), the MTT's obtained at different concentration levels were shown. Again, the four concentration levels corresponded to 0.2, 0.4, 0.6 and 0.8 ml of air, respectively. Four ml of water, 0.2 ml of 20% human albumin were used in all cases. The volume of the compartment phantom was 200 ml. Flow rates were 500, 700, 900 and 1100 ml/min. For each flow rate, five independent measurements were performed. The horizontal axis represents the theoretical values obtained from equation (3.4) and the vertical axis shows the measured MTT. Mean values are shown as crosses with the error bars corresponding to +/- one standard deviation.

Linear regression was performed and the best-fit lines at different concentration levels are shown as the solid line (0.2 ml of air), the dashed line (0.4 ml of air), the dot-dashed line (0.6 ml of air) and the dotted line (0.8 ml of air). The four correlation coefficients between the MTT estimates and the linear regression lines were 0.94, 0.92, 0.94 and 0.93, respectively. In all cases, the estimated MTT is approximately inversely proportional to the volume flow rate Q, demonstrating that the indicator-dilution theory can be applied for relative volume flow measurements. However, absolute measurements are not possible due to the different MTT estimated at different concentration levels.

Results shown in figures 3.13 (b) to 3.13 (d) correspond to the estimated MTT's at different flow rates and different volumes of the compartment. As in figure 3.13(a), the flow rates were 500, 700, 900 and 1100 ml/min. The compartment volume was 260 ml for figure 3.13(b), 580 ml for figure 3.13(c), and 930 ml for figure 3.13(d). The concentration of the contrast agent was fixed at 4 ml of water, 0.2 ml of 20% human albumin and 0.2 ml of air. The three correlation coefficients between the estimated MTT's and the best-fit lines were 0.94, 0.92 and 0.88, respectively. The slopes of linear regression the best-fit lines for figures 3.13(b) to 3.13(d) were 0.66, 0.48 and 0.45, respectively. The high correlation coefficients showed that relative flow estimation is possible with the time-intensity based methods. Moreover, it is shown that the slope decreased as the chamber volume increased. In other words, the effective mixing volume changed with the physical volume. As the physical volume increased, the ratio of the effective volume to the physical volume decreased.

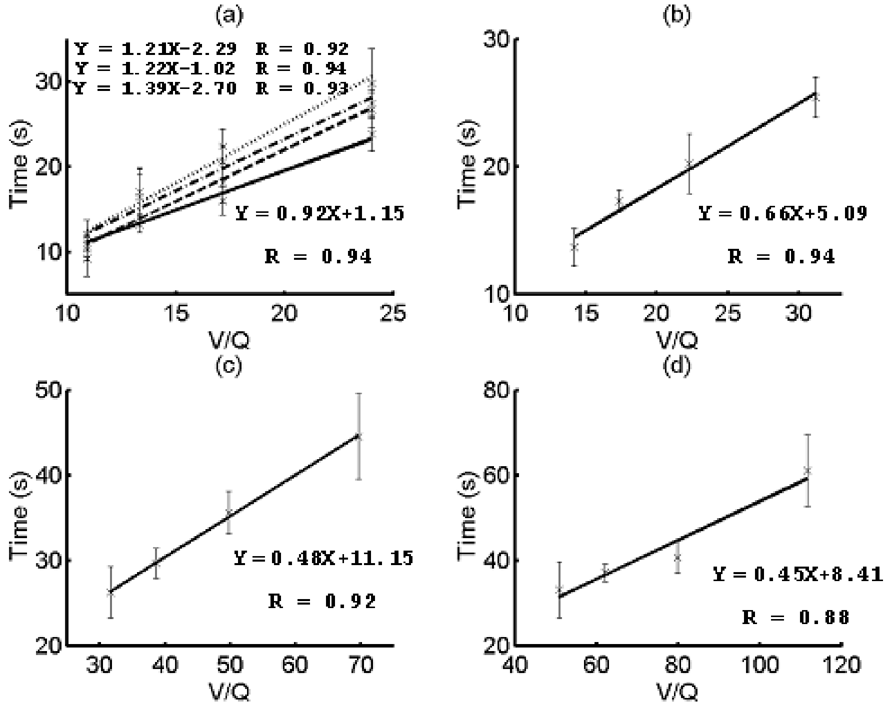

Figure 3.13 MTT measured with the mixing chamber volume at (a) 200 ml, (b) 260 ml, (c) 580 ml, and (d) 930 ml. The air used for making the contrast agent was 0.2 ml for all solid lines. In (a), 0.4 ml of air was used for the dashed lines, 0.6 ml for the dot-dashed line and 0.8 ml for the dotted line.

The results at the 0.2 ml of air concentration level were summarized in table 3.1. Tables 3.1(a) to 3.1(d) include results corresponding to the compartment volume of 200, 260, 580 and 930 ml, respectively. In each case, the average estimated MTT’s are shown in the second row. The theoretical values based on equation (3.4) and the ratios (ψ’s) of the estimated values to the theoretical values are shown in the third row and fourth row, respectively. If ψ is close to one, it indicates that the contrast agent mixes with the fluid completely within the chamber and the indicator-dilution theory can be applied for absolute analysis. Otherwise, only relative measures can be obtained. As shown in table 3.1, ψ is the closest to one with the smallest volume. It decreases as the compartment volume increases.

3.4.3 Prolonged Injection

The experimental setups shown in figures 3.4 and 3.6 were used to investigate effects of prolonged injection. For the setup shown in figure 3.4, the sizes of chambers A and B were 260 ml and 200 ml, respectively. Four flow rates at 500, 700, 900 and 1100 ml/min were used. At each flow rate, five independent measurements were performed to obtain mean and standard deviation. The Self-Made Agent-A composed of 0.2 ml of air, 4 ml of water and 0.2 ml of 20% human albumin was used.

Table 3.1 Summary of the estimated MTT's for four different volumes and four different flow rates. The volumes were (a) 200 ml, (b) 260 ml, (c) 580 ml, and (d) 930 ml.

(a)

Flow rate	0.5 (l/min)	0.7 (l/min)	0.9 (l/min)	1.1 (l/min)
MTT (average)	23.85	16.00	13.20	11.97
V/Q	24.00	17.14	13.33	10.91
ψ	0.99	0.93	0.99	1.10

(b)

Flow rate	0.5 (l/min)	0.7 (l/min)	0.9 (l/min)	1.1 (l/min)
MTT (average)	25.48	20.39	17.31	13.72
V/Q	31.20	22.29	17.33	14.18
ψ	0.82	0.91	1.00	0.97

(c)

Flow rate	0.5 (l/min)	0.7 (l/min)	0.9 (l/min)	1.1 (l/min)
MTT (average)	41.24	35.30	26.69	24.03
V/Q	69.60	49.71	38.67	31.64
ψ	0.59	0.71	0.69	0.76

(d)

Flow rate	0.5 (l/min)	0.7 (l/min)	0.9 (l/min)	1.1 (l/min)
MTT (average)	61.11	40.86	37.26	33.18
V/Q	111.60	79.71	62.00	50.73
ψ	0.55	0.51	0.60	0.65

Results are shown in figure 3.14. The horizontal axis represents the theoretical values obtained from equation (3.4) (i.e., 260 ml for chamber A divided by the flow rate) and the vertical axis corresponds to various MTT values. The dotted line and the dashed line are the best-fit lines for the input and the output MTT's of chamber A based on the measured time-intensity curves. According to equation (3.5), the MTT for chamber A can be obtained by subtracting the input MTT from the output MTT. The results are shown as the dot-dashed line. The mixing chamber MTT can also be found according to equation (3.4) and results are shown as the solid line. Note that the solid line is simply a straight line with a slope of one. Apparently, the solid line is distinctly different from the dot-dashed line indicating that the concentration relationship described by equation (3.1) may not be valid.

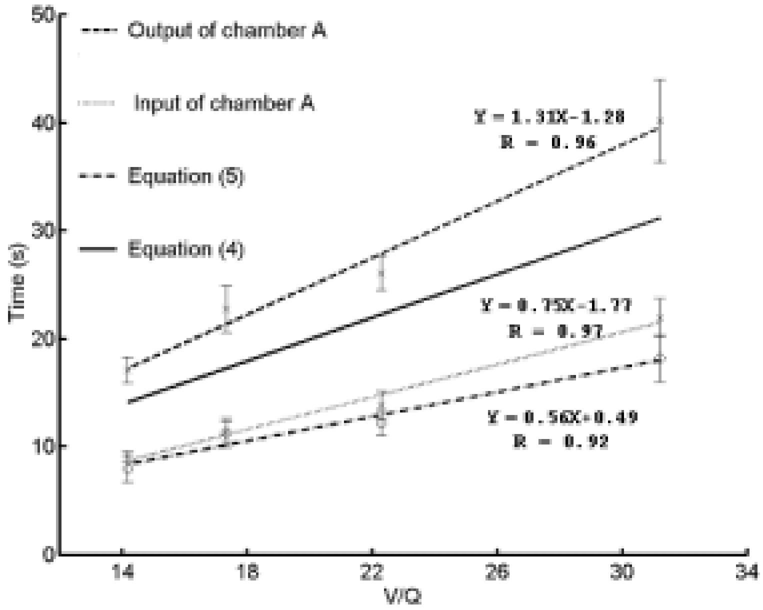

Figure 3.14 Input and output MTT's measured with two compartment phantoms in cascade (setup shown in figure 3.4).

The same experiments were performed with the setup shown in figure 3.6. The size of chamber B was 200 ml and the chamber A was replaced with a dialysis cartridge. Results are shown in figure 3.15. Similar to the results shown in figure 3.14, the convolution relationship between the input time-intensity curve and the output time-intensity curve again does not hold. Nonetheless, all the measurement results shown in figures 3.14 and 3.15 indicate that the MTT is approximately inversely proportional to the volume flow rate *Q*.

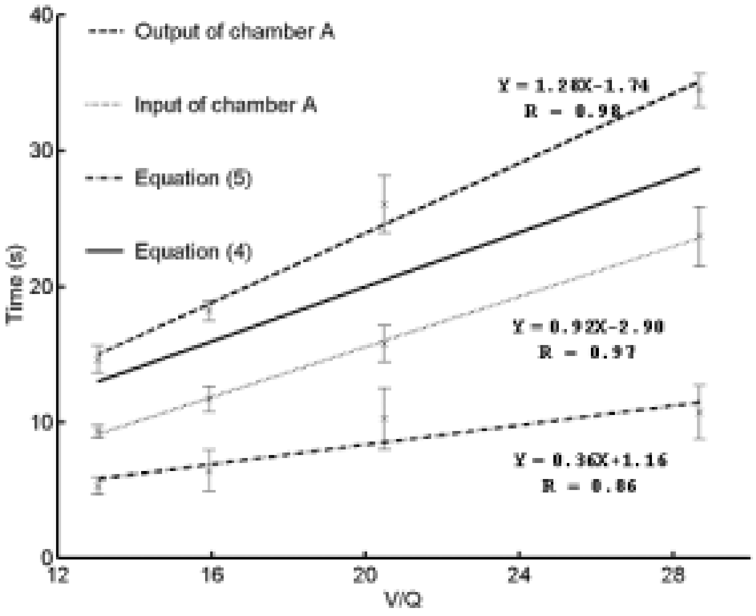

Figure 3.15 Input and output MTT's measured with the perfusion phantom in cascade with a compartment phantom (setup shown in figure 3.6).

3.4.4 Conclusions

The hypothesis that mixing of the contrast agent is a LTI process was tested in this paper. Such a study is critical in determining if deconvolution techniques can be applied for quantitative blood flow estimation. Results indicated that although the backscattered intensity increased with the concentration of the contrast agent, the measured MTT's also varied as the concentration varied. In addition, the MTT's of the mixing chamber derived based on equation (3.5) were different from the MTT's obtained based on equation (3.4). Therefore, it is concluded that the mixing process is generally not LTI and deconvolution techniques cannot be applied for measuring the absolute flow rate.

Moreover, table 3.1 showed that the MTT estimates were affected by both the volume of the mixing chamber and the flow rate. In general, the MTT estimates were closest to the theory with a smaller mixing chamber and at a higher flow rate. Although deconvolution techniques are generally not applicable, results in figures 3.13 to 3.15 showed that a linear relationship was still present between the measured MTT values and theoretical MTT values. Thus, time-intensity based methods are still feasible if only relative flow analysis is required.

In another study of this research project as section (3.4.2), the compartment flow phantom was placed both vertically and horizontally. Results showed that both configurations produced good relative estimates of flow parameters. Hence, influence of microbubbles buoyancy can be ignored when the larger diameter self-made agent was used.

3.5 Flow Measurements Based on Both Input and Output Time Intensities

Variations in the concentration of the contrast agent with time can be determined mathematically by modeling the flow system as a series of blood mixing chambers (Li et al 2002; Yeh et al 2001). However, these time–intensity-based methods are not as effective when the injection site is far away from the measurement site, in which case the time–intensity relationship at the inflow must also be taken into account. If the blood mixing chamber can be treated as a linear time-invariant system, it may be possible to apply deconvolution techniques for flow estimation if the time–intensity relationships are measured at both the input and the output of the blood mixing chamber (Yeh et al 2001). Our previous results showed that although the linear time-invariant assumption may not be valid, time–intensity-based methods are still feasible if only relative flow analysis is required.

In the present study, an *in vitro* perfusion model is set up to measure three TICs – inflow, outflow, and the perfused area – simultaneously using grayscale imaging. One purpose of this section is to evaluate the effect of shadowing on TIC-based perfusion assessment. In the perfused area, shadowing is evaluated at different regions of interest (ROIs) during different flow rates. The correlation between flow parameters and the various TICs is also discussed. Moreover, a new technique is proposed in this study for perfusion estimation based on both the inflow and the outflow TICs, and is referred to as the input–output TIC (IOTIC) method. The TIC based on the IOTIC method is compared with the TIC measured within the perfused area. The relationships between flow parameters and parameters of the IOTICs are also discussed. Note that the injection site can be far away from where the inflow TIC is measured, because both input and output time intensities are taken into account.

One potential clinical application of the IOTIC technique is to assess brain perfusion by measuring the time–intensity relationship in the extracranial flow. Specifically, the time–intensity curves are measured both in a carotid artery and a jugular vein. Therefore, the shadowing effect and the poor acoustic window can be avoided since the TIC from the brain tissue is no longer needed.

3.5.1 Input-Output Time-Intensity Curve (IOTIC) Technique

The proposed IOTIC technique monitors the acoustic intensities at both the inflow and the outflow of a perfused region. Based on mass conservation, the difference between the number of microbubbles at the output and at the input at a time t must be the same as the time derivative of the number of microbubbles in the perfusion model ($n(t)$) (Cooney et al 1976; Li et al 2002; Miles et al 1997). Thus, the number of microbubbles entering and leaving the mixing chamber at time t is $Q \times n_I(t)$ and $Q \times n_O(t)$, respectively. It can then be shown that

$$V \frac{dn(t)}{dt} = Qn_I(t) - Qn_O(t) = Q(n_I(t) - n_O(t)) . \qquad (3.8)$$

By integrating both sides of equation (3.8), we have

$$n(t) = \frac{Q}{V} \int_0^{\infty} (n_I(t) - n_O(t))dt . \qquad (3.9)$$

In other words, it is possible to evaluate the concentration in the perfused area by simultaneously measuring the TICs at the input and output ends. Moreover, $n(t)$ is inherently less noisy due to the integration term in equation (3.9).

3.5.1.1 Experimental Setup

The perfusion phantom was made from a renal dialysis cartridge (model C-12, Terumo, Tokyo, Japan). A window was made in the surface of the cartridge casing, which was then wrapped in a membrane to avoid microbubble leakage into the surrounding water tank. An additional sphere was inserted between the injection site and the perfusion phantom to simulate the situations where the injection site is far away from the measurement site (Yeh et al. 2001). Two 8-mm-diameter silicon tubes (with opposite flow directions) and the perfusion phantom were fixed in parallel and immersed in a water tank. A curved array transducer (model C4-2, Advanced Technology Laboratories, Bothell, WA) was placed 1.5 cm above the cartridge dialysis. A damper was used to stabilize the flow. To prevent recirculation of the contrast agent back in the phantom, the water only passed through the model once. A schematic diagram of the configuration is shown in figure 3.16, and the markers A, B, and C represent the ROI positions of the input, the perfused area, and the output, respectively. In this study, the Self-Made Agent-B was used.

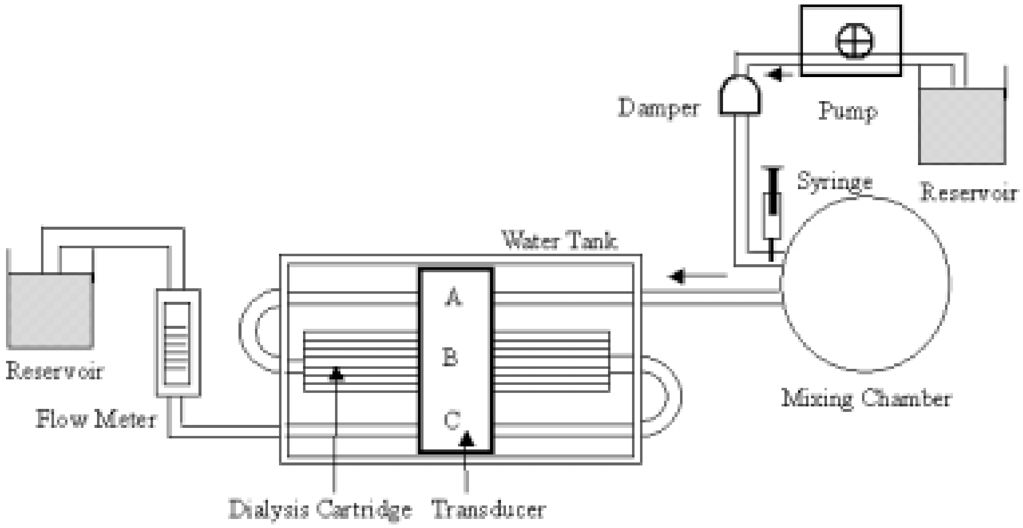

Figure 3.16 Experimental setup with a perfusion phantom.

3.5.1.2 Imaging Processing

The time–intensity relationships at the input, the output, and the perfused area were measured simultaneously using a commercial ultrasound device (Ultramark 9, Advanced Technology Laboratories). The mechanical index was 0.7 with the frame rate ranging from 20–30 Hz. Grayscale images of the transverse view of the three ROIs were acquired at the rate of one frame per second. A total of 300 image frames (i.e., 5 mins of sampling) were acquired and digitized by a frame grabber (model UPG401B, Upmost, Taipei, Taiwan) and stored for off-line analysis. The image size of 304 × 232 pixels covered an area of 72 × 55 mm. A typical image is shown in figure 3.17. The three ROIs denoted by the three circles correspond, from right to left, to the input tube, the dialysis cartridge (i.e., the perfused area), and the output tube.

The grayscale image data was converted from a logarithmic to a linear scale before the mean backscattered intensities inside the ROIs were calculated. To obtain the TICs, the inner portion of the tubes were covered by circles of different diameters. The dialysis cartridge, on the other hand, was covered by half rings of different widths. The intensities of the pixels inside the ROIs were summed, and the resulting value was used as the intensity at that particular instance. The procedure continued until all the 300 digitized grayscale images were processed.

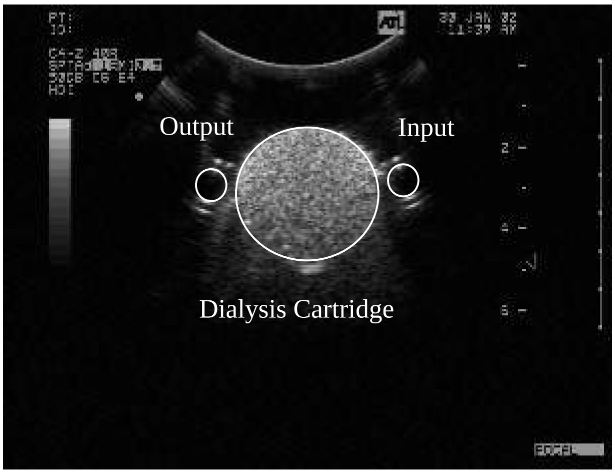

Figure 3.17 A typical grayscale image with three ROIs indicated.

3.5.2 Shadowing Effect

Experiments were conducted to evaluate the influence of the shadowing effect on the perfusion estimates. Four flow rates of 700, 900, 1100 and 1300 ml/min were used. For each flow rate, five independent measurements were performed to obtain the mean and the standard deviation. A typical TIC is shown in figure 3.18(a), for which the flow rate was 900 ml/min. It can be seen that the measured intensity decreased as the microbubbles passed through the perfusion phantom. The same effect occurred during other flow rates, and this was due to the shadowing effect induced by the microbubbles: the microbubbles were close together in the perfused area, and multipath reverberations reduced the backscattered signal. Note that relative intensity change is shown in figure 3.18(a). In other words, the backscattered intensity before microbubbles entered the dialysis cartridge was used as the baseline. As microbubbles passed through the capillaries, the shadowing effect occurred and it made the summed intensity negative.

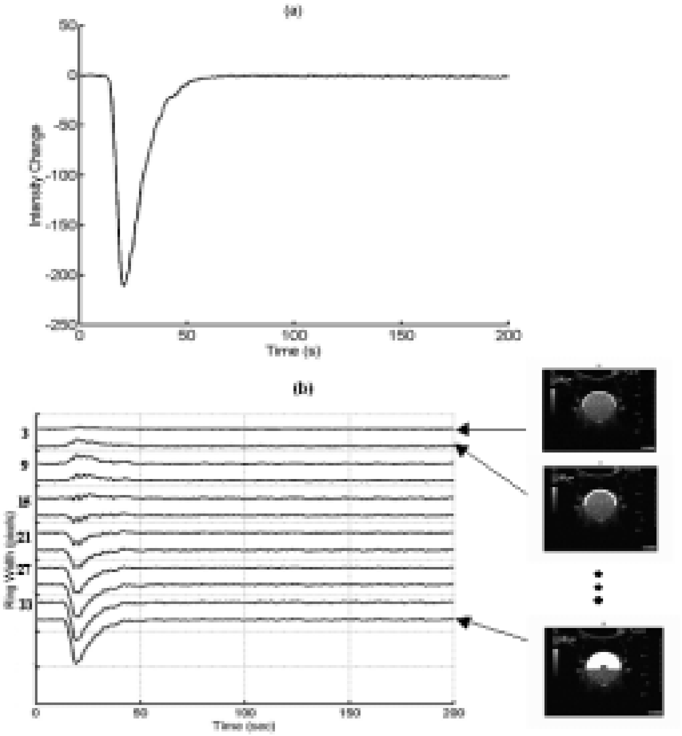

Figure 3.18 Time–intensity curves (TICs) are obtained using (a) a circle as the ROI, and (b) half-rings with different widths as ROIs. The flow rate was 900 ml/min.

To further explore the shadowing effect, various ROIs were used. The ROIs were half-rings with various widths covering the upper portion of the dialysis cartridge. The TICs corresponding to different degrees of shadowing effect can be obtained by changing the ring width (in number of pixels) of the specific ROI. Figure 3.18(b) displays the TICs for various ring widths: the ring width increased from top to bottom, with a step size of 3 pixels between each curve. The upper TIC is for a ring width of 3 pixels; in this case the intensity increased as the contrast agent passed through the ROI. As the ring width increased, the intensity became smaller as the agent passed through the ROI. These results indicate that the shadowing effect depends on the size and position of the ROI, and hence illustrates the importance of defining the ROI correctly in studies of this type.

Figure 3.19 demonstrates the relationship between the AUC and the ROI ring width. Figure 3.19(a)–(d) show the results at flow rates of 700, 900, 1100 and 1300 ml/min, respectively. The horizontal axis represents the ring width (in number of pixels) and the vertical axis is the AUC of the TIC. The average values are shown, with the error bars representing ± one standard deviation. Similar to figure 3.18, relative AUC changes are shown and thus the values become negative when the shadowing effect is significant. The results show that the AUC varies with the ring width. The AUC values increased for ring widths up to 5–9 pixels, and decreased for larger values. The shadowing effect becomes significant as the width of the ROI center increases.

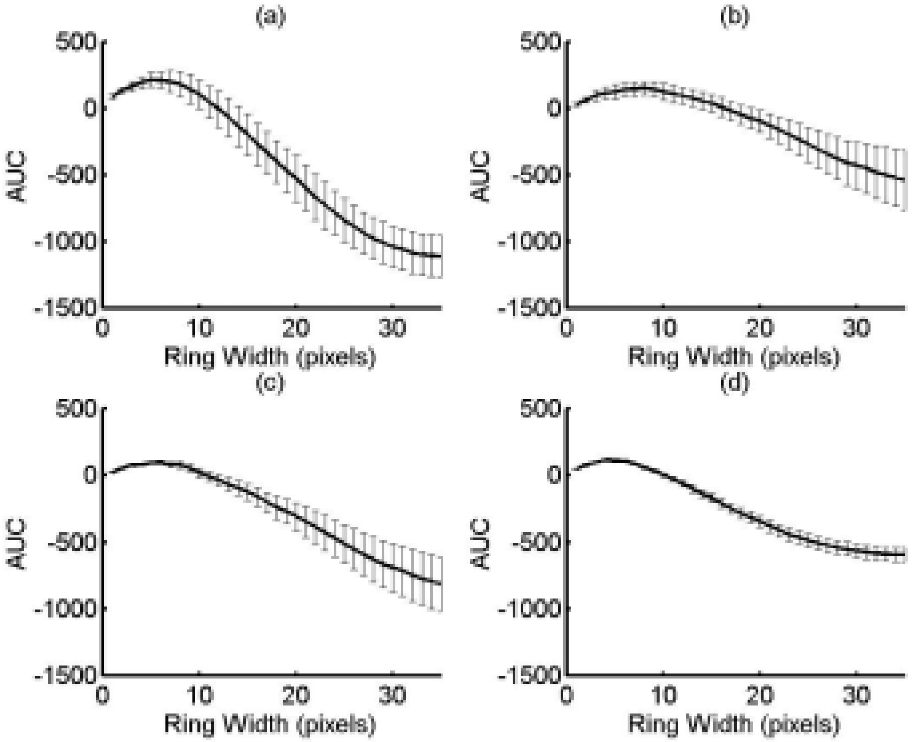

Figure 3.19 AUC of the TIC vs. ROI width at flow rates of (a) 700, (b) 900, (c) 1100, and (d) 1300 ml/min.

The ring width that corresponds to the maximum AUC at each flow rate is shown in figure 3.20. The maximum AUC illustrates that the TIC suffered the least shadowing effect. The results also demonstrate that the shadowing effect is related to flow rate.

Figure 3.21 shows the relationship between the MTTs and the ring width, with figures 3.21(a)–(d) showing the results at flow rates of 700, 900, 1100 and 1300 ml/min, respectively. The horizontal axis represents the width of the half ring and the vertical axis shows the MTTs of the TICs. The estimated MTTs are shown by solid lines and the theoretical MTTs (according to equation (3.4)) are shown by dotted lines. Note that since the transducer was placed at the middle of the cartridge, the perfusion volume was half of the total cartridge volume. Thus, the theoretical value was calculated based on the sum of the volume of the hollow sphere (260 ml), one half of the cartridge volume (39.5 ml), plus the connection tubing (15 ml) (i.e., 260+15+39.5 = 314.5 ml). The solid line is clearly different from the dotted line, and the MTTs varied with the shadowing effect.

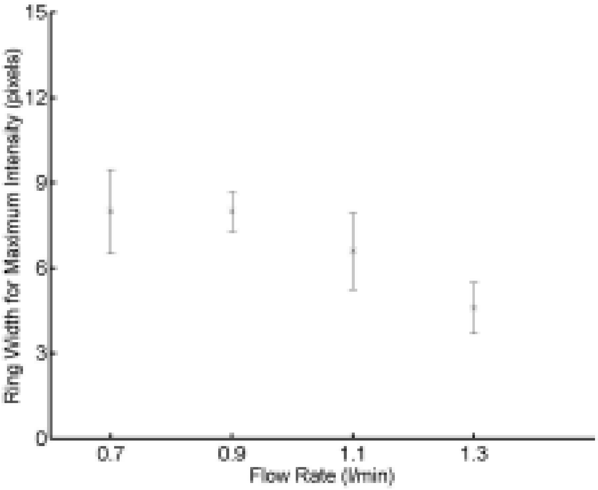

Figure 3.20 The maximum width (in pixels) that corresponds to the maximum AUC, vs. flow rate.

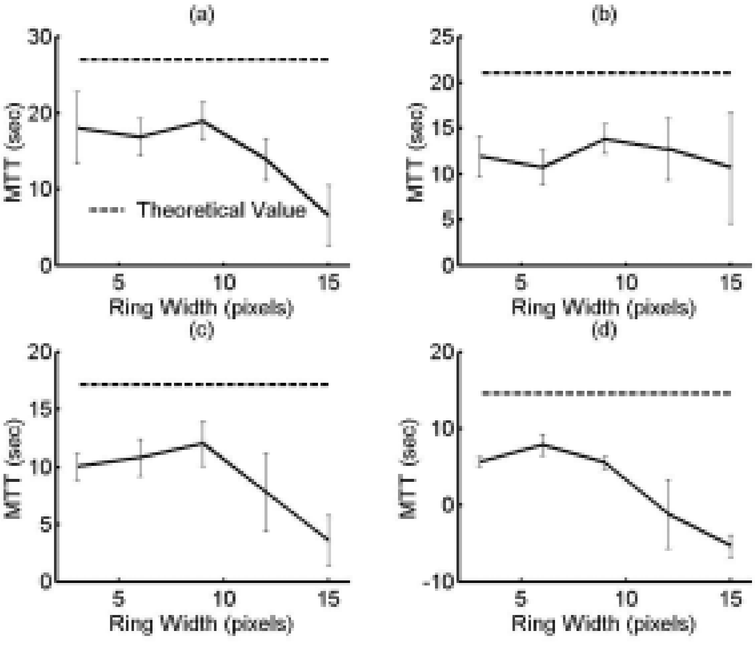

Figure 3.21 The MTT estimates for flow rates of (a) 700, (b) 900, (c) 1100, and (d) 1300 ml/min.

3.5.3 Input–Output Time–Intensity Curve Technique

Figure 3.22(a) shows typical TICs from experimental data. A flow rate of 900 ml/min was used. The input, the output, and the perfusion TICs obtained from raw grayscale images are shown as the dashed, dotted, and solid lines, respectively. Note that the ROI that corresponded to the maximum AUC (as shown in figure 3.18(b)) was used to obtain the perfusion TIC.

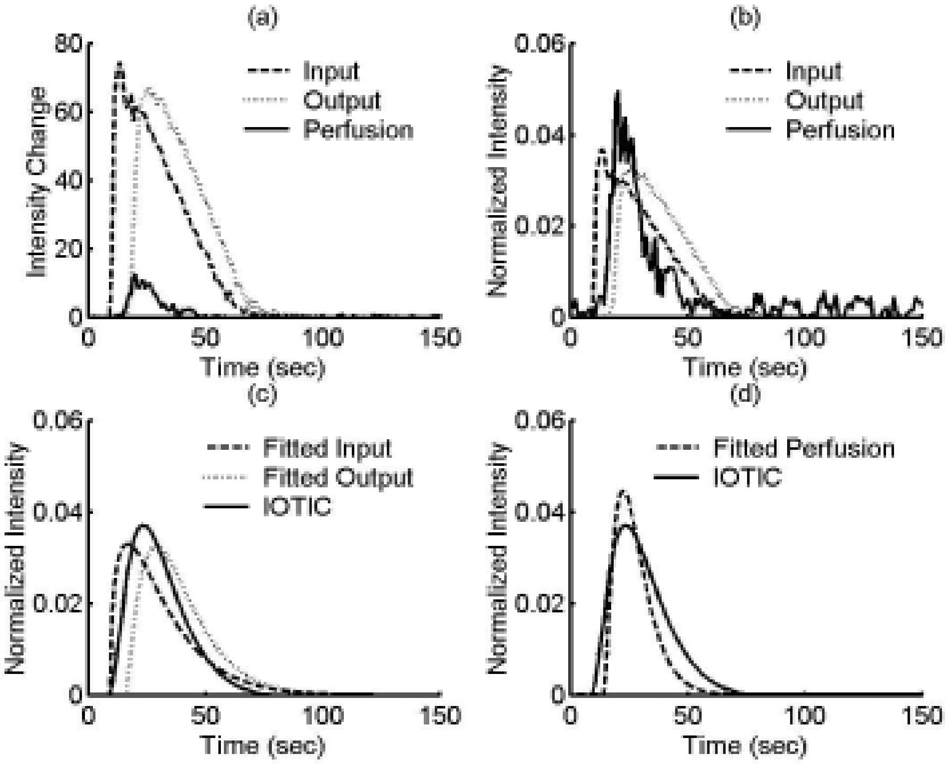

Figure 3.22 (a) The input, output, and perfused-area TICs obtained from grayscale images. (b) Normalized TICs. (c) Gamma-function-fitted input and output TICs and the derived IOTIC. (d) Direct measurement (dashed line) vs. IOTIC (solid line).

In this section, destruction of microbubbles by the acoustic stimulation was assumed negligible, based on the fact that the ratio of the input AUC to the output AUC was close to unity. Figure 3.22(b) shows the three TICs, with the AUC of each curve normalized to unity. After gamma-function fitting, the fitted input and output TICs are shown in figure 3.22(c) by the dashed and dotted lines, respectively. Finally, the directly measured perfusion TIC (after fitting) and the calculated IOTIC are shown in figure 3.22(d) by the dashed and solid lines, respectively. The calculated TIC was obtained from equation (3.9) using the fitted input and output TICs. Note that the parameters derived from the two curves are likely to be different.

The two TICs as shown in figure 3.22(d) were used to determine four flow parameters as a function of the flow rate: MTT and time constant. The results are shown in figures 3.23 and 3.24. The results of the measured perfusion TICs and the TICs obtained from the IOTIC technique are shown in each figure by the dotted and dashed lines, respectively. Linear regression was performed, and the lines of best fit are shown by the solid lines. The horizontal axis represents the flow rate and the vertical axis indicates to the specific flow parameter. The results shown in figure 3.23 correspond to the estimated MTTs at four flow rates. The correlation coefficients between the estimated MTTs and the best-fit lines were 0.91 and 0.90, respectively. The high correlation coefficients indicate that relative flow measurement is possible with both time-intensity based methods.

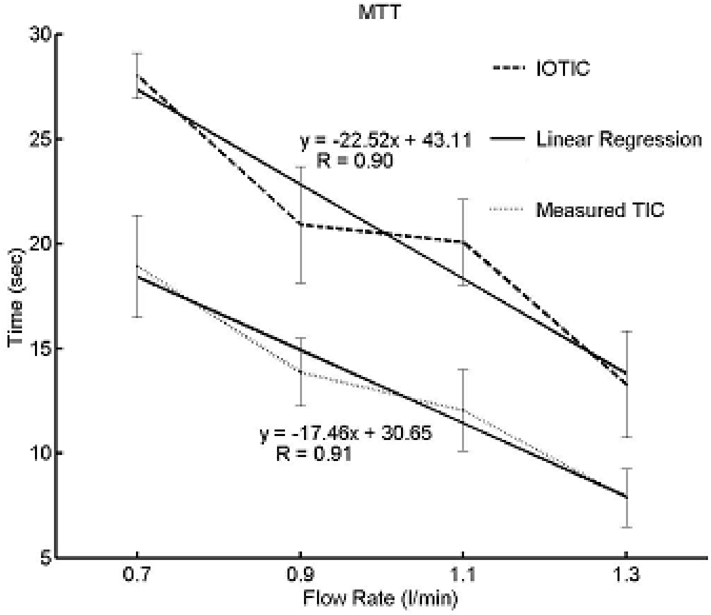

Figure 3.23 MTT estimates vs. flow rates. The dashed, dotted, and solid lines represent the results of IOTIC, measured TIC, and linear regression, respectively.

Finally, the estimated time constants (i.e., τ in equation (3.4)) from measured TICs and TICs obtained using the IOTIC technique are shown in figure 3.22. The time constant was determined from the best least-squares fit between the TIC and an exponential function. Only the portion of the TIC after the peak intensity was used.

The correlation coefficients between the estimated time constants and the best-fit lines are 0.96 for the IOTIC method and 0.63 when derived from the measured TIC.

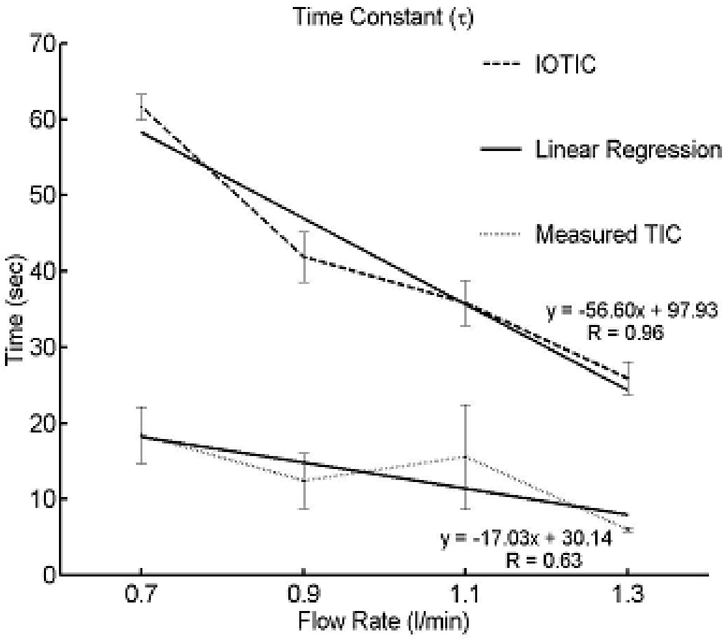

Figure 3.24 Time constant vs. flow rates. The dashed, dotted, and solid lines represent the results of IOTIC, measured TIC, and linear regression, respectively.

The results shown in figures 3.23 and 3.24 demonstrate that parameters estimated on the basis of the TICs using the IOTIC method generally had higher correlation coefficients with the flow rates than when the directly measured TICs were used. The estimated parameters from measured TICs are all smaller than those obtained by the IOTIC method. Moreover, relative perfusion flow estimation is possible using the IOTIC technique, and this technique only uses the input and output TICs to derive the perfusion parameter and thus avoids the shadowing effect.

4. Chapter 4: Microbubbles Destruction/Reperfusion System[3]

4.1 Introduction

Main goals in this chapter are to create a high-frequency ultrasound system in combination with the use of ultrasound contrast agents to functionally evaluate microvascular blood flow with a very high resolution. A new signal processing approach is proposed and can robustly estimate the very rapid flow in small arteries as well as the slow flow in capillaries.

In this part, we do not excite microbubbles substantial nonlinear modes of oscillation, but instead detect the microbubble based on its strong scattered echoes and movement through the microvasculature.

4.1.1 High-Frequency Ultrasound Imaging

Since resolution improves with increasing ultrasound frequency, we choose to create an image based on the transmission of 25 MHz pulses, which provide a spatial resolution on the order of 100 microns. High frequency ultrasonic imaging systems have been developed for noninvasive imaging of small scale superficial structures such as the skin (Turnbull et al 1995), the anterior chamber of the eye (Pavlin and Foster 1998, Silverman et al 2001), and mouse embryos (Aristizabal et al 1997). More recent improvements include color Doppler (Goertz et al 2000; Kruse et al 1998, 2002) and power Doppler (Goertz et al 2002; Kruse et al 2002) imaging modes which allow mapping of blood velocity and power, respectively, with spatial resolution down to 40 μm at 40 MHz.

In vivo studies using these modes include differential studies of the effects of vasoactive drugs (Silverman et al 1999), temperature (Silverman et al 2002), and laser ablation (Kruse et al 2002) on blood velocity and power in the ciliary body of the

---

[3] The Chapter is based on the work presented at *IEEE Medical Imaging*, 2003.

rabbit eye at frequencies ranging from 20 to 40 MHz. Another application of high frequency ultrasound is imaging the effect of anti-angiogenic drug treatment in mouse tumor models at 25 MHz (Goertz et al 2002). These previous systems have not been capable of evaluating flow in the entire microcirculation, however, instead vessels with a diameter below 40 microns were not detected.

4.1.2 Fragmentation of Contrast Agent

The unique characteristic of ultrasound contrast agents is that they can be fragmented after suitable acoustic excitation (Chomas et al 2000, 2001). Following an expansion on the order of 300%, a microbubble will rapidly collapse and can divide into small fragments (Chomas et al 2001). It is clear that contrast agents can be reliably destroyed using ultrasound pulses with a center frequency below 5 MHz (Chomas et al 2001), where decreasing the center frequency reduces the threshold pressure required for microbubble destruction. In this chapter, we use an acoustic measurement procedure to obtain a pressure threshold for bubble destruction for which the agent appears to be completely destroyed when immediately sampled by high frequency ultrasound.

Following destruction of the contrast agent with a low frequency pulse, the flow of agents into the sample volume can be monitored over time to produce a local estimate of the velocity of flow in a region of the microvasculature. This replenishment of the contrast agent results in a gradual increase in the echo amplitude that is typically shown as a wash-in time-intensity curve.

Contrast-assisted techniques that quantitatively estimate wash-in TICs from within the perfused area have been proposed (Chomas et al 2001; Wei et al 1998; Wilkening et al 2000) and applied to study contrast agent replenishment in rat tumors (Chomas et al 2001) and other disease models. Wei et al. (1998) proposed a method for the assessment of blood flow velocity in the myocardium by acquiring triggered images following a venous constant injection, and suggested a rising exponential as a signal model for received echo amplitude as a function of time. The non-destructive imaging was performed in harmonic mode, where ultrasound was transmitted at 2 MHz and received at 4 MHz. Good correlation was found between volume flow rate and the exponential rate constant. Chomas et al. (2001) used phase-inversion sub-harmonic imaging for non-destructive observation of the replenishment of contrast agents after bubble destruction in rat tumor models. The time to achieve 80% intensity was adopted to indicate differences in flow rate and was calculated directly from an estimate of the rate constant in 800 by 800 μm regions-of-interest (ROI).

4.1.3 Scope

In this chapter, we propose a new high frequency destruction/replenishment imaging system with a spatial resolution of 160 by 160 μm, and with the ability to estimate pulse-to-pulse motion of contrast agents within a sub-resolution ROI. With this system, it should be possible to separate regions where flow is dominated by capillaries from those dominated by arterioles (Chomas et al 2001). With this higher resolution, the number of contrast agent microbubbles within a single region of interest is small, and therefore estimates of flow based on the movement of these contrast agents can be noisy. In order to reliably estimate flow based on this small number of contrast agent microbubbles, we also propose a new technique to estimate the replenishment rate, and thus the time to achieve 80% replenishment from the TICs. In this technique, we integrate the TIC, producing a smoother function from which to form our estimate, and derive an appropriate estimator that employs this integrated TIC.

4.2 Destruction/Replenishment Methodology

Assuming that a contrast agent is infused at a constant rate and concentration, after a period of time a steady state concentration is reached throughout the circulation. Local application of high pressure ultrasound pulses destroys microbubbles within a confined volume, and intact microbubbles enter this volume at a rate determined by flow velocities and vessel topology. Non-destructive imaging sequences interrogate the same volume, and the changes in the backscattered intensity as a function of time are referred to as the time-intensity curve.

4.2.1 Wash-in Time-Intensity Curve

A model of the wash-in TIC is adopted from Wei et al. (1998) where it was used to study myocardial replenishment. The model describes the echo intensity resulting from the summed contributions of all microbubbles within the sample volume that enter following destruction. From a linear system perspective, the model is achieved by convolving the input function following destruction (modeled as a scaled unit step function), with the beam sensitivity function (modeled as a scaled rectangular function). The resulting ramp function has a plateau value defined by *B*, which occurs at time, *T*, indicating that microbubble concentration is completely restored within the sample volume. An offset intensity at time zero, *A*, is included to account for echoes from stationary scatterers or noise from the same volume. To approximate non-uniform flow velocities and backscattered amplitudes of bubbles entering the sample volume (e.g. different *T*s and *B*s), the ramp function is approximated by a rising exponential. The resulting equation for the received signal amplitude, *I(t),* as a function of time after destruction is given by the following exponential function

$$I(t) = A + (B - A)(1 - e^{-\beta t}) , \tag{4.1}$$

where A is the received echo magnitude immediately after contrast agent destruction (includes tissue echoes); B is the steady state value of the received echoes; and β is the rate constant that determines the rate of the rise of the exponential and is proportional to the blood flow velocity. Given the elevational beam width (*E*) of the low frequency transducer (1 MHz in this case), β is proportional to the mean velocity (*v*) of microbubbles (Wei et al 1998).

$$\beta = \frac{v}{E} \tag{4.2}$$

It should be noted that this model does not account for attenuation (e.g. frequency shift), divergence, and diffraction; nor does it account for probabilistic factors including non-uniformities in velocity, scattering amplitude, and destruction.

4.2.2 Model Fitting and Integrated Time-Intensity Curve (ITIC)

Wash-in time intensity curves are typically noisy due to a range of factors, including velocity spread from different vessels within the same sample volume, decorrelation, cardiac pulsatility, and variability in bubble scattering. There is a tradeoff between resolution and variance, and there may be useful information contained within the spatial variability of the echo amplitude over time (e.g. a mixture of a small artery and many arterioles and capillaries within the same sample volume).

In this study, *in vitro* and *in vivo* estimates of flow are obtained by sending a pulse train containing 100 high frequency pulses after the destructive pulse, each with an interpulse interval on the order of 100 ms. Therefore, data are acquired for a total duration of approximately 10 seconds following the destructive event. We find that 80% contrast replenishment in the entire region of interest requires approximately 8 seconds within regions dominated by capillaries and therefore this pulse train is sufficiently long. Intravital microscopy measurements of blood flow velocities show that flow velocities within vessels smaller than 200 μm range from 0.5-10 mm/s, with mean velocities of approximately 1 mm/s (Zweifach and Lipowsky 1985).

To further improve tissue echo suppression, the echoes from adjacent pulses are aligned prior to estimation and filtering using alignment techniques as described in (Zagar et al 1998). A correlation-based speckle tracking algorithm is then utilized prior to high-pass filtering in order to align adjacent regions across pulses.

Assuming that tissue echoes change slowly over the multi-pulse acquisition, thus making them band-limited across frames, a step initialized infinite impulse response (IIR) high-pass filter is applied to remove them, similar to wall-filtering in Doppler processing. In most regions of the image, the contrast agent echoes decorrelate quickly with respect to the pulse index, and therefore this high-pass filter can be applied in the pulse index dimension. Due to the extent of tissue motion for *in vivo* experiments, the wall-filter is applied on the B-mode data, rather than the radiofrequency data for improved rejection of tissue echoes.

Following the use of a high-pass filter to remove tissue echoes, the parameter, A, is nearly zero in the frame following microbubble destruction. To insure that microbubble echoes produced by destruction do not influence the flow estimates, the imaging pulses are delayed from the destruction pulses by tens of microseconds. This short delay insures that the first frame following destruction does not contain the contrast agent, and therefore A is assumed to be zero.

A modified approach is adopted in this study for acquiring and estimating the rate constant from integrated TIC data, in order to reduce parametric variability and sensitivity. Given that A and B are determined, an estimate of β could be obtained using equation (4.1) to fit the wash-in TIC. In order to reduce the noise influence in the time-intensity measurements, an integrated time-intensity curve (ITIC) method to estimate β was used in this study. Assuming that A is equal to zero and by integrating equation (4.1) from zero to t, and dividing by time, we have:

$$I'(t) = \frac{\int_0^t I(\tau)d\tau}{t} = \frac{B}{t\beta}(e^{-\beta t} - 1) + B\,, \tag{4.3}$$

where t is the time elapsed from bubble destruction. Note that in the limit, $t \to 0$, $I'(t) \to 0$, and in the limit, $t \to \infty$, $I'(t) \to B$, just as for equation (4.1) with $A = 0$. Thus, an estimate of B is found by averaging the last intensities of ITIC in this method. The ITIC, $I'(t)$, is inherently less noisy than the TIC. Therefore, an estimate of β with smaller variance is obtained using the ITIC to fit the model in equation (4.3).

4.2.3 Time to Achieve 80% Replenishment

A relevant parameter that can be directly inferred from the estimate of β is the time to achieve 80% replenishment ($T_{80\%}$). $T_{80\%}$ is a normalized measure of the rate at which a tissue is replenished with the contrast agent. Based on equation (4.1), $T_{80\%}$ can be derived as

$$T_{80\%} = -\frac{\ln(0.2)}{\beta} \tag{4.4}$$

If $T_{80\%}$ in equation (4.4) is substituted for t in equation (4.3), the following is obtained:

$$\frac{I'(T_{80\%})}{\lim\limits_{t\to\infty} I'(t)} = \frac{\frac{1}{T_{80\%}}\int_0^{T_{80\%}} I(\tau)d\tau}{B} = 1 + \frac{1}{\beta T_{80\%}}(e^{-\beta T_{80\%}} - 1) \cong 0.5029 \cdot \qquad (4.5)$$

Equation (4.5) shows that time to achieve 80% replenishment for a given TIC is approximately equal to the time to achieve 50% of the corresponding ITIC, therefore this time is referred to as $IT_{80\%}$.

4.3 Destruction Threshold Determination

An acoustical method was designed to determine the threshold pressure for bubble destruction, and to insure that destruction was sufficient to prevent bias when estimating flow parameters using the high frequency imaging methods in the proposed system.

4.3.1 Destruction Threshold Setup

A block diagram of the experimental system is shown in figure 4.1. The setup consists of two single element transducers, a 25 MHz spherically focused transducer with a 0.25” element (model V324, Panametrics, Waltham, MA), and a 1 MHz cylindrically focused transducer (model V303, Panametrics, Waltham, MA) with a 0.5” element. Relevant specifications of the transducers are summarized in table 4.1. The cylindrical focus of the 1 MHz transducer results in a planar beam. With this planar beam, the contrast agent can be destroyed within an entire plane of interest with a single pulse.

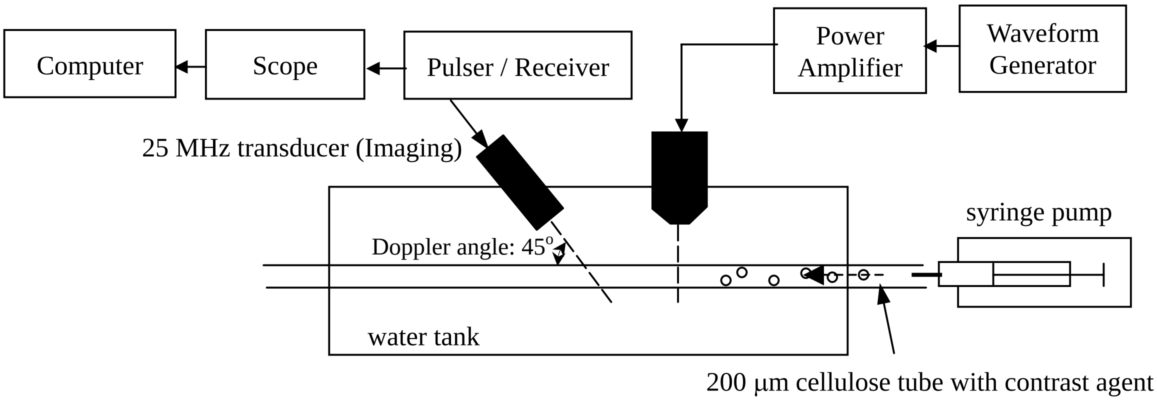

Figure 4.1 Experimental arrangement for the threshold of bubble destruction measurements.

The 25 MHz transducer is fixed at a 45-degree angle with respect to a 200-μm diameter cellulose tube (Spectrum Medical, Laguna Hills, CA) near the outlet of a tube, with the focal region aligned with the tube. The 1 MHz transducer is fixed approximately 7 cm upstream from the 25 MHz transducer on the inlet side of the tube, perpendicular to the tube, and with the tube perpendicular to the line defining the focus. Acoustically-absorbent rubber is placed at the bottom of the tank to minimize reflections.

An arbitrary waveform generator (model HP 33120A, Hewlett-Packard Company, Palo Alto, CA) is used to generate 1 MHz tone bursts with 1-10 cycles, and an RF power amplifier (model 3200L, ENI, Rochester, NY) amplifies the pulses to produce the corresponding acoustic pressures ranging from 0 to 0.6 MPa. The commercial contrast agent Definity® (Bristol-Myers Squibb Medical Imaging Inc., N. Billerica, MA) is used at a concentration of 6 μL Definity®/10 mL water (3 mL/5 L blood volume). A syringe pump regulates the flow rate of contrast agent solution through the tube at 1 mL/hr (8.9 mm/s average). The 1 MHz pulses are transmitted with a pulse repetition frequency (PRF) of 50 Hz, where primary and secondary radiation forces are insignificant (Dayton et al 1997).

Table 4.1 Transducer characteristics

	Destruction (V303)	Imaging (V324)
Central frequency	1 MHz	25 MHz
Element diameter	12.70	6.35
Focal length	15.01	12.85
-6 dB bandwidth	78.2 %	51.5 %
-6 dB (-3 dB) depth of focus	15.54 (8.29)	1.40
-6 dB (-3 dB) lateral beam width	11.09 (7.99)	0.12
-6 dB (-3 dB) elevational beam width	3.24 (2.36)	0.12

Units: (mm)

Simultaneous with transmission at 1 MHz, the 25 MHz transducer operates in a pulse-echo mode to detect the presence of bubbles in the tube. Transmission by the 25

MHz transducer is accomplished using a pulser/receiver (model 5900PR, Panametrics, Waltham, MA) through a transformer diplexer/diode limiter circuit at a PRF of 1 kHz. The received echoes are amplified by 31 dB with a low-noise pre-amplifier (model AU-1114-BNC, Miteq, Hauppauge, NY) and then further amplified or attenuated by the pulser/receiver. The RF echoes are digitized at 125 MSPS using a high-speed 12-bit A/D board (model PDA12A, Signatec, Corona, CA) and stored in M-mode format on a PC for offline processing in Matlab® (Mathworks, Natick, MA).

4.3.2 Results for the Threshold of Destruction

The effect of pulse length and acoustic pressure at 1 MHz on microbubble destruction were tested using 1, 3, 5, and 10 cycles and 0-0.6 MPa, respectively. One M-mode recording of 256 axial samples (1.5 mm) for each pulse, and 2048 pulses (2.048 seconds) was acquired for each pressure and pulse length setting, and divided into 8 groups of 256 pulses for statistical analysis. A second order IIR high-pass filter was used to remove stationary echoes from the wall of the tube, as well as wall reverberation echoes that appeared directly below the tube. Figures 4.2(a) and (b) show the RF and wall-filtered baseband M-mode images, respectively. In figure 4.2(a), the wall reverberation signal appears at a depth of 0.35 mm. The pulsatile modulation over time evident in the echo amplitudes in figure 4.2(b) was produced by the syringe pump.

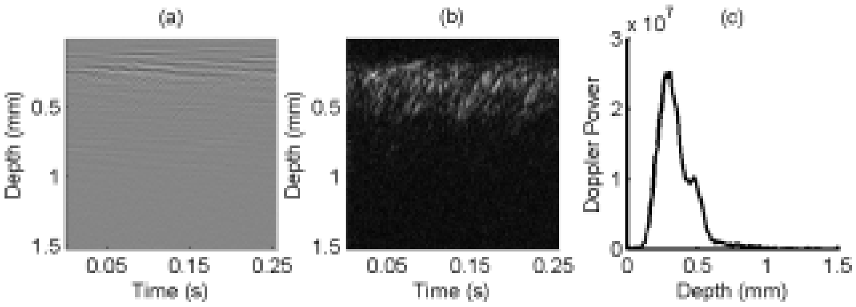

Figure 4.2 (a) RF M-mode image. (b) Wall-filtered baseband M-mode image. (c) Sum of the wall-filtered echo power over the time variable in (b).

Post-wallfiltered power, defined as the square of the baseband signal amplitude, was used to assess microbubble destruction in this experiment. The bubbles were considered destroyed when the echo power received with the imaging pulses was less than 1% of that recorded before microbubble destruction. Since microbubble echoes are detected far above their linear resonance frequencies, and the microbubbles are small compared to a wavelength at 25 MHz, we assume that they behave as Rayleigh scatterers. Thus, backscattered power is proportional to the number of intact microbubbles within the tube. Post-wallfiltered power is first integrated over time, as shown in figure 4.2(c), and the resulting curve is integrated over depth. The integration was performed over a region windowed in depth to reject duplicate echoes due to reverberation. For consistency, the same windowed region was used for all data.

Figures 4.3(a)-(d) show the post-wallfiltered power integrated over the pulse index (time in figure 4.2) as the 1 MHz pulse length is varied between 1, 3, 5, and 10 cycles, respectively, and the acoustic pressure is varied from 0 to 0.6 MPa. The error bars show one standard deviation estimated from 8 M-modes recorded at each setting. The destruction thresholds of figures 3(a)-(d) correspond to 0.63, 0.53, 0.52, and 0.43 MPa for the 1, 3, 5, and 10 cycle pulses, respectively. The results indicate that the threshold of bubble destruction decreases with increasing pulse length. Based on these findings, the 1 MHz pulse used for microbubble destruction was chosen to be 5-cycles at 0.52 MPa, which was used for the remainder of this study.

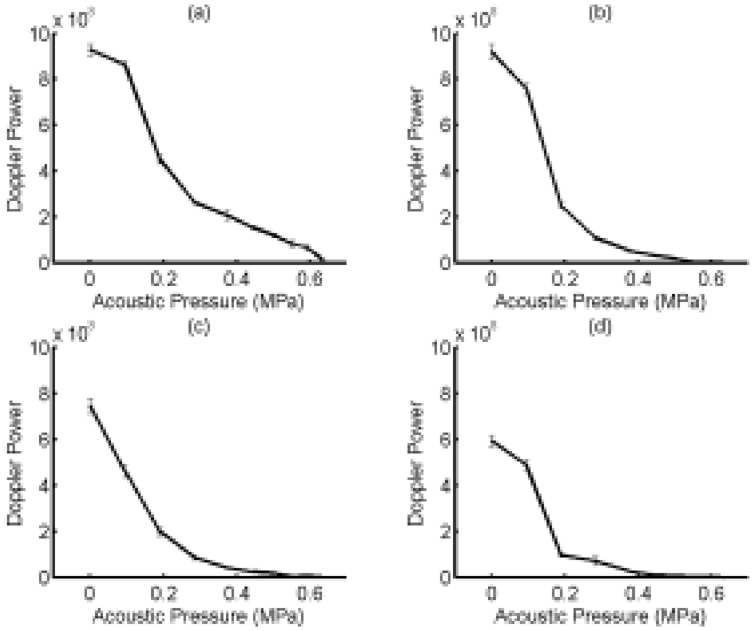

Figure 4.3 Wall-filtered echo power as a function of transmission pressure for a 1 MHz transducer with (a) 1, (b) 3, (c) 5, and (d) 10 cycle transmitted pulses.

4.4 High Resolution Destruction/Replenishment System

4.4.1 System Description

The primary components of the destruction/replenishment system include: data acquisition, pulse generation and motor control. The system is a modified version of the high frequency ultrasound scanner described elsewhere (Kruse et al 2000), with a schematic diagram of the system shown in figure 4.4. The same pair of transducers (refer to table 4.1 for specifications) used for determining the destruction threshold was fixed in a confocal arrangement using a machined holder. The minimum angle of separation between the transducers is approximately 42 degrees, which is limited by the physical dimensions of the transducer casings and their respective focal depths. A cylindrical geometry is chosen for the 1 MHz transducer because of the need to focus the destruction pulses in a plane aligned with the scanning plane of the 25 MHz transducer.

The transducer holder is affixed to a high-speed 3-D motion stage. A motion controller (model DMC-2060, Galil Motion Control, Rocklin, CA) and a data acquisition system are coordinated by software running on a PC. Transmission and reception at 25 MHz transducer and transmission at 1 MHz are accomplished using the same system detailed above. TTL triggers for the imaging and destruction sequences are generated at specified encoder increments of 16 μm as the transducers are scanned. Using a counter/timer board (PCI-6602, National Instruments, Austin, TX), each trigger is synchronized with the sampling clock to eliminate trigger jitter.

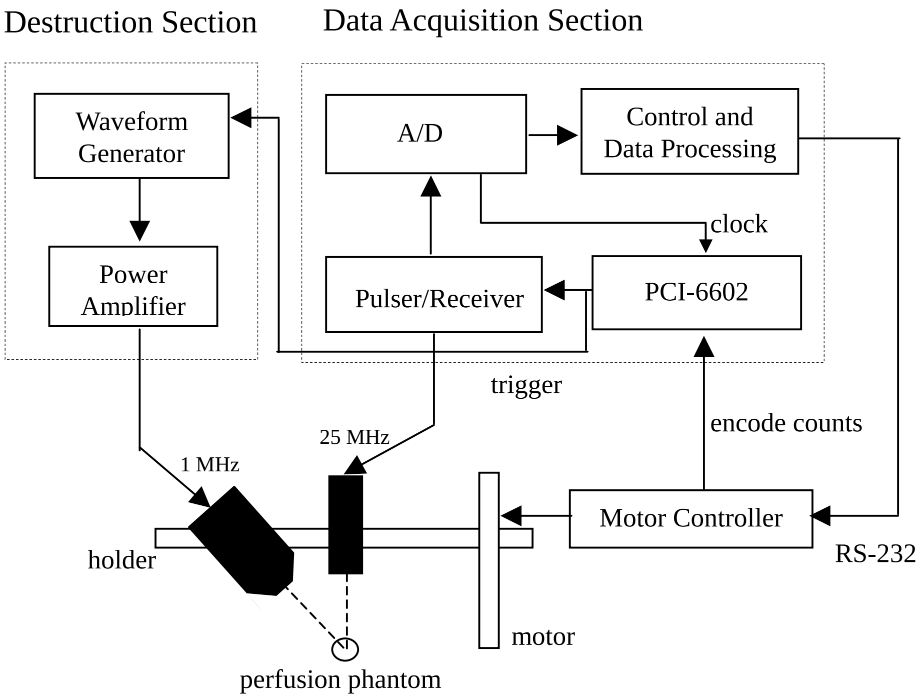

Figure 4.4 Schematic diagram of high-frequency destruction/replenishment system.

4.5 *In Vitro* Experiments

4.5.1 Perfusion Flow Phantom

To test the system, a new flow phantom has been developed capable of generating very low flow velocities typically found in the microcirculation and ranging from 0.1 to 5 mm/s. The flow tube portion of the phantom was machined from a low attenuation plastic called RexoliteR (Curbell Plastics, Glenshaw, PA), which has a loss of 1.1 dB/mm at 30 MHz (Haifeng et al 2001). The inner diameter of the phantom is 5 mm with a wall thickness of 0.5 mm and it is 25 mm long. In order to simulate the microcirculation, a small amount of cotton (less than 0.01 grams) is placed inside to simulate tissue scattering and flow randomization. The flow rate of the contrast solution in the phantom is controlled using a syringe pump. A magnetic stir bar inside the syringe is used to keep the solution mixed. A flexible buffer made of latex between the phantom and the syringe pump is used to dampen pulsatile flow and vibration produced by the syringe pump.

4.5.2 Data Analysis and Results

To illustrate the system's performance, B-mode images are shown in figure 4.5 for a flow rate of 90 mL/hr (1.26 mm/s) with a mixture of 40 μL contrast/100 mL water. The images are 3.15 mm in depth by 1.02 mm in width, and were acquired at a frame rate of approximately 10 fps. The displayed dynamic range is 40 dB. The pulse train consisted of 1 frame immediately following destruction, and 99 more post-destruction frames for a total of 100. The top 5 images are acquired without cotton, and the bottom five panels are acquired with cotton placed in the phantom. Figure 4.5(a) shows the pre-destruction image with scatter from intact microbubbles. The first frame after bubble destruction is shown in figure 4.5(b), and figures 4.5(c)-(e) are acquired at 0.5, 1 and 2 seconds following destruction, respectively.

To look at the influence of ROI size on estimates of $T_{80\%}$ and $IT_{80\%}$, three square regions with different sizes were selected concentric with the ROI shown in figure 4.5(a). Echo intensities from within the ROI shown in figure 4.5(a) were summed at each time point to create the TICs shown in figure 4.6(a)-(c), where the TICs (solid lines) correspond to ROI square sizes of 160 by 160 μm, 320 by 320 μm and 480 by 480 μm, respectively.

All nonlinear fits were performed using a nonlinear least squares algorithm (lsqnonlin function in Matlab®). B was estimated from the last 10 values in the TIC curve. Using the estimated values of B and β obtained from fits to equation (4.1) with A set to zero, fits to the TICs (dotted lines) are plotted in figures 4.6(a)-(c). The ITICs were then calculated by integrating the TICs, and fit to a model based on equation (4.3) to obtain a second estimate of β. Figures 4.6(d)-(f) show the normalized ITIC (solid lines) and normalized ITIC fits (dash-dotted lines). In this case, B was estimated from the last 10 values in the ITIC curve. Estimates of B and β from the ITIC fits were used to calculate the corresponding TIC curves shown in figures 4.6(a)-(c) (dashed lines) and in normalized form in figures 4.6(d)-(f) (dashed lines). In figures 4.6(d)-(f), the symbols ‘+’ and ‘o’ denote the $T_{80\%}$ and $IT_{80\%}$, respectively, where $T_{80\%}$ is from the TIC obtained from the fit to the ITIC, and $IT_{80\%}$ is obtained by searching for the 50% level in the ITIC. From figures 4.6(d)-(f), $T_{80\%}$ estimates are 1.30, 1.31, and 1.36 s and $IT_{80\%}$ estimates are 1.35, 1.34 and 1.40 s. Predictions of β based on equations (4.2) and (4.4) were calculated using one-half of the one-way elevational beam width of the destruction transducer (E = 1.18 mm) and the mean flow velocity (v = 1.26 mm/s), which resulted in a predicted value of 1.51 s.

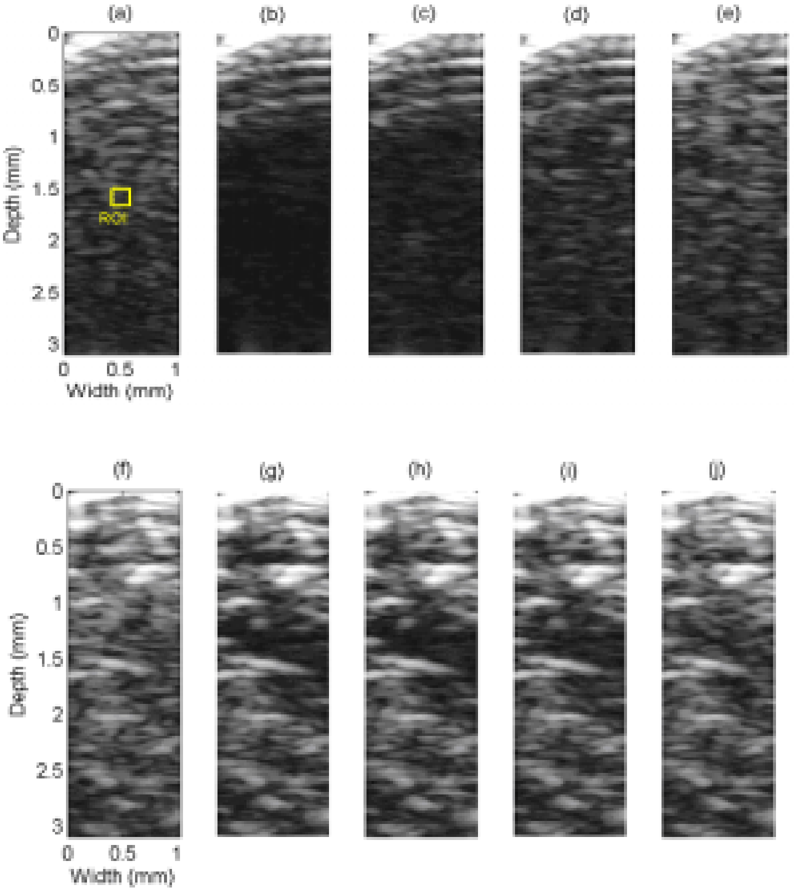

Figure 4.5 Typical destruction/replenishment B-mode images. Without cotton (top) and with cotton (bottom) *in vitro* experiments. (a) and (f) pre-destruction frames, (b)-(e) and (g)-(j) post-destruction images acquired over time. The TIC resulting from the 160 by 160 µm ROI is shown in figure 4.6.

In order to evaluate the effects of parameter estimation strategies on the standard deviation of the estimates of β and $T_{80\%}$, a set of experiments was then conducted at varying flow rates (tables 4.2 and 4.3) using the flow phantom without cotton insert. In order to compute these values, estimates of B (required in equation (4.1)) are based on either the last or average of the last 10 values in the TIC curve or the ITIC curve, and compared with the predicted values (E = 1.18 mm). The range of the fractional standard deviation in these estimates is also computed over 10 flow rates from 30 to 300 mL/hr. Clearly, using the ITIC data to estimate β greatly reduced the standard deviation of the estimates. The standard deviation is also reduced slightly by basing the estimate of B on the last 10 values rather than the last value alone.

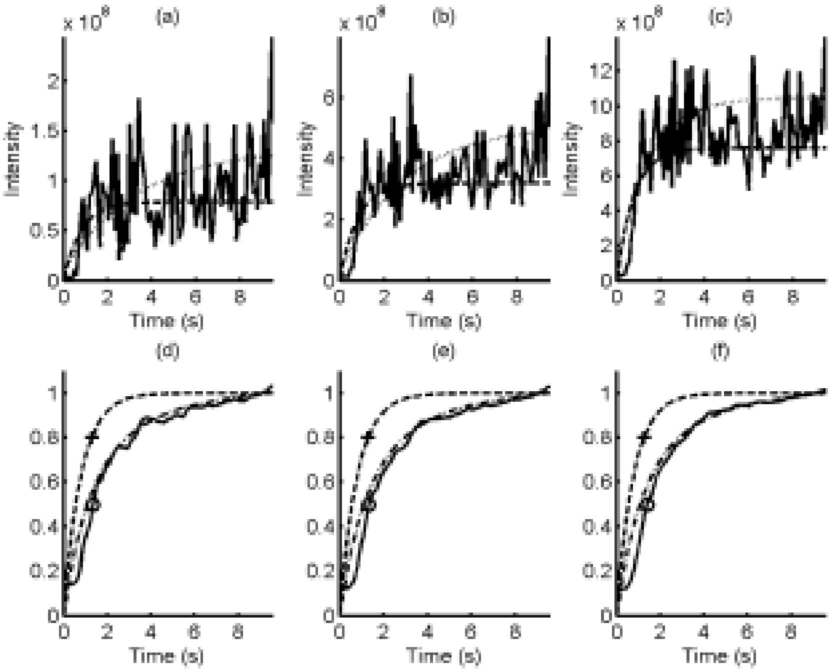

Figure 4.6 Raw TIC (solid), ITIC curve fit (dashed) and TIC curve fit (dotted) with ROI sizes of (a) 160×160 μm (b) 320×320 μm (c) 480×480 μm. Normalized ITIC (solid), normalized ITIC curve fit (dash-dotted) and normalized TIC from ITIC fit (dashed) with ROI sizes of (d) 160×160 μm (e) 320×320 μm (f) 480×480 μm. The symbols "+" and "o" denote the $T_{80\%}$ and $IT_{80\%}$, respectively.

Table 4.2 Estimates of β for *in vitro* images (without cotton) using 160 by 160 μm ROI shown in figure 4.5(a) as a function of flow rate. Standard deviation is computed over all flow rates with the mean fractional standard deviation shown in parentheses.

	60 ml/hr (0.84 mm/sec)	**120 ml/hr (1.68 mm/sec)**	**180 ml/hr (2.52 mm/sec)**	**240 ml/hr (3.36 mm/sec)**	**Fractional STD**
ITIC-B from last 1	0.84 ± 0.18	1.41 ± 0.32	2.32 ± 0.45	2.71 ± 0.68	21-36% (26%)
ITIC-B from last 10	0.89 ± 0.20	1.44 ± 0.31	2.36 ± 0.42	2.71 ± 0.56	14-36% (25%)
TIC-B from last 1	0.42 ± 0.26	0.51 ± 0.78	3.72 ± 1.64	2.80 ± 1.24	44-151% (93%)
TIC-B from last 10	0.53 ± 0.25	0.94 ± 0.63	2.43 ± 0.65	2.46 ± 1.28	10-80% (49%)
Predicted Value $(\beta = \frac{v}{E})$	0.71	1.42	2.14	2.85	

Units: (1/s)

Table 4.3 Estimates of time to achieve 80% replenishment for *in vitro* images (without cotton) using 160 by 160 μm ROI shown in figure 4.5(a) as a function of flow rate. Standard deviation is computed over all flow rates with the mean fractional standard deviation shown in parentheses.

	60 ml/hr (0.84 mm/sec)	**120 ml/hr (1.68 mm/sec)**	**180 ml/hr (2.52 mm/sec)**	**240 ml/hr (3.36 mm/sec)**	**Fractional STD**
	FIT (Search)	**FIT (Search)**	**FIT (Search)**	**FIT (Search)**	
ITIC-B from last 1	1.99 ± 0.40	1.20 ± 0.28	0.73 ± 0.21	0.67 ± 0.17	20-56% (28%)
	(2.39 ± 0.63)	(1.30 ± 0.35)	(0.85 ± 0.22)	(0.71 ± 0.14)	(14-27%) (22%)
ITIC-B from last 10	1.90 ± 0.44	1.16 ± 0.26	0.71 ± 0.17	0.66 ± 0.14	14-59% (27%)
	(2.36 ± 0.63)	(1.29 ± 0.34)	(0.82 ± 0.17)	(0.70 ± 0.14)	(14-27%) (21%)
TIC-B from last 1	3.33 ± 1.08	3.43 ± 1.98	0.80 ± 0.42	0.66 ± 0.26	32-116% (67%)
TIC-B from last 10	3.36 ± 1.19	2.16 ± 0.94	0.67 ± 0.07	0.86 ± 0.58	10-89% (51%)
Predicted Value $(T_{80\%} = \frac{-\ln(0.2)}{\beta})$	2.26	1.13	0.75	0.57	

Units: (s)

Table 4.3 then considers the effect of strategies on the standard deviation of estimating the time to achieve 80% replenishment. Again, both the TIC curves and

ITIC curves are considered as well as the last value or last 10 values in the estimation of B. In addition, the final estimate of the time to 80% is either calculated from β and equation (4.4) (labeled as FIT) or from directly detecting the 80% or 50% value in the pre-fit TIC or ITIC curves, respectively (labeled as Search). Again, the standard deviation of the estimate is greatly reduced using the ITIC data, with the minimum produced with B estimated based on the last 10 values, and the time estimated by searching the ITIC curve for the 50% threshold. All remaining studies estimate B using the average of the last ten values, and the time based on searching the ITIC ($IT_{80\%}$).

To illustrate the spatial variation in estimates of β and $IT_{80\%}$, a two-dimensional map of each parameter was created using a sliding window with dimensions of 160 by 160 μm for a flow rate of 90 mL/hr. Between estimates, the ROI moves with a step size of 16 μm. In addition, a 5 by 5 median filter was used to remove spatially unsupported estimates in the two-dimensional mapping. Figure 4.7 shows the spatial mapping of β and $IT_{80\%}$ estimates, without (figures 4.7(a)) and with cotton (figure 4.7(b)), respectively, and the $IT_{80\%}$ estimates without (figures 4.7(c)) and with cotton (figure 4.7(d)), respectively.

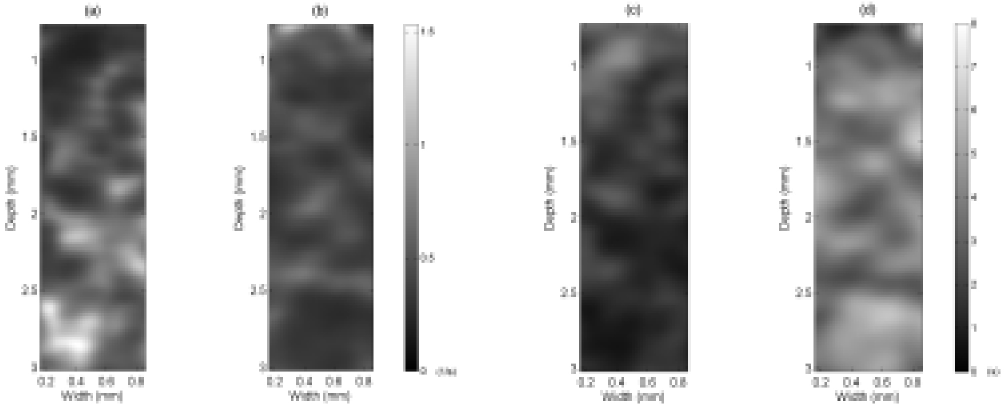

Figure 4.7 Spatial map of the β estimate obtained from scanning the phantom (a) without cotton and (b) with cotton. Spatial map of the two-dimensional $IT_{80\%}$ estimate obtained from scanning the phantom (c) without cotton and (d) with cotton.

To explore the effect of flow rate on these estimates, varying ROI sizes, locations and flow velocities were used in the following experiments. Equation (4.2) predicted a linear relationship between velocity and β estimates, which is explored experimentally in figure 4.8. For each flow rate, five independent measurements were performed to obtain the mean and standard deviation.

Figures 4.8(a) and (b) show the resulting estimates of β without and with cotton, respectively where the 160 by 160 μm ROI is placed at depths of 0.8 mm (dot), 1.6 mm (solid), and 2.4 mm (dash), and compared with the predicted values based on equation 2 (dash-dot). The mean flow rate within the small regions was reduced by the addition of cotton (figure 4.8(b)). A linear regression analysis of the mean β estimate versus flow rate produced a correlation coefficient of 0.96 for the 160 by 160 μm ROI in the center of the phantom.

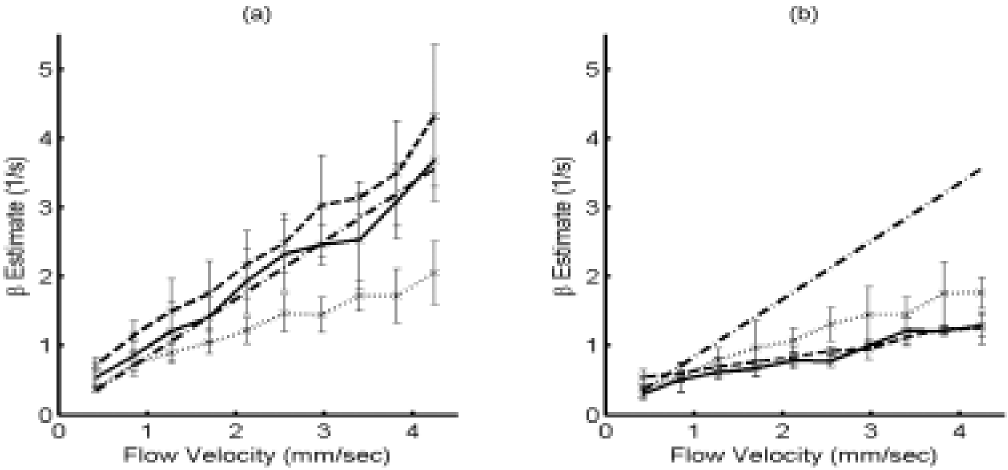

Figure 4.8 β estimates vs. flow velocities with kernel blocks of 160×160 μm (a) without and (b) with cotton where the 160×160 μm ROI is placed at depths of 0.8 mm (dot), 1.6 mm (solid), and 2.4 mm (dash), and compared with the predicted values based on Eq (2) with E = 1.18 mm (dash-dot).

Figures 4.9 (a)-(b) show predicted and experimental $T_{80\%}$ and $IT_{80\%}$ estimates corresponding to data shown in figure 4.8, where (a) and (b) were acquired without and with cotton, respectively. In figures 4.9(a) and (b), the $T_{80\%}$ (dashed) and $IT_{80\%}$ (solid) estimates are shown for the depth of 1.6 mm in the phantom and compared with the predicted values (dash-dot) based on equations (4.2) and (4.4). Mean values are shown as crosses with the error bars corresponding to ± one standard deviation. Without cotton in the phantom and with a small ROI in the center of the phantom, the mean of both $T_{80\%}$ and $IT_{80\%}$ estimates closely approach the predicted values (figure

4.9(a)). When the cotton is added, the flow rate decreases from that predicted for laminar flow, and a difference appears between predicted and experimental estimates for the entire image (figure 4.9(b)).

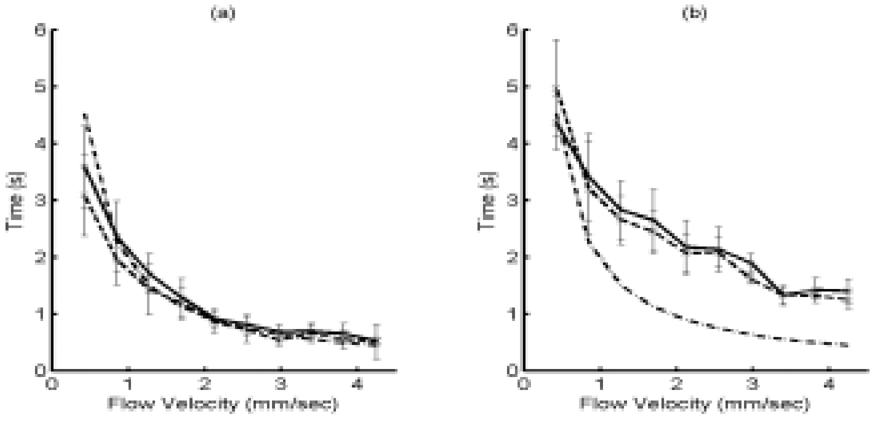

Figure 4.9 $T_{80\%}$ (dashed) and $IT_{80\%}$ (solid) estimates vs. flow velocities and compared with the predicted values (dash-dot). ROI blocks of (a) 160×160 μm at a depth of 1.6 mm in phantom without cotton and (b) 160×160 μm at a depth of 1.6 mm with cotton.

4.6 *In Vivo* Experiments

4.6.1 Animal Protocol

To demonstrate the system's performance for *in vivo* imaging, the highly vascular ciliary body and iris region of the rabbit eye was imaged, according to a protocol approved by the University of California Animal Use and Care Committee. A diagram of this region is shown in figure 4.10(a), where the proximal regions are noted to contain arteries, and the distal end of the ciliary process is dominated by capillaries. A healthy Dutch Belt rabbit was used in the experiment. The rabbit was anesthetized with an intramuscular injection of diazepam at 5 mg/kg followed by 2.5% isoflurane.

The eye was prepared without proptosing using a small speculum to fix the eyelids and ultrasound gel (Aquasonic 100, Parker Laboratories, Inc., Orange, NJ) generously applied to the eye. A 1 mil thick TPX film (Westlake Plastics, Placentia, CA) served as the acoustic window at the bottom of a water bath formed from a Steri-Drape (1020, 3M Medical, St. Paul, MN). The TPX window was placed in contact with the gel, and filled with distilled water. A recent investigation showed that blood flow in the anterior segment is greatly influenced by temperature (Silverman et al 2002). Consequently, the distilled water was maintained at a constant temperature of 40°C using an external water bath, recirculating heater, and heat exchange coil. Once a suitable image of the ciliary body was obtained, a commercially available contrast agent was injected through an ear vein at full concentration using a syringe pump set to 0.5 mL/hr.

(a)

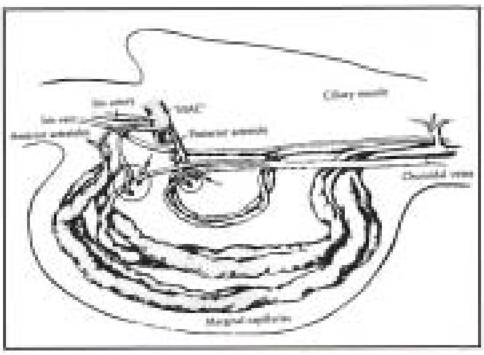

Diagrammatic representation of the anterior segment vasculature. (Reprinted with permission from J. C. Morrison, E. M. V. Buskirk, and T. F. Freddo. Anatomy, microcirculation, an ultrastructure of the ciliary body. In *The Glaucomas*. 2nd Ed. R. Ritch, M. B. Shields, T. Krupin, Eds. St Louis, Mo: CV Mosby Co; 1996.)

(b) (c)

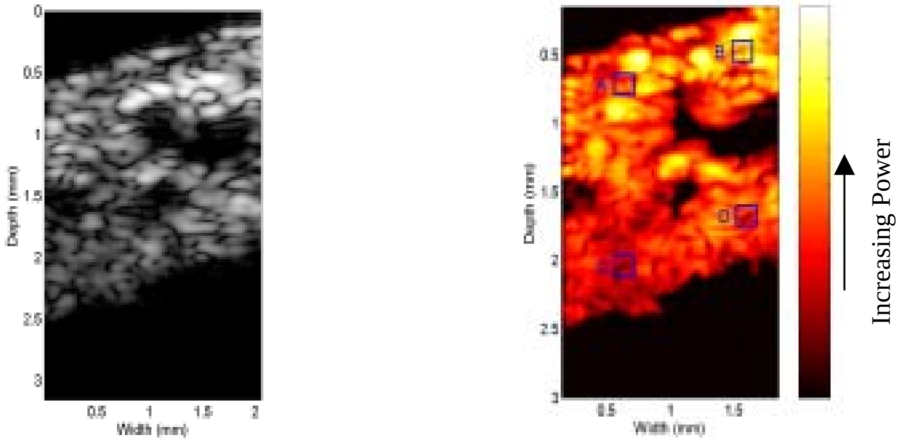

Figure 4.10 *In vivo* experimental data. (a) Diagram of the region to be scanned, (b) B-mode image and (c) spatial map of wall-filtered power integrated over all pulses obtained after bubble destruction. ROIs A-B and C-D are located in iris region and ciliary processes, respectively.

4.6.2 Data Analysis and Results

The region containing the iris and ciliary process was imaged approximately along radial lines extending to the center of the pupil. The RF data were acquired in frames extending 2.04 mm laterally by 3.15 mm in depth at a frame rate of 8.5 fps. A total of 100 frames were acquired. A B-mode image of the rabbit eye with a 40 dB dynamic range is shown in figure 4.10(b). The top section contains the iris and the bottom portion contains the ciliary processes. Image alignment by speckle tracking was applied across frames to reduce the challenging physiologic motion artifacts that are obtained when imaging with a mechanically scanned transducer. To further suppress motion artifacts, a step initialized, 2^{nd} order inverse Chebyshev highpass filter with -30 dB stopband and -1.5 dB passband frequencies of 1.7 Hz and 2.1 Hz, respectively, was applied in the frame index dimension following envelope detection. The filter was first applied in the forward direction and then reapplied in the reverse direction to cancel nonlinear phase distortion.

To map contrast replenishment after bubble destruction, the echo power in each voxel (following the high-pass filter applied across pulses) was summed over the post-destruction frames and is shown in figure 4.10(c). This measure is similar to the integrated area under the time intensity curve (IAUC) in dynamic contrast enhanced (DCE) MRI, and, when normalized by the spatial extent of the voxel, has been shown to be proportional to volume flow in mL/(mg min) in MRI imaging (Simpson et al 1999) as well as in ultrasound (Pollard et al 2002). Within the iris, the power is higher than within the ciliary body, indicating the presence of more contrast, and thus more blood flow. Four ROIs were selected to compare their respective estimates of $IT_{80\%}$, and they are labeled in figure 4.10(c). The ROIs A and B are within the iris, the ROIs C and D are located within the ciliary body.

A ROI of size 160 by 160 μm is translated through the image in figures 4.11(a)-(d), and the quantitative estimates of the replenishment time with different ROI sizes are summarized in table 4.4. In figure 4.11, the "o" denotes the $IT_{80\%}$ estimates, and we note that faster replenishment times in regions A and B in the region expected to be dominated by arteries, and slower times in C and D, expected to be dominated by capillaries. The $IT_{80\%}$ estimates in ROIs A and B ranges from 1.34 to 1.44 s and in ROIs C and D ranges from 4.02 to 4.35 s. ROIs from within the iris include a range of replenishment times expected for arterioles and capillaries. ROIs from the ciliary processes yielded slower perfusion as expected from vascular casts of the microcirculation in this region (Morrison et al 1996).

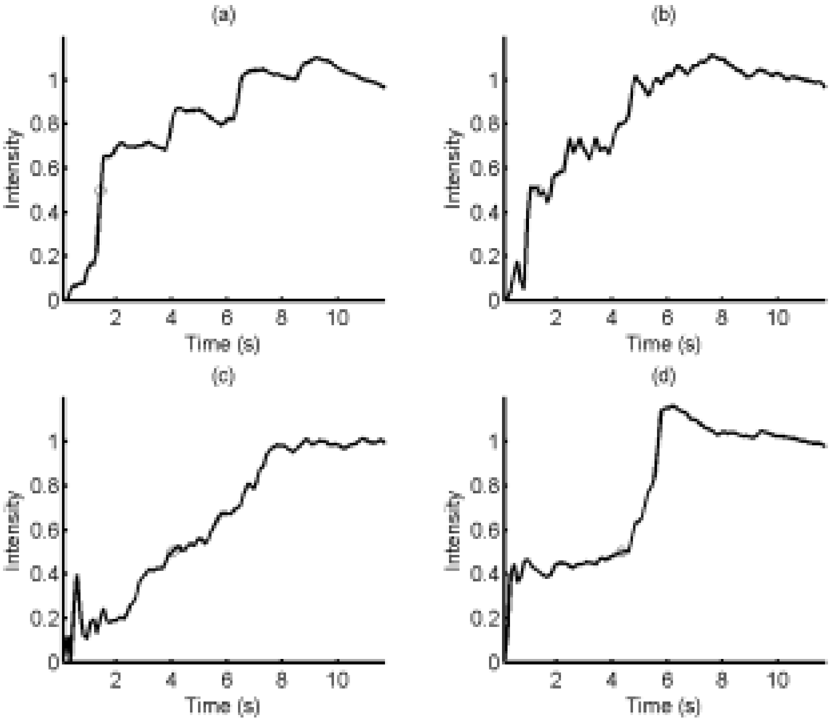

Figure 4.11 Integrated time-intensity curves obtained from regions of interest centered in the locations indicated in figure 4.10, for ROIs A, B, C, and D.

Table 4.4 Summary estimates of time to achieve 80% replenishment ($IT_{80\%}$) within four ROIs *in vivo* experiment.

ROI Size ROI	160 × 160 μm	320 × 320 μm	480 × 480 μm
A	1.44 s	1.49 s	1.50 s
B	1.34 s	0.80 s	0.80 s
C	4.02 s	3.66 s	2.43 s
D	4.35 s	2.21 s	2.68 s

Units: (s)

Figure 4.12 shows a two-dimensional map of $IT_{80\%}$ estimates. The time for replenishment maps offer insight into the distribution of blood velocity within this region. Each $IT_{80\%}$ estimate of the map was obtained from a sliding kernel block of 160 by 160 μm applied across the frames. Note the faster replenishment times in the upper region (iris) compared to the lower left regions (ciliary process).

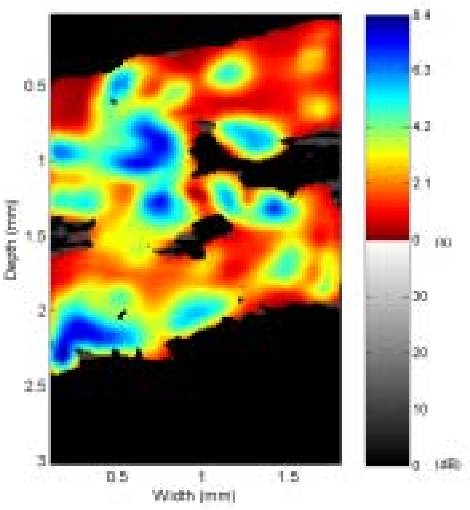

Figure 4.12 Two-dimensional map of $IT_{80\%}$ estimates in the iris and ciliary body.

4.7 Conclusions

In this chapter, we present a new high frequency destruction/replenishment system to assess blood flow in the microcirculation using an ultrasound contrast agent. The unique approaches taken here include the development and testing of an ultrasound system that combines transmission at 1 MHz with transmission at 25 MHz, the use of a new signal integration scheme to reliably estimate microvascular flow in very small regions, and the evaluation of the performance of this system with a new flow phantom. The new flow phantom introduced here is capable of producing very low flow rates and the high clutter to signal ratio found in the microcirculation.

Two parameters, including the rate constant (β) and time to achieve 80% replenishment, were used to estimate flow rates based on wash-in time-intensity measurements. The rate constant can be obtained using a nonlinear least squares fit to an integrated time-intensity model. The estimates of time to achieve 80%

replenishment obtained from time-intensity curves were compared with those obtained from the integrated time-intensity curves. The *in vitro* results showed a good correlation between the actual flow rate and the measured rate constant, thus making quantitative estimation of perfusion feasible. *In vivo* experiments were presented showing blood perfusion in the ciliary body and processes of the rabbit eye. The spatial resolution of the imaging system is 160 by 160 μm. The time to achieve 80% replenishment in the image ranges from 0 to 7.6 seconds. Potential applications of this system include high-resolution flow assessment in small animal tumor and glaucoma models and the evaluation of superficial vasculature in clinical studies.

5. Chapter 5 Discussion and Conclusions

5.1 Doppler Angle Estimation

In chapter 1, we proposed a new approach for Doppler angle estimation that only requires a small number of flow samples. An eighth-order AR model was used to extrapolate the original eight flow samples to 64 flow samples for spectrum estimation. The selection criteria for both the Doppler signal and the model order had a significant effect on the results obtained. The results obtained using simulated and experimental data show that the AR method not only accurately estimated the Doppler bandwidth, it also outperformed the conventional FFT method at small Doppler angles. The main reason is that the data acquisition time required by the AR method is smaller and hence it is less affected by the temporal velocity change. This study shows that real-time two-dimensional Doppler angle estimation is possible.

This study considered constant flows, flows with spatially varying velocity, pulsatile and turbulent flows. In the presence of the turbulent flows, however, the AR method is not suitable to estimate the Doppler angle due to the fact that the Doppler bandwidth is not only affected by the transit time effect, it is also affected by the turbulence. In this study, the experimental results had larger estimation errors than the simulation results. This is possibly due to the difference in SNR. In other words, the lower SNR associated with the experimental data potentially induced more extrapolation errors when the AR method was applied.

In section (2.3.1), performance of the AR method in the constant velocity flows was validated. The spatial velocity gradient associated with a laminar flow had noticeable impact on the estimation results. Errors of the AR method increased with gradient. The AR method had an average estimation error of 3.6^{o} in the experimental data for the Doppler angle ranging from 33^{o} to 72^{o}. For pulsatile flows, the Doppler bandwidth was affected by both the spatial and the temporal velocity changes. The experimental data for the AR method had an average estimation error of 3.5^{o} for Doppler angle range from 30^{o} to 78^{o}. It was found that the spatial velocity change (i.e., gradient) has a bigger impact on Doppler angle estimation than the temporal velocity change (i.e., pulsation) with the AR method. However, the FFT method is significantly affected by both the spatial and temporal velocity changes. For the FFT method, the average estimation errors for constant flows and for pulsatile flows were 4.7° and 6.87°, respectively.

Finally, results indicate that real-time two-dimensional Doppler angle estimation using the AR method in the presence of pulsatile flows is feasible. Although the computational complexity associated with the AR method is more demanding than that with the conventional FFT method, such computational requirements can be adequately met and do not affect the two-dimensional imaging frame rate (Schlindwein and Evans 1989).

5.2 Contrast-Specific Flow Estimation

5.2.1 Feasibility of Using Deconvolution Technique

The hypothesis that mixing of the contrast agent is a LTI process was tested in section (3.4). Such a study is critical in determining if deconvolution techniques can be applied for quantitative blood flow estimation. Results indicated that although the backscattered intensity increased with the concentration of the contrast agent, the measured MTT's also varied as the concentration varied.

In addition, the MTT's of the mixing chamber derived based on equation (3.5) were different from the MTT's obtained based on equation (3.4). Therefore, it is concluded that the mixing process is generally not LTI and deconvolution techniques cannot be applied for measuring the absolute flow rate. Moreover, table 3.1 showed that the MTT estimates were affected by both the volume of the mixing chamber and the flow rate. In general, the MTT estimates were closest to the theory with a smaller mixing chamber and at a higher flow rate. Although deconvolution techniques are generally not applicable, results in figures 3.12 to 3.14 showed that a linear relationship was still present between the measured MTT values and theoretical MTT values. Thus, time-intensity based methods are still feasible if only relative flow analysis is required.

In another study of this research project, the compartment flow phantom was placed both vertically and horizontally. Results showed that both configurations produced good relative estimates of flow parameters. Hence, influence of microbubbles buoyancy can be ignored when the larger diameter self-made agent was used.

Only constant flows were considered in chapter 3. In practice, pulsatile flows are present and the flow rate changes with time and the mixing process becomes time varying. In this case, Li and Yang (2003) proposed deconvolution techniques based on the ensemble method, the cross-correlation method and the recursive least-squares method for time-varying transfer function analysis. Results indicate that the pulsation generally does not affect the validity of time-intensity based flow estimation. The proposed RLS deconvolution technique is effective for both constant and pulsatile flows, thus permitting transfer function analysis in various flow conditions.

5.2.2 Shadowing Effect and IOTIC Technique

Section (3.5.2) discussed the shadowing effect that occurs when a contrast agent passes through a perfused region. Since the TIC measured within the perfused area is affected by the shadowing effect, it is not a reliable method for deriving flow parameters. The shadowing effect depends on the concentration of the contrast agent. In clinical conditions, it may also occur in a heart chambers or a blood vessel (Goldberg 1997). It has been shown that the shadowing effect may limit penetration of the ultrasound beam and affect visualization of myocardial layers in contrast echocardiography (Bos et al 1996; Kaul et al 1992). The new IOTIC technique monitors the signal enhancement at both the input and the output of a perfused region. Although all the three TICs may potentially be affected, the shadowing effect is less significant on the inflow and the outflow TICs because it can be minimized with a lower microbubble concentration.

It has been shown that several flow parameters obtained from the IOTIC technique are more linearly related to the flow rate than those obtained from the TIC measured directly from the perfused area. These results indicate that the IOTIC technique can replace direct measurement methods. The IOTIC technique provides several advantages: (i) it does not require assumptions regarding the input concentration curve, (ii) it is less affected by the shadowing effect, and (iii) the difficulties associated with gaining acoustic access to certain perfused areas (e.g., brain tissue) can be avoided.

5.3 Microbibbles Destruction/Reperfusion System

The ultrasound technique described in chapter 4 can be used to create high resolution maps of the time required for contrast replenishment in regions as small as 160 by 160 microns. In order to characterize the system, the pressure required for microbubble destruction was evaluated first through acoustic experiments and found to be approximately 0.52 MPa, in agreement with previous studies. When a small ROI in the center was selected, the estimates of the flow parameter β obtained for a flow phantom were unbiased and increased linearly in proportion to increases in the input flow rate. For *in vitro* imaging in a small chamber, for which the flow velocity is nearly constant across the ROI, the standard deviation of the estimated replenishment parameters increases from 9 to 21% when the ROI is decreased from the whole image to 160 by 160 μm, respectively.

A new method for estimating the time to 80% contrast replenishment was introduced. The TIC curve is integrated over time for each ROI and the time required for the integrated amplitude to reach one half of the maximum value is estimated. With this method, the time to 80% contrast replenishment could be estimated in a few seconds, and the average standard deviation of estimates of β and the $IT_{80\%}$ in the small volume of 160 by 160 μm were substantially reduced to a low of 21%.

The phantom described here can be used without a cotton insert to produce calibrated and low variance estimates of flow rate. With the addition of the cotton insert, the flow rate decreased and flow became more uniform over depth. Cotton also provides a clutter source in order to test wall filter and estimation strategies. This phantom can be used for calibration experiments in the development of new ultrasound systems.

The estimates of flow obtained within the iris ciliary body correspond with the values expected for regions dominated by arteries or capillaries. Thus, while our *in vitro* studies indicate that increasing the ROI decreases the estimate variance for a region with a constant flow velocity, we find *in vivo* that increasing the ROI would result in a loss of information about the spatial and temporal variation in the flow characteristics.

The iris and ciliary body are regions that are often the focus for blood flow reduction therapies associated with glaucoma. The goal is to reduce aqueous fluid production by decreasing blood flow within this region. Due to the unique geometry of the iris and ciliary processes, flow is more predictable in angle and velocity as compared to other tissues. The ciliary processes are thin structures with constrained flow, and are dominated by arteries near their junction with the iris and by capillaries as they approach the anterior chamber of the eye. This therefore is a clinically relevant and well-characterized setting in which to evaluate this new flow mapping system.

Given that the flow within this region is constrained, it is possible that the destruction of the contrast agent using the planar focus of our 1 MHz transducer will result in a delay for the contrast agent as it travels from the arteries in the iris to the ciliary body. Thus, the delay in any small sample volume does not represent just the delay in refilling this one small region, but instead includes travel time through the plane within which the contrast agent was destroyed. Future studies can compare the delay estimated following microbubble destruction along a single line of sight with the delay estimated following microbubble destruction in an entire plane. The image as shown in figure 4.12 shows rapid replenishment in a region of the iris, with an apparent increase in delay in the surrounding regions.

5.3.1 Limitation of this System

The technology currently available for high frequency ultrasound has limited studies such as ours. While ultrasound imaging at the lower frequencies typically used in clinical studies is performed with arrays of elements that allow for electronic steering, such arrays have not yet been developed for commercial purposes for frequencies above 17 MHz. Without electronic beam-steering, the transducer or an acoustic mirror must be mechanically scanned, and any positional or velocity errors in this scanning will greatly degrade the TIC and resulting estimated parameters. In addition, each individual ultrasound transducer typically has a fractional bandwidth on the order of 100%, and therefore one transducer cannot provide both the low frequency destructive and high frequency imaging pulse. Combined transducers with multiple center frequencies are under consideration or being developed for several applications, however, and are likely to become available over the next few years.

Another limitation of this study is the use of a wall-filter to remove the fixed and slowly moving tissue component. While using the combination of the 1 MHz and 25 MHz transducer for destruction and replenishment, we were unable to take advantage of the nonlinear oscillation of contrast agent microbubbles in order to separate the microbubble and tissue echoes. There have been reports of harmonic or subharmonic oscillations of contrast agents when insonified at high frequencies, however, these components are small and require relatively long pulse lengths and high pressures to excite. The application of the wall-filter could have removed some echoes from very slowly moving contrast agents, however, our predicted replenishment times agree with previous observations of intravital microscopy, and other ultrasound studies by our group at lower frequencies for which the wall-filter was not required.

5.3.2 Comparisons of Flow Estimation with MRI, CT and PET

The ultrasound technique proposed here has substantial advantages for the estimation of local blood velocity and potentially volume flow, compared to MR, CT, and PET. First, ultrasound contrast agents are a purely intravascular tracer, and therefore compartmental analysis is not required. Second, it provides a direct measurement of blood flow, volume, and local velocity, rather than indirect measures. Third, since routine examinations likely to become a part of clinical cancer management, it will be important to minimize cost. Fourth, using this destruction-replenishment scheme, flow velocity can be repeatedly measured and the variance of the estimator can be reduced. This is not possible with MR and CT contrast agents, even with macromolecular agents.

Many MR-based techniques to assess blood flow have been explored including those that assess flow, vascular permeability, and vascular maturity (Neeman et al 2001). Spin-tagging techniques (Roberts et al 1995; Silva et al 2000) have been used to assess microvascular flow, including flow in tumors, although ultrasound as described here may improve spatial resolution, assess very slow flow (not limited by relaxation times), and assess purely intravascular flow. The development of macromolecular MR contrast agents has been necessary to reduce the diffusion of the contrast agent out of the vasculature, a condition that is not a limitation in ultrasound since ultrasound contrast agents do not diffuse through endothelial fenestrations. DCE MRI has been used to measure the effect of an angiogenesis inhibitor (Taylor et al 1999), however resolution on the order of 100 microns has not been reported in a clinically-applicable technique.

Alternative flow estimation techniques for small vessels also include laser Doppler flowmeters and fluorescein angiography (Williamson and Harris 1994; Giovagnorio et al 1993; Ho et al 1992; Flaharty et al 1991; Michelson et al 1990; Prunte et al 1995). Laser Doppler flowmetry is limited to superficial layers, requires averaging over significant time intervals to produce a reliable estimate, must be calibrated, and does not provide sufficient resolution in the range dimension. Also, since signals resulting from arterioles are not easily differentiated from those resulting from capillaries, the interpretation of resulting measurements must be made cautiously. Fluorescein angiography (FA) and other angiographic methods can be used to estimate the architecture and dilution rate in vessels that can be visualized optically. The acquisition of a time series of angiograms over a period of seconds can be used to estimate the time for wash-in and wash-out of the dye. However, estimation of velocity over the cardiac cycle cannot be performed with fluorescein angiography and FA cannot be employed within the ciliary body or within the optic nerve head.

6. Chapter 6 Future Works

6.1 Doppler Angle estimation

From the results of Chapter 1, it is concluded that real-time two-dimensional estimation of the Doppler angle is possible using the AR method in the presence of pulsatile flows. Future work will extend the AR method to *in vivo* experiments and take into account the influence of physiological motion artifacts. Since accurate estimates can be obtained using a limited number of flow samples, the Doppler angle estimated by AR method is less affected by physiological motion artifact.

6.2 Applications of IOTIC Technique

In Section (3.5.1), we proposed the IOTIC technique to estimate perfusion blood flow. Future work includes the applications of the IOTIC technique to the kidney and the extracranial brain perfusion assessment. First, the IOTIC can be applied in renal perfusion assessment by measuring the TICs from the renal artery and the renal vein, assuming the loss of microbubbles through the urine metabolism can be ignored. The measured perfusion can be used as an index for the kidney functions after a transplant. Second, the time–intensity relationships can be measured both in a carotid artery and an internal jugular vein to assess brain perfusion.

6.2.1 Multi-Input and Multi-Output System

Consider a simple perfusion flow system shown in figure 6.1 with a single inflow orifice P (e.g., the common carotid artery), and a single outflow orifice O (e.g., the cardinal vein). The inflow orifice P divides into a number of branches, one of which is P' (e.g., the internal or external carotid artery) and they continue to divide and terminate at capillaries. Outflow channels coadunate progressively, one of them being represented by O' (e.g., the internal jugular vein) and finally all venous drainage flows out through the single channel O (Meier and Zierler 1954). The application of the IOTIC method in this case implies measurements of the time intensities from the internal carotid artery and the internal jugular vein, since the two vessels can be monitored simultaneously using conventional grayscale imaging. Thus, the simple single-input–single-output model adopted in this study needs to be replaced with a multiple-input–multiple-output model.

Further analysis of multiple input multiple output systems is necessary, although if it is assumed that the concentration curve is essentially the same for all output branches (i.e., the fraction of the total flow leaving through any output channel is proportional to the flow rate in that channel, and the shape of the concentration curve is the same for all output branches), equation (3.9) will still be valid for flow and volume calculations. The perfusion flow assessments using IOTIC will be correlated with the results from the direct measurement method.

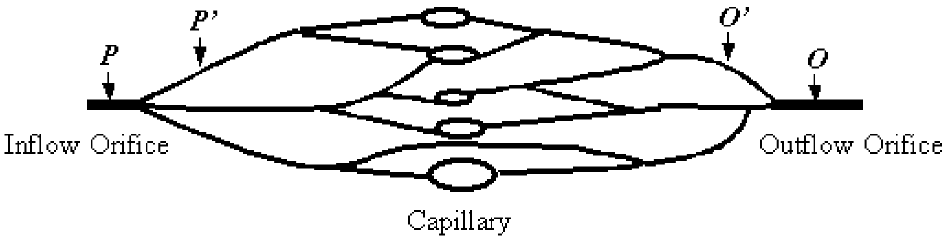

Figure 6.1 A schematic diagram of the flow system model with multiple inputs and multiple outputs.

6.3 Microbubbles Destruction/Reperfusion System

One important application of this new bubble destruction/reperfusion technique is to evaluate the effect of vasoactive drugs used for cardiovascular indications or as ophthalmic therapies. Glaucoma drug therapies include α-agonists (apraclonidine and brimonidine), β-adrenergic receptor blocking agents, prostoglandin-based agents (Morsman et al 1995; Nicolela et al 1996; Stewart and Castelli 1996; Stewart and Garrison 1998). The effects of these drugs on blood flow within the eye are expected to vary greatly, but assessment of their impact has been difficult due to the lack of imaging tools with sufficient spatial and velocity resolution. Development of the capability to quantitatively assess flow in each small region within the eye could have significant impact on current clinical management, and on the integration of the many new glaucoma drugs currently under development. It is critical to decrease intraocular pressure without decreasing perfusion of the optic nerve head. It is known that the density of α and β-adrenergic receptors varies within the eye, even within the anterior segment.

Wax and Molinoff (1987) found that the density of β-adrenergic receptors in the iris was significantly higher than in the ciliary body. β–adrenergic receptor blocking agents decrease blood flow (presumably with the exception of the β_1 selective antagonist betaxodol). Latanoprost (prostoglandin F2α) is now widely used but has varying vascular effects including a vasoconstrictive effect in the human eye. The new technique described here can be used to better characterize these effects.

References

Anderson ME, “Multi-dimensional velocity estimation with ultrasound using spatial quadrature,” *IEEE Trans. Ultrason. Ferroelect. Freq. Contr.*, vol. 45, pp. 852-861, 1998.

Aristizabal O, Christopher DA, Foster FS, and Turnball DH, “Measuring blood flow in the mouse embryo,” *in Proc. IEEE Ultrason. Symp.*, vol. 2, pp. 1489-1492, 1997.

Axel L, “Cerebral blood flow determination by rapid-sequence computed tomography: theoretical analysis,” *Neuroradiology*, vol. 137, pp. 679-686, 1980.

Azimi M, and Kak AC, “An analytical study of Doppler ultrasound systems,” *Ultrasonic Imaging*, vol. 7, pp. 1-48, 1985.

Baker DW, “Pulsed ultrasonic Doppler blood-flow sensing”, *IEEE Transactions on Sonics and Ultrasonics*, vol. 3, pp. 170-85, July 1970.

Bascom PAJ, Cobbold RSC, Routh HF, and Johnston KW, “On the Doppler signal from a steady flow asymmetrical stenosis model: effects of turbulence,” *Ultrasound Med. Biol.*, vol. 19, pp. 197-210, 1993.

Bates JH, “Deconvolution of tracer and dilution data using the Wiener filter,” *IEEE Trans. on Biomed. Eng.*, vol. 38, pp. 1262-1266, 1991.

Becher H and Burns PN, “Handbook of contrast echocardiography,” *Springer Verlag*, Frankfurt and New York, June 2000.

Bohs LN, Friemel BH, and Trahey GE, “Experimental velocity profiles and volume flow via two-dimensional speckle tracking,” *Ultrasound Med. Biol.*, vol. 21, pp. 885-898, 1995.

Bohs LN, Geiman BJ, Anderson ME, Breit SM, and Trahey GE, “Ensemble tracking for 2D vector velocity measurement: experimental and initial clinical results,” *IEEE Trans. Ultrason. Ferroelect. Freq. Contr.*, vol. 45, pp. 912-924, 1998.

Bos LJ, Piek JJ, and Spaan JA, “Effects of shadowing on the time-intensity curves in contrast echocardiography: a phantom study,” *Ultrasound Med Biol.*, vol. 22, pp. 217-227, 1996.

Chen X, Schwarz K, Phillips D, Steinmetz SD, and Schlief R, “A mathematical model for the assessment of hemodynamic parameters using quantitative contrast echocardiography,” *IEEE Trans. on Biomed. Eng.*, vol. 45, pp.

754-765, 1998.

Chomas JE, “Contrast-assisted ultrasound perfusion estimation,” PhD dissertation, Biomedical Engineering, University of Virginia, 2001.

Chomas JE, Dayton P, Allen J, Morgan K, and Ferrera KW, “Mechanisms of contrast agent destruction,” *IEEE Trans. Ultrason. Ferroelect. Freq. Contr.*, vol. 48, no. 1, pp. 232-248, 2001.

Chomas JE, Dayton P, May D, and Ferrara KW, “Threshold of fragmentation for ultrasonic contrast agent,” *J. Biomed. Opt.*, vol. 6, no. 2, pp. 141-150, 2001.

Chomas JE, Dayton P, May D, Allen J, Klibanov A, and Ferrara K, “Optical observation of contrast agent destruction,” *Appl. Phys. Lett.*, vol. 77, no. 7, pp. 1056-1058, 2000.

Chomas JE, Pollard R, Wisner E, and Ferrara K, “Subharmonic phase-inversion for tumor perfusion estimation,” *in Proc. IEEE Ultrason. Symp.*, vol. 2, pp. 1713-1716, 2001

Claassen L, Seidel G, and Algermissen C, “Quantification of flow rates using harmonic gray-scale imaging and an ultrasonic contrast agent: an *in vitro* and *in vivo* study,” *Ultrasound Med. Biol.*, vol. 27, pp. 83-88, 2001.

Cloutier G, Chen D, and Durand LG, “Performance of time-frequency representation techniques to measure blood flow turbulence with pulsed-wave Doppler ultrasound,” *Ultrasound Med. Biol.*, vol. 27, pp. 535-550, 2001.

Cooney DO, “Biomedical engineering principles: an introduction to fluid, heat and mass transport processes,” New York: M. Dekker, 1976.

David JY, Giddens SA, and Giddens DP, “Modern spectral analysis techniques for blood flow velocity and spectral measurements with pulsed Doppler ultrasound,” *IEEE Trans. Biomed. Eng.*, vol. 38, no. 6, pp. 589-596, 1991.

Dayton PA, Morgan KE, Klibanov AL, Brandenburger G, Nightingale KR, and Ferrara KW, “A preliminary evaluation of the effects of primary and secondary radiation forces on acoustic contrast agents,” *IEEE Trans. Ultrason. Ferroelect. Freq. Contr.*, vol. 44, no. 6, pp. 1264-1277, 1997.

D‘Sa A, “Acoustic densitometry-white paper,” Hewlett Packard. Boeblingen, Germany: Agilent Technologies, 1999.

Eigler NL, Pfaff JM, Zeiher A, Whiting JS, and Forrester JS, “Digital angiographic impulse response analysis of regional myocardial perfusion: linearity, reproducibility, accuracy, and comparison with conventional indicator dilution curve parameters in phantom and canine models," *Circ. Res. 64*, pp. 853-66, 1989.

Evans DH, "Some aspects of the relationship between instantaneous volumetric blood flow and continuous wave Doppler ultrasound recordings III," *Ultrasound Med. Biol.*, vol. 9, pp. 617-623, 1982.

Flaharty P, Lieb W, Sergott R, Bosley T, and Savino P, "Color Doppler imaging. A new noninvasive technique to diagnose and monitor carotid cavernous sinus fistulas," *Arch. Ophthalmol.*, vol. 109, no. 4, pp. 522-526, 1991.

Fred SG, "Basic concepts in the determination of vascular volumes by indicator-dilution methods," *Circ. Res. X*, pp. 429-446, 1962.

Giovagnorio F, Quaranto L, and Bucci M, "Color Doppler assessment of normal ocular blood flow," *J. Ultras. Med.*, vol. 12, no. 8, pp. 473-477, 1993

Gobbel GT, and Fike JR, "A deconvolution method for evaluating indicator-dilution curves," *Phys. Med. Biol.*, vol. 39, pp. 1833-1854, 1994.

Goertz DE, Christopher DA, Yu JL, Kerbel RS, Burns PN, and Foster FS," High-frequency color flow imaging of the microcirculation," *Ultrasound Med. Biol.*, vol. 26, no. 1, pp. 63-71, 2000.

Goertz DE, Yu JL, Kerbel RS, Burns PN, and Foster FS, "High-frequency Doppler ultrasound monitors the effects of antivascular therapy on tumor blood flow," *Cancer Res.*, vol. 62, no. 22, pp. 6371-6375, 2002

Goldberg BB, "Ultrasound contrast agents, "*Dunitz ltd. London. Chapter3*, 1997.

Gramiak R and Shah PM, "Echocardography of the aortic root*," Invest. Radiol.*, vol. 3, pp. 356-388, 1968.

Haifeng W, Ritter T, Wenwu C, and Shung KK, "High frequency properties of passive materials for ultrasonic transducers," *IEEE Trans. Ultrason. Ferroelect. Freq. Contr.*, vol. 48, no. 1, pp. 78-84, 2001.

Heidenreich PA, Wiencek JG, Zaroff JG, Aronson S, Segil LJ, Harper PV, and Feinstein SB, "*In vitro* calculation of flow by use of contrast ultrasonography," *J. Am. Soc. Echoc.*, vol. 6, pp. 51-61, 1993.

Hein IA, "3-D flow velocity vector estimation with a triple-beam lens transducer experimental results," *IEEE Trans. Ultrason. Ferroelect. Freq. Contr.*, vol. 44, pp. 85-89, 1997.

Hindle AJ, and Perkins AC, "A perfusion phantom for the evaluation of ultrasound contrast agent," *Ultrasound Med. Biol.*, vol. 20, pp. 309-314, 1994.

Ho A, Lieb W, Flaharty P, Sergott R, Brown G, Bosley T, and Savino P, "Color Doppler imaging of the ocular ischemic syndrome," *Ophthalmology*, vol. 99, no. 9, pp. 1453-1462, 1992.

Jain RK, "Determinants of tumor blood flow: A review," *Cancer Research*, vol. 48, 2641-2658, May, 1988.

Jensen JA, "Estimation of blood velocity using ultrasound: A signal processing approach," New York: Cambridge University Press, 1996.

Jensen JA, "A new estimator for vector velocity estimation," *IEEE Trans. Ultrason. Ferroelect. Freq. Contr.*, vol. 48, pp. 886-894, 2001.

Jones SA and Giddens DP, "A simulation of transit time effects in Doppler ultrasound signals," *Ultrasound Med. Biol.*, vol. 16, no. 6, pp. 607-619, 1990.

Kaluzynski K, "Analysis of application possibility of autoregressive modelling to Doppler blood flow signal spectral analysis," *Med. Biol. Eng. Comput.*, vol. 25, no. 4, pp. 373-376, 1987.

Kaluzynski K, "Order selection in Doppler blood flow signal spectral analysis using autoregressive modeling," *Med. Biol. Eng. Comput.*, vol. 27, no. 1, pp. 89-92, 1989.

Kasai C, Namekawa K, Koyano A, and Omoto R, "Real-time two dimensional blood flow imaging using an autocorrelation technique," *IEEE Trans. Sonics Ultrason.*, vol. 32, no. 3, pp. 458-464, 1985.

Kaul S, Jayaweera A, Glasheen WP, Villanueva FS, and Gutgesell HP, "Myocardial contrast echocardiography and transmural distribution of flow: a critical appraisal during myocardial ischemia not associated with infarction," *J. Am. Coll. Cardiol.*, vol. 20 pp. 1005-016, 1992.Kay SM, "Modern spectral estimation: Theory and application. Englewood Cliffs," NJ: Prentice Hall, 1988.

Keeton PI, Schlindwein FS, and Evans DH, "A study of the spectral broadening of simulated Doppler signals using FFT and AR modelling," *Ultrasound Med. Biol.*, vol. 23, no. 7, pp. 1033-1045, 1997.

Kerr AT, and Hunt JW, "A method for computer simulation of ultrasound Doppler color flow images – I. Theory and numerical method," *Ultrasound Med. Biol.*, vol. 18, no. 10, pp. 861-872, 1992.

Kerr AT, and Hunt JW, "A method for computer simulation of ultrasound Doppler color flow images – II. Simulation results," *Ultrasound Med. Biol.*, vol. 18, no. 10, pp. 873-879, 1992.

Kruse DE, and Ferrara KW, "A new high resolution color flow system using an eigendecomposition-based adaptive filter for clutter rejection," *IEEE Trans. Ultrason. Ferroelect. Freq. Contr.*, vol. 49, no. 12, pp. 1739-1754, 2002.

Kruse DE, Lim MC, Redline DE, Eisele PE, and Ferrara KW, "High frequency ultrasound with an eigen-decomposition filter to assess the effect of laser cyclophotocoagulation treatment on blood flow," *in Proc. IEEE Ultrason. Symp.*, vol. 2, pp. 1485-1489, 2002.

Kruse DE, Silverman R, Erickson S, Coleman DJ, and Ferrara KW, "Optimization of real-time high frequency ultrasound for blood flow imaging in the microcirculation," *in Proc. IEEE Ultrason. Symp.*, vol. 2, pp. 1461–1464, 2000.

Kruse DE, Silverman RH, Fornaris RJ, Coleman DJ, and Ferrara KW, "A swept-scanning mode for estimation of blood velocity in the microvasculature," *IEEE Trans. Ultrason. Ferroelect. Freq. Contr.*, vol. 45, no. 6, pp. 1437-1440, 1998.

Lee BR, Chiang HK, Kuo CD, Lin WL, and Lee SK, "Doppler angle and flow velocity estimations using the classic and transverse Doppler effects," *IEEE Trans. Ultrason., Ferroelect., Freq. Contr.*, vol. 46, no. 1, pp. 252-256, 1999.

Lee BR, Chiang HK, Chou YH, Kuo CD, Wang JH, and Lee SK, "Implementation of spectral width Doppler in pulsatile flow measurements," *Ultrasound Med. Biol.*, vol. 25, pp. 1221-1227, 1999.

Li PC, "Principles of Medical Ultrasound," Class Notes, National Taiwan University, 2000.

Li PC, Cheng CJ, and Shen CC, "Doppler angle estimation using correlation," *IEEE Trans. Ultrason. Ferroelect. Freq. Contr.*, vol. 47, pp. 188-196, 2000.

Li PC, Yeh CK, and Wang SW, "Time-intensity-based volumetric flow measurements: an in vitro study," *Ultrasound Med. Biol.* vol. 28, no. 3, pp. 349–358, 2002.

Li PC and Yang MJ, "Transfer function analysis of ultrasonic time-intensity measurements," *Ultrasound Med. Biol.* vol. 29, no. 10, pp. 1493-1500, 2003.

Lauterborn W, "Numerical investigation of nonlinear oscillations of gas bubbles in liquids," *J.* Acoustical *Society. Am.,* vol. 59, no. 2, pp. 283-93, 1976.

Lotsberg O, Hovem JM, and Askum B, “Experimental observation of subharmonic oscillations in infoson bubbles,” *J. Acoust. Soc. Am.*, vol. 99, no. 3, pp. 1366-1369, 1996.

Marasek K, and Nowicki A, “Comparison of the performance of 3 maximum Doppler frequency estimators coupled with different spectral estimation methods,” *Ultrasound Med. Biol.*, vol. 20, pp. 629-638, 1994.

Meier P, and Zierler KL, “On the theory of the indicator-dilution method for measurement of blood flow and volume,” *J. appl. physiol.*, vol. 6 pp. 731-744, 1954.

Michelson G, Gierth K, Priem R, and Laumer R, “Blood velocity in the ophthalmic artery in normal subjects and patients with endophthalmitis,” *Invest. Ophthalmol. Vis. Sci.*, vol. 31, no. 9, pp. 1919-1923, 1990.

Miles K, Dawson P, and Blomley M, “Functional computed tomography. Oxford, UK: Isis Medical Media,” *Oxford University Press*, pp. 49-51, 1997.

Mor-Avi V, Akselrod S, David D, Keselbrener L, and Bitton Y, “Myocardial transit time of the echocardiographic contrast media,” *Ultrasound Med. Biol.*, vol. 19, pp. 635-648, 1993.

Morrison JC, Van Buskirk EM, and Freddo TF, “Anatomy, microcirculation, an ultrastructure of the ciliary body.” in *The Glaucomas*, 2nd Ed., R. Ritch, M. B. Shields, and T. Krupin, Ed. St Louis: CV Mosby Co, 1996.

Morsman CD, Bosem ME, Lusky M, and Weinreb RN, “The effects of topical beta-adrenoceptor blocking agents on pulsatile ocular blood flow,” *Eye*, vol. 9, pp. 344-347, 1995.

Nanda NC, Schlief R, and Goldberg B, “Advances in echo imaging using contrast enhancement,” Dordrecht Boston: Kluwer Academic Publishers, 1997.

Navin CN, and Reinhard S, “Advances in echo imaging contrast enhancement,” *Kluwer Academic Publishers. Chapter3*, pp. 43-56, 1993.

Neeman M, Provenzale LM, and Dewhirst MW, “Magnetic resonance imaging applications in the evaluation of tumor angiogenesis,” *Semin. Radiat. Oncol.*, vol. 11, no. 1, pp. 70-82, 2001.

Newhouse VL, Censor D, Vontz T, Cisneros JA, and Goldberg BB, “Ultrasound Doppler probing of flows transverse with respect to beam axis,” *IEEE Trans. Biomed. Eng.*, vol. 34, no. 10, pp. 779-789, 1987.

Newhouse VL, Furgason ES, Johnson GF, and Wolf DA, “The dependence of ultrasound bandwidth on beam geometry," *IEEE Trans. Sonics Ultrason.*, vol. 27, no. 2, pp. 50-59, 1980.

Nicolela MT, Buckley AR, Walman BE, and Drance SM, "A comparative study of the effects of timolol and latanoprost on blood flow velocity of the retrobulbar vessels," *Am. J. Ophthalmol.*, vol. 122, no. 6, pp. 784-789, 1996.

Newhouse VL, Censor D, Vontz T, Cisneros JA, and Goldberg BB, "Ultrasound Doppler probing of flows transverse with respect to beam axis," *IEEE Trans. Biomed. Eng.*, vol. 34, pp. 779-789, 1987.

Ostrander L, Lee B, Silverman D, and Groskopf RW, "A compartment model for fluorometric indication of tissue perfusion," *IEEE Trans. on Biomed. Eng.*, vol. 37, pp. 1017-1023, 1990.

Pavlin CJ, and Foster FS, "Ultrasound biomicroscopy. High-frequency ultrasound imaging of the eye at microscopic resolution," *Radiol. Clin. North Am.*, vol. 36, no. 6, pp. 1047-1058, 1998.

Pollard R, Sadlowski A, Bloch S, Murray L, Wisner E, Griffey S, and Ferrara K, "Contrast-assisted destruction-replenishment ultrasound for the assessment of tumor microvasculature in a rat model," *J. Technol. Cancer Resear. Treat.*, vol. 1, no. 6, pp. 459-470, 2002.

Postert T, Hoppe P, Federlein J, Helbeck S, Ermert H, Przuntek H, Buttner T, and Wilkening W, "Contrast agent specific imaging modes for the ultrasonic assessment of parenchymal cerebral echo contrast enhancement," *J. Cereb. Blood Flow Metab.*, vol. 20 pp. 1709-1716, 2000.

Prunte C, Flammer J, Markstein R, and Rudin M, "Quantification of optic nerve blood flow changes using magnetic resonance imaging," *Invest. Ophthalmol. Vis. Sci.*, vol. 36, no. 1, pp. 247-251, 1995.

Ramnarine KV, Nassiri DK, Hoskins PR, and Lubbers J, "Validation of a new blood-mimicking fluid for use in Doppler flow test objects," *Ultrasound Med. Biol.*, vol. 24, no. 3, pp. 451-459, 1998.

Roberts DA, Detre JA, Bolinger L, Insko EK, Lenkinski RE, Pentecost MJ, and Leuigh JS, "Renal perfusion in humans: MR imaging with spin tagging of arterial water," *Radiology*, vol. 196, no. 1, pp. 281-286, 1995.

Schlindwein FS, and Evans DH, "A real-time autoregressive spectrum analyzer for Doppler ultrasound signals," *Ultrasound Med. Biol.*, vol. 15, pp. 263-272, 1989.

Schlindwein FS, and Evans DH, "Selection of the order of autoregressive models for spectral analysis of Doppler ultrasound signals," *Ultrasound Med. Biol.*, vol. 16, no. 1, pp. 81-91, 1990.

Schwarz KQ, Bezante GP, Chen X, Mottley JG and Schlief R, "Volumetric arterial flow quantification using echo contrast. An *in vitro* comparison of three ultrasonic intensity methods: radio frequency, video and Doppler," *Ultrasound Med. Biol.*, vol. 19, pp. 447-460, 1993.

Schwarz KQ, Bezante GP, Chen X, and Schlief R**,** "Quantitative echo contrast concentration measurement by Doppler sonography," *Ultrasound Med. Biol.*, vol. 19, pp. 289-297, 1993.

Shi WT, and Forsberg F, "Ultrasonic characterization of the nonlinear properties of contrast microbubbles," *Ultrasound Med. Biol.* vol. 26, no. 1, pp. 93-104, 2000.

Shi WT, Forsberg F, Hall AL, Chia RY, Liu JB, Miller S, Thomenius KE, Wheatley MA, and Goldberg BB, "Subharmonic imaging with microbubble contrast agents: initial results," *Ultrasonic Imaging*, vol. 21, no. 2, pp. 79-94, 1999.

Shung KK, Sigelmann RA, Reid JM. "Scattering of ultrasound by blood," *IEEE Trans. Biomed. Eng.*, pp. 460-471, 1976.

Silva AC, Kim S, and Garwood M, "Imaging blood flow in brain tumors using arterial spin labeling," *Magnet. Reson. Med.*, vol. 44, no, 2, pp. 169-173, 2000.

Silverman RH, Kruse DE, Coleman DJ, and Ferrara KW, "High-resolution ultrasonic imaging of blood flow in the anterior segment of the eye," *Invest. Ophthalmol. Vis. Sci.*, vol. 40, no. 7, pp. 1373-1381, 1999.

Silverman RH, Lizzi FL, Ursea BG, Rondeau MJ, Eldeen NB, Kaliscz A, Lloyd HO, and Coleman DJ, "High-resolution ultrasonic imaging and characterization of the ciliary body," *Invest. Ophthalmol. Vis. Sci.*, vol. 42, no. 5, pp. 885-894, 2001.

Silverman RH, Ursea R, Kruse DE, Ferrara KW, Rondeau MJ, and DJ Coleman, "Ultrasound measurement of the effect of temperature on microperfusion in the eye," *Ultrasound Med. Biol.*, vol. 28, pp. 1413-1419, 2002.

Simpson DH, Burns PN, and Averkiou MA, "Techniques for perfusion imaging with microbubble contrast agents," *IEEE Trans Ultrason Ferroelectr Freq Control.*, vol. 48 pp. 1483-1494, 2001.

Simpson DH, Chien TC, and Burn PN, “Pulse inversion Doppler: a new method for detecting nonlinear echoes from microbubble contrast agents,” *IEEE Trans. Ultrason. Ferroelect. Freq. Contr.*, vol. 46, no. 2, pp. 372-382, 1999.

Simpson NE, and Evelhoch JL, “Deuterium NMR tissue perfusion measurements using the tracer uptake approach: II. comparison with microspheres in tumors,” *Magnet. Reson. Med.*, vol. 42, no. 2, pp. 240-247, 1999.

Stewart WC, and Castelli WP, “Systemic side effects of topical beta-adrenergic blockers,” *Clin. Cardiol.*, vol. 19, no. 9, pp. 691-697, 1996.

Stewart WC, and Garrison PM, “Beta-blocker – induced complications and the patient with glaucoma,” *Arch. Intern. Med.*, vol. 158, pp. 221-226, 1998.

Taylor JS, Tofts PS, Port DPR, Evelhoch JL, Knopp M, Riddick WE, Runge VM, and Mayr N, “MR imaging of tumor microcirculation: promise for the new millennium,” *J. Magn. Reson. Im.*, vol. 10, pp. 903-907, 1999.

Tortoli P, Guidi G, Guidi F, and Atzeni C, “A review of experimental transverse Doppler studies,” *IEEE Trans. Ultrason,. Ferroelect., Freq. Contr.*, vol. 41, no. 1, pp. 84-89, 1994.

Tortoli P, Guidi G, Mariotti V, and Newhouse VL, “Experimental proof of Doppler bandwidth invariance,” *IEEE Trans. Ultrason. Ferroelect. Freq. Contr.*, vol. 39, pp. 196-203, 1992.

Tortoli P, Guidi G, and Newhouse VL, “Improved blood velocity estimation using the maximum Doppler frequency,” *Ultrasound Med. Biol.*, vol. 21, no. 4, pp. 527-532, 1995.

Turnbull DH, Starkoski BG, Harasiewicz KA, Semple JL, From L, Gupta AK, Sauder DN, and Foster FS, “A 40–100MHz B-scan ultrasound backscatter microscope for skin imaging,” *Ultrasound Med. Biol.*, vol. 21, no. 1, pp. 79-88, 1995.

Ugolini P, Delouche A, Herment A, and Diebold B, “*In vitro* flow quantification with contrast power Doppler imaging,” *Ultrasound Med. Biol.*, vol. 26, pp. 113-120, 2000.

Vaitkus PJ, Cobbold RS, and Johnston KW, “A comparative study and assessment of Doppler ultrasound spectral estimation techniques. II: Methods and results,” *Ultrasound Med. Biol.*, vol. 14, no. 8, pp. 673-688, 1988.

Wax MB, and Molinoff PB, “Distribution and properties of β-adrenergic receptors in human iris-ciliary body,” *Invest. Ophthalmol. Vis. Sci.*, vol. 28, no. 3, pp.

420-430, 1987.

Wei K, Jayaweera AR, Firoozan S, Linka A, Skyba DM, and Kaul S, “Quantification of myocardial blood flow with ultrasound-induced destruction of microbubbles administered as a constant venous infusion,” *Circulation*, vol. 97, no. 5, pp. 473-483, 1998.

Wilkening W, Helbeck S, Postert T, Federlein J, Rose J, Hoppe P, Buttner Y, and Ermert H, “Brain perfusion imaging using contrast agent specific imaging modes,” in *Proc. IEEE Ultrasonic Symp.*, pp. 1721-1724, 1999.

Wilkening W, Postert T, Federlein J, Kono Y, Mattrey RF, and Ermert H, “Ultrasonic assessment of perfusion conditions in the brain and in the liver,” in *Proc. IEEE Ultrasonic Symp.*, pp. 1545-1548, 2000.

Williamson TH, and Harris A, “Ocular blood flow measurement,” *Brit. J. Ophthalmol.*, vol. 78, no. 12, pp. 939-945, 1994.

Wilson B, Shung KK, Hete B, Levene H, and Barnhart JL, “A feasibility study on quantitating myocardial perfusion with Albunex®, an ultrasonic contrast agent,” *Ultrasound Med. Biol.*, vol. 19, pp. 181-191, 1993.

Yeh CK and Li PC, “Doppler angle estimation using AR modeling”, *IEEE Transactions on Ultrasonics, Ferroelectrics and Frequency Control,* vol. 49, no. 6, pp. 683-692, 2002.

Yeh CK and Li PC, “Doppler angle estimation of pulsatile flow using AR modeling,” *Ultrason Imaging*, vol. 24, pp. 135-146, 2002.

Yeh CK, Wang SW, and Li PC, “Feasibility study on the time-intensity based blood flow measurements using deconvolution.” *Ultrason Imaging*, vol. 23 pp. 90-105, 2001.

Yeh CK, Yang MJ, and Li PC, “Contrast-specific ultrasonic flow measurements based on both input and output time intensities,” *Ultrasound Med. Biol.*, vol. 29, no. 5, pp. 671–678, 2003.

Yeh CK, Ferrara KW, and Kruse DE, “High-resolution functional vascular assessment with ultrasound”, *IEEE Transactions on Medical Imaging*, 2003.

Zagar BG, Fornaris RJ, and Ferrara KW, “Ultrasonic mapping of the microvasculature: signal alignment,” *Ultrasound Med. Biol.*, vol. 24, no. 6, pp. 809-824, 1998.

Zweifach BW, and Lipowsky HH, “Pressure and flow distribution in microcirculation,” in *Handbook of Physiology*, vol. 11, Sec. 5, E. M. Renkin and C. C. Michel, Ed. Washington, D. C.: American Physiological Society, pp. 251–307 1985.

Publication List

Journal Articles

[1] P. C. Li, C. J. Cheng, and Chih-Kuang Yeh, “ On velocity estimation using speckle decorrelation,” *IEEE Transactions on Ultrasonics, Ferroelectrics and Frequency Control,* vol. 48, no. 4, pp. 1084-1091, 2001.

[2] Chih-Kuang Yeh, S. W. Wang, and P. C. Li, “Feasibility study on the time-intensity based blood flow measurements using deconvolution,” *Ultrasonic Imaging*, vol. 23, pp. 90-105, April, 2001.

[3] Chih-Kuang Yeh and P. C. Li, “Doppler angle estimation using AR modeling”, *IEEE Transactions on Ultrasonics, Ferroelectrics and Frequency Control,* vol. 49, no. 6, pp. 683-692, 2002.

[4] Chih-Kuang Yeh and P. C. Li, “Contrast-based flow measurements using both inflow and outflow time–intensities,” *Proceeding in Biomedical Optical and Imaging*: *Ultrasound Imaging and Signal Processing*, Vol. 4, No. 26, pp. 357-364, 2003.

[5] P. C. Li, Chih-Kuang Yeh, and S. W. Wang, “Time-intensity-based volumetric flow measurements: an in vitro study,” *Ultrasound in Medical & Biology*, vol. 28, no. 3, pp. 349–358, 2002.

[6] Chih-Kuang Yeh and P. C. Li, “Doppler angle estimation of pulsatile flow using AR modeling,” *Ultrasonic Imaging*, vol. 24, pp. 135-146, 2002.

[7] Chih-Kuang Yeh, M. J. Yang, and P. C. Li, “Contrast-specific ultrasonic flow measurements based on both input and output time intensities,” *Ultrasound in Medical & Biology*, vol. 29, no. 5, pp. 671–678, 2003.

[8] Chih-Kuang Yeh, K. W. Ferrara and D. E. Kruse, “High-resolution functional vascular assessment with ultrasound”, *IEEE Transactions on Medical Imaging*, 2004. (accepted)

Conference Papers

[1] Chih-Kuang Yeh and P. C. Li, “ Doppler angle estimation using the AR spectrum model,” *IEEE Ultrasonics Symposium*, Puerto Rico, vol. 2, pp. 1513 -1516, 2000.

[2] Chih-Kuang Yeh and P. C. Li, "The application of AR spectrum model to Doppler angle estimation" Symposium of Annual Conference of the Biomedical Engineering Society, Taipei, Taiwan, R.O.C., December 15-16, 2000.

[3] Chih-Kuang Yeh, S. W. Wang and P. C. Li, “Contrast-based ultrasonic blood flow measurements based on inflow/outflow time intensities,” 23rd Annual International Conference of the IEEE Engineering in Medicine and Biology Society, Istanbul, Turkey, pp. 2617-2620, vol. 3, 2001.

[4] P. C. Li, Chih-Kuang Yeh, and S. W. Wang, “Assessment of Blood Flow Parameters Using Ultrasonic Contrast Agents,” *The 9th SCBA International Symposium*, Taipei, Taiwan, 2001.

[5] Chih-Kuang Yeh, S. Y. Kuo and P. C. Li, “The quality testing procedures of medical ultrasound image,” *The 6-th proceeding of Chinese National Laboratory Accreditation*, Section A5, November 30, Taipei, Taiwan, 2001.

[6] Chih-Kuang Yeh and P. C. Li, “Contrast-based flow measurements using both inflow and outflow time–intensities,” *SPIE*, *Medical Imaging*, Feb 15-20, San Diego, USA, 2003.

[7] Chih-Kuang Yeh, D. E. Kruse and K. W. Ferrara, “A new high frequency destruction/reperfusion system with preliminary results,” *The 8th US Contrast Research Symposium*, San Diego, USA, 2003.

[8] Chih-Kuang Yeh, D. E. Kruse, M. C. Lim, D. E. Redline, and K. W. Ferrara, “A new high frequency destruction/reperfusion system” *IEEE Ultrasonics Symposium*, Hawaii, 2003. (in press)

[9] D. E. Kruse, Chih-Kuang Yeh, and K. W. Ferrara, “A new imaging strategy utilizing wideband transient response of ultrasound contrast agents”, *IEEE Ultrasonics Symposium*, Hawaii, 2003. (in press)

[10] Chih-Kuang Yeh, D. E. Kruse, and K. W. Ferrara, “High-resolution vascular assessment using contrast-assisted ultrasound system” Symposium of Annual Conference of the Biomedical Engineering Society, Taiwan, 2003.